Bubble dynamics and its application in dental cleaning

By

You Yu

A thesis submitted to
the University of Birmingham
for the degree of
DOCTOR OF PHILOSOPHY

School of Mathematics
College of Engineering and Physical Sciences
University of Birmingham
August 2023

UNIVERSITY OF
BIRMINGHAM

University of Birmingham Research Archive

e-theses repository

This unpublished thesis/dissertation is copyright of the author and/or third parties. The intellectual property rights of the author or third parties in respect of this work are as defined by The Copyright Designs and Patents Act 1988 or as modified by any successor legislation.

Any use made of information contained in this thesis/dissertation must be in accordance with that legislation and must be properly acknowledged. Further distribution or reproduction in any format is prohibited without the permission of the copyright holder.

© Copyright by YOU YU, 2023

All Rights Reserved

ABSTRACT

Hydrodynamic cavitation is associated with broad and vital applications, including pump, turbine, and propeller damage. Acoustic cavitation also has biomedical ultrasound, sonochemistry, and cavitation cleaning applications. This thesis includes three published journal articles concerned with the dynamics of a single bubble in a viscous compressible liquid near a rigid boundary at a moderately large Reynolds number of O(10-100) and the application of bubble clouds in dental cleaning.

Chapter 3 explores the bubble dynamics near a rigid boundary for a Reynolds number of O(10-100) by experiments and simulations. A non-reflective boundary condition is proposed based on the far-field asymptotic behaviour. New mechanisms are found for the development of bubble jetting, the vortex sheet, and the vortex ring.

In Chapter 4, numerical studies have been conducted for a scaler vibrating in a periodontal pocket using ABAQUS based on the finite element method. A parametric study has been carried out in terms of the volume of the pocket, the taper ratio, and the immersion depth of the scaler tip in the pocket.

In Chapter 5, we further analyse how the scaler's amplitude, frequency, and cross-sectional shape affect cavitation generation in the pocket to provide practical guidance for optimising dental scaler settings, which can improve oral hygiene and prevent complications related to dental implants.

ACKNOWLEDGMENTS

I would like to express my heartfelt gratitude to my supervisors, Prof. Qianxi Wang and Dr. Warren Smith, for their unwavering support and invaluable guidance throughout my academic journey.

I would also like to extend my appreciation to the collaborators, namely Prof. Damien Walmsley, Prof. Timothy Leighton, Prof. Jie Cui, Dr. Mehdi Mahmud, and Dr. Nina Vyas. They have played a pivotal role in creating the three journal articles presented within my thesis.

Furthermore, I wish to extend my thanks to the School of Mathematics and the University of Birmingham for providing the essential support of the studentship and the High-Performance Computing service (BlueBEAR HPC service).

LIST OF PUBLICATIONS

Y. Yu, J. Cui, W. R. Smith, Q. Wang, and T. G. Leighton. "The mechanisms of jetting, vortex sheet and vortex ring development in asymmetric bubble dynamics". . In: *Physics of Fluids* 35.12 (2023), p. 123320. (reformatted and partially edited in chapter 3)

Y. Yu, M. Mahmud, N. Vyas, W. R. Smith, Q. Wang, and A. D. Walmsley. "Cavitation in a periodontal pocket by an ultrasonic dental scaler: A numerical investigation". In: *Ultrasonics Sonochemistry* 90 (2022), p. 106178. (reformatted and partially edited in chapter 4)

Y. Yu, W. R. Smith, Q. Wang, and A. D. Walmsley. "Numerical investigation of cavitation in periodontal pockets: insights for enhancing cleaning efficiency". In: *Ultrasonics Sonochemistry* 100 (2023), p. 106625. (reformatted and partially edited in chapter 5)

Contents

Page

1 General introduction **1**

1.1 Research background 1

1.2 Literature review 2

1.2.1 Single bubble dynamics 2

1.2.2 Bubble clusters dynamics 3

1.2.3 Ultrasonic cavitation in dental cleaning 5

1.3 Thesis overview 6

1.4 Original contributions clarification 9

2 Numerical models **10**

2.1 Numerical Simulations of bubble dynamics using OpenFOAM 10

2.1.1 Volume of fluid method for multiphase flow 10

2.1.2 Bubble dynamics and multiphase flow 15

2.2 Numerical simulation of ultrasonic cavitation using ABAQUS 19

2.2.1 Governing equations 20

2.2.2 Modelling of cavitation 23

3 The mechanisms of jetting, vortex sheet and vortex ring development in asymmetric bubble dynamics **25**

3.1 Introduction 26

3.2 Methodology 26
3.2.1 Experiment 27
3.2.2 Numerical simulation 29
3.3 Experimental results 34
3.3.1 Spherical bubble oscillation in the silicone oil 34
3.3.2 Bubble oscillation near a rigid boundary in silicone oils 36
3.4 Numerical results 39
3.4.1 Comparisons with experiments 40
3.4.2 Bubble dynamics near a rigid boundary for $Re = O(10)$ 44
3.5 Chapter summary 57

4 Cavitation in a periodontal pocket by an ultrasonic dental scaler: a numerical investigation 58

4.1 Introduction 59
4.2 Physical and numerical model 60
4.2.1 Problem description 60
4.2.2 Numerical model 61
4.3 Numerical validations 62
4.3.1 Choice of time step 63
4.3.2 Mesh convergence tests 64
4.3.3 The truncated computational domain 64
4.3.4 Comparisons with experimental results 64
4.4 Numerical results 68
4.4.1 Cavitation around a scaler tip 68
4.4.2 Effects of the hole volume 69
4.4.3 Effects of the taper ratio 70
4.4.4 Effects of the immersion depth 71

4.5 Chapter summary 73

5 Numerical investigation of cavitation in periodontal pockets: insights for enhancing cleaning efficiency 74

5.1 Introduction 75

5.2 Physical and numerical model 75

5.2.1 Problem description 75

5.2.2 Numerical model 77

5.3 Numerical validations 79

5.3.1 Numerical setup 79

5.3.2 Mesh convergence test 81

5.3.3 Comparison with the experiment 81

5.4 Numerical results 82

5.4.1 Effects of the vibration amplitude 83

5.4.2 Effects of the vibration frequency 85

5.4.3 Effects of the shape of the scaler tip cross-section 87

5.5 Chapter summary 90

6 Summary, conclusions and possible developments 91

6.1 Summary and conclusions 91

6.2 Possible developments 95

A Derivation of Rayleigh-Plesset equation for a spherical bubble 96

B Derivation of Keller-Miksis equation for a spherical bubble 100

References 105

List of Figures

2.1 Volume of fluid approach. 11

2.2 Wedge-shaped computational domain. 16

2.3 Computation of values at the wedge boundary. 16

3.1 (a) Experimental setup used to generate a cavitation bubble and record its dynamics. (b) Underwater discharge circuit. 27

3.2 Sketch of the bubble in a container filled with the liquid in the experiment. . 28

3.3 Sketch of the geometry and the boundary conditions used for the simulations of bubble dynamics near a rigid boundary. (a) 3D view of the truncated computational domain, (b) 2D projection of the computational domain in the *Oxz*-plane. An initially spherical bubble of high internal pressure is inserted into the liquid at a distance D from the boundary, and (c) a schematic diagram of the computational mesh. 32

3.4 Comparison of the equivalent bubble radius histories R_{eq} obtained from different computational domain sizes $10R_{max}$ and $100R_{max}$ respectively, for a bubble with the maximum radius $R_{max} = 600$ μm at the dimensionless stand-off distance $\gamma = 1.1$ from a rigid boundary. The initial conditions for the computation are $R_0 = 300$ μm, $\dot{R}_0 = 20$ m/s and $p_{b0} = 1500$ Pa. Other parameters used for calculations are $\rho_\infty = 998$ kg/m^3, $\rho_{ref} = 1.2$ kg/m^3, $p_\infty = p_{ref} = 101315$ Pa, $\mu_g = 1.73 \times 10^{-5}$ Pa $\cdot$ s, $\mu_l = 0.001$ Pa $\cdot$ s, $\gamma_h = 1.4$, $\sigma = 0.072$ N/m, and $c = 1500$ m/s. 34

3.5 Convergence tests in terms of various element numbers: 64356, 256719, 501671, and 756954, for (a) the equivalent bubble radius R_{eq} histories and (b) the bubble shapes. Parameters used for calculations are the same as in figure 3.4. . . 35

3.6 The evolution of bubble shapes for a spherical bubble oscillating in the 1000cSt silicone oil with the density ρ_l, the dynamic viscosity μ_l, and the surface tension coefficient σ being 975 kg/m^3, 0.975 Pa $\cdot$ s, and 0.021 N/m, respectively. 36

3.7 Comparison of the equivalent bubble radius R_{eq} history with the solution of the Keller-Miksis equation for a spherical bubble oscillating in the 1000cSt silicone oil for the case in figure 3.6. Other parameters used for the Keller-Miksis equation are $p_{b0} = 659$ Pa, $R_0 = 14.74$ mm, $p_v = 31000$ Pa, $p_\infty = 101315$ Pa, $\gamma_h = 1.4$, $\sigma = 0.021$ N/m, and $c = 950$ m/s. 37

3.8 The evolution of bubble shapes for a bubble oscillating near a rigid boundary in (a) water with the viscosity μ_l being 0.001 Pa $\cdot$ s, (b) 500cSt silicone oil with the viscosity μ_l being 0.485 Pa $\cdot$ s, and (c) 1000cSt silicone oil with the viscosity μ_l being 0.975 Pa $\cdot$ s at the dimensionless standoff distance $\gamma \approx 1.4$. The densities ρ_l are 998, 975, and 975 kg/m^3, respectively. The surface tension coefficients σ are 0.072, 0.021, and 0.021 N/m, respectively. The maximum bubble radii R_{max} attained in the experiment are about 16.35, 15.33, and 14.03 mm, respectively. 38

3.9 Comparison of bubble shapes between the computation and the experiment for the bubble oscillating in the 500cSt silicone oil with the viscosity being 0.485 Pa·s at typical times (a) 1.90 ms, (b) 2.66 ms, (c) 3.16 ms, (d) 3.42 ms, (e) 3.67 ms, and (f) 3.92 ms. Parameters used for the calculation are $R_0 = 10$ mm, $\dot{R}_0 = 12$ m/s and $p_{b0} = 720$ Pa, $\rho_\infty = 975$ kg/m^3, $\mu_l = 0.485$ Pa·s and $c = 950$ m/s, and the remaining parameters are the same as in figure 3.4. The left part in frames (a1)-(f1) is the computational results, while the right is the experimental results. The rigid boundary is the lower boundary of frames (a1)-(f1). The red dot displays the outer profile of the bubble shapes in the experiment. Frames (a2)-(f2) and frames (a3)-(f3) are 2D and 3D views of the simulated bubbles, respectively. 41

3.10 Comparison of the bubble shapes between the computation and the experiment [88] at typical times (a) 65 μs, (b) 125 μs, (c) 130 μs, (d) 140 μs, (e) 185 μs, and (f) 230 μs during the two cycles of oscillation. The parameters used for calculation are the same as in figure 3.4. The left part in frames a1-f1 is the computational results, while the right is the experimental results. The rigid boundary is the lower boundary of frames (a1)-(f1). The red dot displays the outer profile of the bubble shapes in the experiment. Frames (a2)-(f2) and frames (a3)-(f3) are 2D and 3D views of the simulated bubbles, respectively. 42

3.11 Comparison of the equivalent bubble radius R_{eq} history between the computation and the experiment [88] for the case in figure 3.10. The parameters used for the calculation are the same as in figure 3.4. 43

3.12 (a) Streamlines, (b) velocity vectors (left), velocity contour (left), and pressure contour (right) during early expansion when the bubble is nearly spherical. The Reynolds number is $Re = 75$ ($\mu_l = 0.08$ Pa·s), and the remaining parameters are the same as in figure 3.4. 45

3.13 Velocity vectors (left in each figure), velocity contours (left in each figure), and streamlines (right in each figure) at (a) 42 μs and (b) 47 μs showing the formation of the vortex sheet generated from the bubble collapse near a rigid boundary for the case in figure 3.12. (Recall that the simulations are axisymmetric when visualising the 3D form of the vortex sheet). 46

3.14 Velocity vectors (left in each figure), velocity contours (left in each figure), and streamlines (right in each figure) at (a) 50.2 μs and (b) 56 μs showing the conversion from the vortex sheet to the vortex ring for the case in figure 3.12. 46

3.15 Streamlines ((a) & (c)), velocity vectors (left in (b) & (d)), velocity contours (left in (b) & (d)), and vorticity contours (right in (b) & (d)) showing the further development of the vortex ring after generation during bubble collapse for the case in figure 3.12. 47

3.16 Bubble shapes evolutions near a rigid boundary for Re = 75, 6033 (μ_l = 0.08, 0.001 Pa$\cdot$s, respectively). The remaining parameters are the same as in figure 3.4. 49

3.17 Numerical results for Re = 75, 6033 (μ_l = 0.08, 0.001 Pa$\cdot$s, respectively): (a) histories of the equivalent bubble radius R_{eq} and (b) the jet velocity V_{jet}. The remaining parameters are the same as in figure 3.4. 50

3.18 Pressure contours showing the emission and propagation of shockwaves generated at the end of the first bubble collapse for the case in figure 3.12. . . . 51

3.19 Pressure on the centre point of the rigid boundary (green spots in figure 3.18) as a function of time for Re = 75, 6033 (μ_l = 0.08, 0.001 Pa$\cdot$s, respectively). The remaining parameters are the same as in figure 3.4. 52

3.20 The time-space map of the wall shear stress for the case in figure 3.12. The logarithm to the base 10 is taken of the wall shear stress values before plotting due to the large range of values. The first colour bar represents the positive wall shear stress (away from the axis of symmetry), while the second one represents the negative shear stress. Overlaid is the bubble dynamics as a dashed line adapted from figure 3.17(a). 53

3.21 Velocity vectors (black arrows), velocity contour (left), and pressure contour (right) at $t = 42$ μs for the case in figure 3.12. 54

3.22 The time histories of the shear stress at a point on the rigid boundary, at 180 μm from the axis of symmetry, for $Re = 75$, 6033 ($\mu_l = 0.08$, 0.001 Pa $\cdot$ s, respectively). Other parameters are the same as in figure 3.4. 55

3.23 Bubble shapes (frames (a1)-(d1)) and flow fields (frames (a2)-(d2)) including velocity vectors (left in frames (a2)-(d2)), velocity contours (left in frames (a2)-(d2)) and pressure contours (right in frames (a2)-(d2)) at (a) 120 μs, (b) 123 μs, (c) 127 μs, and (d) 150 μs during bubble collapse and rebound for the case in figure 3.12. 56

4.1 (a) Schematic problem description of ultrasonic scaler tip and its vibration in a periodontal pocket [126], and (b) 3D view of the computational domain where the periodontal pocket is simplified to a hole. 59

4.2 The illustration of (a) the scaler with the truncated surface S_{ts}, and (b) the cross-section of the computational domain at the *Oxy*-plane indicating the position of the displacement boundary condition at S_{ts}, the fluid-structure interface S_{fs}, the rigid wall surface S_{rw} and the truncated water planes S_{tf}. 61

4.3 Mesh convergence tests regarding the time history of the cavitation density within the hole. Element numbers are 2 million, 8 million, 12 million, and 16 million for coarse, medium, fine, and very fine mesh, respectively. The hole is a circular cylinder shape with radius $r = 1.5$ mm, depth $H = 10.0$ mm and the immersion depth of the scaler tip in the hole $h = 5.0$ mm. The amplitude A and the angular frequency ω of the harmonic oscillation of the scaler handpiece are 0.01 mm and 195000 rad/s (approx. 31 kHz). Other parameters used in the calculations are $\rho_f = 1000$ kg/m^3, $K_f = \rho_f c^2 = 2140$ MPa, $p_c = 2300$ Pa, $\rho_s = 8000$ kg/m^3, the Young's modulus $E = 224$ GPa, and $\nu = 0.3$ [166]. 65

4.4 (a) Illustration of the two truncated computational domains at *Oxy*-plane with different sizes. (b) Comparison of the displacement of the free end of the scaler tip along the x-axis for the computational domains $V_f \cup V_s$ and $V_f' \cup V_s'$. Other parameters used in the calculations are the same as in figure 4.3. . . . 66

4.5 Comparisons with experiments in terms of (a) the displacement of the free end of the scaler tip denoted by "+" in figure 4.4(b) along the x-axis, and (b) the cavitation pattern (black area) around the scaler tip at $t = 348.5$ μs in the simulation on *Oxy*-plane and in the experiment. Parameters used in the calculations are the same as in figure 4.3. 67

4.6 Pressure contours showing the cavitation pattern for a scaler vibrating in (a) an unbounded, infinite domain, and (b) a hole at $t = 399$ μs. The black area denotes the area of cavitation. Other parameters used in the calculations are the same as in figure 4.3. 69

4.7 (a) Schematic diagram for a dental scaler vibrating in holes with the volume being approximately 20.1, 70.7, 125.7 mm^3 (from left to right). (b) Time-averaged cavitation density in the hole versus the volume of the hole. The dimensionless immersion depth of the scaler tip in the hole is 0.5. Other parameters used in the calculations are the same as in figure 4.3. 70

4.8 (a) Schematic diagram for a dental scaler vibrating in holes with the depth H being 10 mm and the volume being 70.7 mm^3. The taper ratio η is 0.35, 1 and 2.75 (from left to right). (b) Time-averaged cavitation density in the hole versus the taper ratio of the hole. The dimensionless immersion depth of the scaler tip in the hole is 0.5, and other parameters used in the calculations are the same as in figure 4.3. 71

4.9 (a) Schematic diagram for a dental scaler vibrating in holes with the volume being 70.7 mm^3 and the taper ratio being 1. The dimensionless immersion depths are 0, 0.5, and 0.75 (from left to right). (b) Time-averaged cavitation density in the hole versus the dimensionless immersion depth of the scaler tip. Other parameters used in the calculations are the same as in figure 4.3. . . . 72

4.10 Pressure contours at $t = 399$ μs for cases with dimensionless immersion depths being (a) 0, (b) 0.5, and (c) 0.75 on the Oxy-plane of the hole. The black area denotes the area of cavitation. Other parameters used in the calculations are the same as in figure 4.3. 73

5.1 (a) Schematic illustration of the ultrasonic dental scaler and the periodontal pocket, and (b) 3D truncated domain in Cartesian coordinates. 76

5.2 The simplified representation of the periodontal pocket with gum tissue and the positions of the scaler in (a) the x-y plane and (b) the y-z plane. 77

5.3 (a) The position of the truncated and free end of the scaler tip. (b) Cross-sectional view of the computational domain at the x-y plane indicating the locations of the displacement boundary condition at S_{ts}, the liquid-scaler interface S_{ls}, the liquid-tissue interface S_{lg}, the tooth surface S_{rt} and the truncated surfaces of the computational domain S_{tf}. 78

5.4 Strain-stress curves of PDMS obtained from the experiment [172] and the fitting results using the 3^{rd} Ogden model in the simulations. 80

5.5 Mesh convergence tests for the cavitation volume within the periodontal pocket over time. The element numbers are about 1 million, 3 million, 8 million, and 12 million. The truncated surface of the scaler oscillates harmonically at the amplitude A = 0.01 mm and the frequency f = 31 kHz. Other parameters for the calculations are ρ_f = 1000 kg/m^3, K_f = 2140 MPa, p_c = 2300 Pa, ρ_{s1} = 8000 kg/m^3, E = 224 GPa, ν = 0.3, ρ_{s2} = 980 kg/m^3, μ_1 = -0.102 MPa, μ_2 = -0.095 MPa, μ_3 = -0.117 MPa, α_1 = 5.226, α_2 = 5.448, and α_3 = -5.545. 82

5.6 (a) Schematic of the scaler near a wall in the experiment, (b) a high-speed experimental cavitation image, and (c) the contour of the liquid pressure. The black region represents cavitation, where the pressure reduces to the cavitation limit of 2300 Pa. Other parameters are the same as in figure 5.5. 83

5.7 Void fraction in the periodontal pocket with both soft and nearly rigid boundaries plotted against the scaler tip's oscillation amplitude A. The oscillation amplitude A ranges from 0.005 to 0.02 mm, and other parameters are the same as in 5.5. 84

5.8 Void fraction in the periodontal pocket with both soft and nearly rigid boundaries plotted against the scaler's vibration frequency f. The vibration frequency f ranges from 20 to 45 kHz, and other parameters are the same as in figure 5.5. 85

5.9 The root mean square (RMS) amplitude of the scaler tip along the x- and y-axes plotted against the vibration frequency f of the scaler tip. The vibration frequency f ranges from 20 to 45 kHz, and other parameters are the same as in figure 5.5. 86

5.10 Schematics showing various cross-sectional shapes of dental scalers, where the x-axis is along the scaler tip displacement direction. Type A: a thin cross-section ($\xi = 0.5$), Type B: a circular cross-section ($\xi = 1$), and Type C: a blunt cross-section ($\xi = 2$). 87

5.11 Void fraction in the periodontal pocket with both soft and nearly rigid boundaries, generated by dental scalers with different cross-sectional shapes (Type A: a thin cross-section $\xi = 0.5$, Type B: a circular cross-section $\xi = 0.5$, and Type C: a blunt cross-section $\xi = 0.5$). Parameters are the same as in figure 5.5. 88

5.12 The RMS amplitude of the scaler tip along the x- and y- axes for dental scalers with different cross-sectional shapes (Type A: a thin cross-section $\xi = 0.5$, Type B: a circular cross-section $\xi = 1$, and Type C: a blunt cross-section $\xi = 2$). Other parameters are the same as in figure 5.5. 89

List of Tables

3.1 Properties of the liquids used in the experiment, the Reynolds and Weber numbers, the corresponding maximum equivalent bubble radius R_{max}, and the period for the first oscillation cycle P_1. 36

Chapter One

General introduction

1.1 Research background

Hydrodynamic cavitation occurs when the pressure within the liquid drops below its vapour pressure, forming tiny vapour-filled bubbles within the liquid [1]. Research interests concerning cavitation bubbles can be categorised into two primary domains. Firstly, uncontrolled cavitation can cause damage to hydraulic systems, such as propellers [2], hydro turbines [3], and pumps [4]. Cavitation near these components often results in significant noise, damage to components, vibrations, and reduced efficiency [5, 6]. This damage mechanism is attributed to shockwaves [7–9] and bubble jetting [10–12], both originating during the final stages of bubble collapse. Thus, the primary focus of studying bubble dynamics is understanding how cavitation can negatively impact these components [1, 13, 14].

Secondly, controlled cavitation has diverse practical applications. Ultrasonic cavitation bubbles, a form of controlled cavitation, are generated by applying highly intense focused ultrasound (HIFU). It has applications in the field of biomedical ultrasound [15, 16], including drug delivery [17–19], extracorporeal shockwave lithotripsy [20–23], tissue ablation [16, 24–26], as well as oncology [27] and cardiology [28, 29]. Additionally, it is applied

in sonochemistry [30–33] and cavitation cleaning [34–41]. In these applications, cavitation bubbles absorb and focus a significant amount of energy from ultrasound, resulting in shape oscillations, strong shockwaves, forceful collapses, and intense bubble jetting [42].

1.2 Literature review

1.2.1 Single bubble dynamics

The dynamics of a single bubble has been extensively studied theoretically [43–54], experimentally [8, 9, 55–61], and numerically [62–68] for a long time. Experimental studies for the bubble distributions of various cavitation structures (bubble filaments, bubble clusters, and acoustically cavitated jets) have shown a centroid at an equilibrium radius of approximately 2-4 μm [69]. Therefore, considering viscous effects is vital because the Reynolds number for cavitation bubble dynamics is relatively small.

Previous studies have primarily focused on bubbles with radii of $O(100)$ μm or larger, with Reynolds numbers of $O(10^3)$ or larger. Extensive experiments have been conducted on bubbles with radii of approximately $O(100)$ μm or larger [9, 24, 55, 56, 58, 70–76]. This could be attributed to the fact that experimental investigations of cavitation bubbles, with dimensions and durations on the order of $O(1)$ μm and $O(1)$ μs, are limited by the requirement for high spatial and temporal resolution.

In numerical studies, the bubble dynamics of a single bubble has been extensively modelled using the boundary integral method based on the potential flow theory [24, 62, 77–81] and the Navier–Stokes equations coupled with various interface-capturing schemes [63, 66, 67, 82–90]. These computations are carried out for Reynolds numbers of $O(10^3)$ or larger. One of the challenges in studying bubble dynamics by solving the Navier–Stokes equations

is the need for a large computational domain. To prevent the reflection from the far field, its typical dimension is on the order of $O(100R_{max})$, where R_{max} represents the maximum bubble radius. Another challenge is that the mesh and temporal resolution must be fine enough across the entire computational domain to model shockwave propagation accurately. The loss of energy associated with the emission of shockwaves at the end of the collapse was not accurately captured in the previous computations. This could be due to the mesh size not being fine enough for simulating the radiation of shockwaves. In order to circumvent this issue, a portion of the bubble's potential energy was manually removed at the end of the first cycle of oscillation to continue the computations and to achieve agreement with experiments for the second cycle [88]. Therefore, any development in the numerical model that can reduce the computational cost is highly desirable.

Furthermore, it is well known that the conditions inside a collapsing bubble essentially determine the chemical consequences of cavitation [33, 91]. This collapse will not only occur at rigid boundaries but also when two bubbles are in close proximity in the cloud. However, the fluid mechanics of the bubble gas during the asymmetric collapse remains unclear.

1.2.2 Bubble clusters dynamics

In recent years, bubble cluster dynamics has attracted growing interest, as practical cavitation phenomena are commonly linked to cloud cavitation [92]. Bubble clusters exhibit strong bubble-bubble interactions, leading to a non-spherical collapse of nearly all bubbles within the cluster. During the collapse of the bubble cluster, an inward-propagating shock wave emerges from a single bubble, converging with its precursor towards the cluster's centre. As this shock passes other bubbles, it generates a large pressure pulse, inducing further bubble collapse. The convergence of these shock waves results in a focal point of high-frequency pressure oscillations and vigorous bubble collapses, leading to elevated pressure peaks sev-

eral hundred times greater than those observed in individual bubble collapses, resulting in a significantly intense impact on materials [7, 93]. Understanding the dynamics of bubble clusters will not only aid in comprehending the mechanisms of cavitation erosion but also facilitate the utilisation of cavitation bubbles.

However, the detailed dynamics of these clusters suffers from a lack of understanding due to the length scales of $O(10)$ μm and time scales of $O(1)$ μs during the final and most destructive collapse stage, which pose challenges to measurement technologies in experiments [7, 94–98]. Many researchers use numerical methods to explore the dynamics of bubble clusters [99–101]. However, these methods can only consider simple or idealised applications as the dynamics of individual bubble particles in these methods are governed by the Rayleigh-Plesset equations, which only account for a spherical bubble shape. Other approaches based on the boundary integral method [102] or a homogeneous mixture model solving the Navier-Stokes equations [98, 103, 104] can consider asymmetries and non-spherical bubbles, capturing the dynamics of more realistic configurations. However, these methods remain computationally demanding and are restricted to small-scale issues suitable for fundamental research purposes. Dealing with resolved bubble clouds composed of thousands of bubbles requires extremely large computational grids. [105–108].

For practical and engineering applications, cavitation bubble clusters are often modelled using simplified homogeneous models [109–111] and mass transfer rate models [112–118], disregarding bubble-bubble interactions and the consequent non-spherical deformation of bubbles. Similar models can currently be found within commercial CFD software packages and open-source CFD toolkits [119].

1.2.3 Ultrasonic cavitation in dental cleaning

Ultrasonic dental scalers are essential to routine periodontal therapy for effectively removing bacterial biofilm (dental plaque) from teeth and dental implants [120]. The most effective treatment for cleaning dental plaque biofilms has yet to be established, although using ultrasonic instruments is recommended [121].

Cavitation, which involves the formation and collapse of microbubbles within a liquid, occurs in the cooling water surrounding the tips of ultrasonic scalers [122–126]. Cleaning effects result from various mechanisms when cavitation bubbles collapse, including the formation of microjets during microbubble collapse that induces localised shear stress on the biofilm [34, 35, 127], shockwaves emitted during microbubble implosion [128], microstreamers, acoustic streaming in the bulk fluid, and microstreaming around individual cavitation bubbles as they oscillate [129]. This cavitation can be used to clean dental biofilms in a non-contact approach, proving beneficial in hard-to-reach regions of the mouth, such as within periodontal pockets, root furcation, and on artificial surfaces like dental implants.

Previous studies have confirmed that cavitation occurs around dental scaler tips, enhancing the cleaning process [37, 38, 122]. Enhancing the cavitation generated by an oscillating scaler tip could pave the way for innovative clinical approaches to the cleaning process. Manmi et al. [40] investigated the influence of operation conditions of ultrasonic dental scalers on cavitation generation around a scaler tip in an unbounded liquid using the one-fluid, cut-off cavitation model. This model solves the governing equations for a single phase, employed to represent two distinct phases of the fluid (such as water and vapour). It treats the cavitation region as a homogeneous single-phase area with a constant total pressure equal to the vapour pressure of water when the cavitation criterion is met [130]. However, the current understanding of cavitation behaviour remains limited when the scaler tip is confined, such as a scaler in a periodontal pocket. The effects of the confined space's

shape, optimal operation conditions, and ideal scaler tip design remain unclear.

1.3 Thesis overview

This thesis addresses the bubble dynamics in a viscous, compressible liquid near a rigid boundary and its application in cavitation dental cleaning. It includes three journal articles that have been published. The thesis is structured as follows:

Chapter 2. Numerical models

The numerical models used in this study and some specific treatments have been described in this chapter.

Chapter 3. The mechanisms of jetting, vortex sheet and vortex ring development in asymmetric bubble dynamics

The viscous bubble dynamics for a Reynolds number of O(10-100) has been investigated using experiments and computations.

Our collaborator in this study, Jie Cui, conducted experiments for electric spark-generated bubbles in silicone oils with a high-speed camera, as the viscosity of silicone oils is two to three orders of magnitude higher than that of water. In order to maintain the same Reynolds number, bubble sizes in silicone oils are increased by two to three orders of magnitude compared to those in water. To be specific, in order to conduct experiments for bubbles with $Re = O$(10-100) in water, bubbles radii are O(1-10) μm. Similarly, for bubbles with $Re = O$(10-100) in silicone oils, bubbles radii are O(1-10) mm. Another advantage of using a high-viscosity liquid is that bubble surfaces in water often become unstable after the first oscillation cycle. Bubble surfaces in silicone oil are more stable, and thus, more cycles of oscillations may be observed and studied.

Our numerical simulations are based on the axisymmetric compressible Navier-Stokes equations using OpenFOAM [131], following Koch et al. [63], Lechner et al. [67, 85] and Zeng et al. [88]. A non-reflective boundary condition is proposed based on the far-field asymptotic behaviour obtained from the weakly compressible theory [81, 132, 133]. The newly proposed boundary condition reduces the dimension of the computational domain tenfold. With this reduction in domain size, a sufficiently fine grid can be used for the computational domain to accurately capture the shockwaves' radiation.

New mechanisms are found for the development of bubble jetting, the vortex sheet, and the vortex ring. An initially located stagnation point at the bubble centre migrates from the wall due to asymmetric bubble expansion and moves out of the bubble at approximately the maximum bubble volume, a vortex sheet forming inside the bubble during this process. As the vortex sheet approaches the bubble interface, it transfers momentum to the gas-liquid interface, influencing the liquid flow close to the bubble wall. The high-pressure zone at the stagnation point drives the distal part of the bubble surface to collapse first and fastest subsequently. The asymmetric collapse generates the circulation around the side cross-section of the bubble, and a vortex ring thus develops within the bubble gas at the outer rim of the vortex sheet as the vortex sheet itself decays. With its core inside the bubble gas, the vortex ring functions like a bearing system in accelerating the jet. Bubble dynamics, including jetting, shockwaves, and viscous shear stress, is analysed in terms of the Reynolds number.

Chapter 4. Cavitation in a periodontal pocket by an ultrasonic dental scaler: a numerical investigation

Using the finite element method, cavitation in a periodontal pocket by an ultrasonic dental scaler has been investigated using ABAQUS. The simulations consider the three-dimensional, nonlinear, and transient interaction between the vibration and deformation of

the scaler tip; the water flows around the scaler and the cavitation formation. The numerical model is validated by comparing results with the experimental data for a scaler vibrating in an unbounded liquid, the displacement at the scaler's free end, and the cavitation pattern near the scaler tip displaying excellent agreement. The amount of cavitation generated is evaluated by the cavitation density (or the void fraction), the ratio of cavitation volume occupied in the hole to the total hole volume.

Numerical results indicate that the cavitation density in the hole increases with the decreasing hole volume and the increasing taper ratio. Cleaning effects could be increased if some modifications to the scaler design could be made to increase the blocking effect of the hole during the cleaning process. Cavitation is observed in the hole even if the scaler is placed above the hole and increases with the immersion depth.

Chapter 5. Numerical investigation of cavitation in periodontal pockets: insights for enhancing cleaning efficiency

Numerical investigations of cavitation in periodontal pockets have been conducted to provide insights for enhancing cleaning efficiency in dental cleaning. This chapter describes two developments to the research in Manmi et al. [40] and in chapter 3. Firstly, we account for the influence of the soft tissue of the periodontal pocket on cavitation development, which better represents the practical clinical scenario. We model soft tissue by incorporating the Ogden model [134, 135]. Secondly, we study the effects of the operation conditions of the dental scaler and the scaler's cross-sectional shape on cavitation generation to optimise the design of ultrasonic scalers.

Numerical results indicate that cavitation is more pronounced for a scaler oscillating near a nearly rigid boundary than a soft boundary. It increases with the vibration amplitude because higher ultrasonic energy transfers to the liquid and generates stronger pressure waves. The resonant frequency of the scaler coincides with the maximum cavitation and

scaler tip amplitude. Reducing the dimension of the cross-section of the scaler in its oscillation direction increases both the scaler tip amplitude and the cavitation generated. This finding offers a potential design approach for enhancing the scaler cavitation and its cleaning effects.

Chapter 6. Summary, conclusions, and possible developments

Summary, conclusions, and possible developments are presented.

1.4 Original contributions clarification

The thesis is paper-based and contains both experimental and numerical studies. The author proposed a new non-reflective far-field boundary condition and implemented it in OpenFOAM. Additionally, the author implemented the Ogden model for hyperelastic materials in ABAQUS. Based on these developments, numerical simulations were conducted to study bubble dynamics and its application in dental cleaning in chapters 3-5. The experimental study in chapter 3 is performed by the collaborator Prof. Jie Cui from Jiangsu University of Science and Technology, China.

Chapter Two

Numerical models

2.1 Numerical Simulations of bubble dynamics using OpenFOAM

OpenFOAM (Open Field Operation And Manipulation) is an open-source cell-centred finite volume computational fluid dynamics (CFD) toolbox developed initially at Imperial College London by Jasak and Rusche [136, 137]. It comprises a collection of libraries and codes written in C++ to address complex fluid flow problems.

2.1.1 Volume of fluid method for multiphase flow

Multiphase flows are common in nature and industrial applications. Modelling these flows is challenging due to moving interfaces between different phases. Among various modelling approaches, the volume of fluid (VOF) method [138] is a popular and widely accepted technique for capturing multiphase flow interfaces and has been incorporated into OpenFOAM.

(i) Interface indicator

In the VOF method, multiphase flow interfaces are captured by assessing the fraction of the computational cell volume occupied by each phase [138]. For gas-liquid two-phase flow, the volume fraction of the liquid, α_l, is defined as the volume of liquid in the cell divided by the total cell volume. Consequently, as shown in figure 2.1, the value of α_l can fall into one of the following three conditions:

(1) $\alpha_l = 1$ the entire cell is filled with liquid;

(2) $\alpha_l = 0$ the entire cell is filled with gas;

(3) $0 < \alpha_l < 1$ the cell is filled with liquid and gas (interface region).

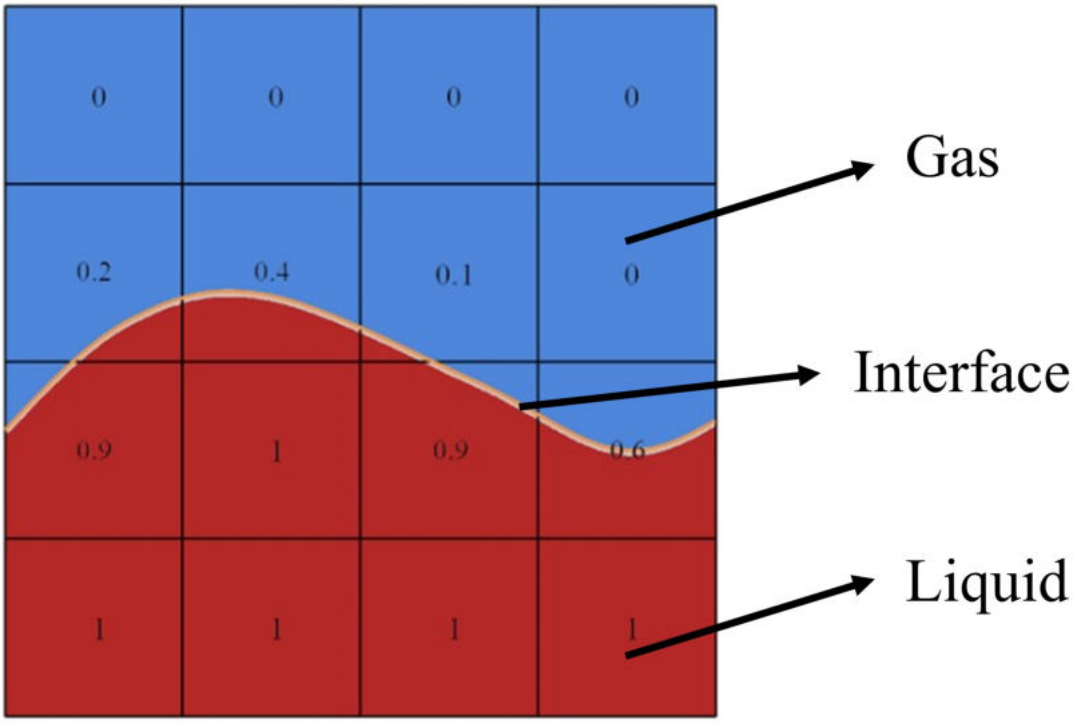

Figure 2.1: Volume of fluid approach.

The fluid density ρ and viscosity μ are expressed in terms of the volume fraction

parameter α_l of the liquid

$$\rho = \alpha_l \rho_l + \alpha_g \rho_g, \mu = \alpha_l \mu_l + \alpha_g \mu_g, \tag{2.1}$$

where $\alpha_l + \alpha_g = 1$, and the subscripts g and l denote the gas phase and the liquid phase, respectively.

(ii) Continuity equation

Assuming no mass transfer between the two fluids, the mass conservation can be expressed as a continuity equation for each phase

$$\frac{\partial (\alpha_i \rho_i)}{\partial t} + \nabla \cdot (\alpha_i \rho_i \mathbf{u}) = 0, i = l, g, \tag{2.2}$$

where $\mathbf{u}$ is the flow velocity.

The sum of the continuity equations for each phase leads to the overall continuity equation

$$\frac{\partial \rho}{\partial t} + \nabla \cdot (\rho \mathbf{u}) = 0. \tag{2.3}$$

(iii) Transport equation of the interface indicator

Differentiating equation (2.2) for the liquid reveals

$$\begin{aligned} &\tfrac{\partial \alpha_l}{\partial t} \rho_l + \alpha_l \tfrac{\partial \rho_l}{\partial t} + \rho_l \left(\nabla \cdot (\alpha_l \mathbf{u})\right) + \alpha_l \mathbf{u} \cdot \nabla \rho_l = 0, \\ &\Leftrightarrow \tfrac{\partial \alpha_l}{\partial t} + \nabla \cdot (\alpha_l \mathbf{u}) = -\tfrac{\alpha_l}{\rho_l} \left(\tfrac{\partial \rho_l}{\partial t} + \mathbf{u} \cdot \nabla \rho_l\right). \end{aligned} \tag{2.4}$$

Furthermore, it is observed that

$$\frac{d\rho_l}{dt} = \mathbf{u} \cdot \nabla \rho_l + \frac{\partial \rho_l}{\partial t}. \tag{2.5}$$

where d/dt is the Lagrangian derivative.

We also know that

$$\frac{d\rho_l}{dt} = \frac{d\rho_l}{dp} \frac{dp}{dt} = \psi_l \frac{dp}{dt}, \tag{2.6}$$

where $\psi_l = \frac{d\rho_l}{dp}$ is the compressibility of the liquid and p is the pressure.

Equation (2.4) may now be written as

$$\frac{\partial \alpha_l}{\partial t} + \nabla \cdot (\alpha_l \mathbf{u}) = -\frac{\alpha_l}{\rho_l}\left(\psi_l \frac{dp}{dt}\right). \tag{2.7}$$

This can be done for the gas phase as well so that

$$\frac{\partial(\alpha_l + \alpha_g)}{\partial t} + \nabla \cdot ((\alpha_l + \alpha_g)\,\mathbf{u}) = -\left(\frac{\alpha_l}{\rho_l}\psi_l + \frac{\alpha_g}{\rho_g}\psi_g\right)\frac{dp}{dt}, \tag{2.8}$$

where $\psi_g = \frac{d\rho_g}{dp}$ is the compressibility of the gas.

As $\alpha_l + \alpha_g = 1$, we have

$$\nabla \cdot \mathbf{u} = -\left(\frac{\alpha_l}{\rho_l}\psi_l + \frac{\alpha_g}{\rho_g}\psi_g\right)\frac{dp}{dt}. \tag{2.9}$$

Equation (2.7) can be written as follows:

$$\frac{\partial \alpha_l}{\partial t} + \nabla \cdot (\alpha_l \mathbf{u}) = -\frac{\alpha_l}{\rho_l}\left(\psi_l \frac{dp}{dt}\right) = -\alpha_l\left(\nabla \cdot \mathbf{u} + \frac{\psi_l}{\rho_l}\frac{dp}{dt}\right) + \alpha_l\left(\nabla \cdot \mathbf{u}\right). \tag{2.10}$$

Now inserting equation (2.8) into equation (2.10) gives us

$$\begin{aligned} &\tfrac{\partial \alpha_l}{\partial t} + \nabla \cdot (\alpha_l \mathbf{u}) = -\alpha_l\left(-\left(\tfrac{\alpha_l}{\rho_l}\psi_l + \tfrac{\alpha_g}{\rho_g}\psi_g\right)\tfrac{dp}{dt} + \tfrac{\psi_l}{\rho_l}\tfrac{dp}{dt}\right) + \alpha_l \nabla \cdot \mathbf{u} \\ &= \alpha_l \alpha_g \left(\tfrac{\psi_g}{\rho_g} - \tfrac{\psi_l}{\rho_l}\right)\tfrac{dp}{dt} + \alpha_l \nabla \cdot \mathbf{u}. \end{aligned} \tag{2.11}$$

Furthermore, to avoid numerical dissipation and retain the sharpness of the interface, it is necessary to include an artificial "interface compression" term $-\nabla \cdot (\alpha_l\,(1-\alpha_l)\,\mathbf{u}_c)$ as a source term on the right-hand side of equation (2.11) to ensure that the interface does not dissolve numerically.

In the above, $\mathbf{u}_c$ is a specially treated vector field only acting on the interface

$$\mathbf{u}_c = c_\alpha\,|\mathbf{u}|\,\mathbf{n}, \tag{2.12}$$

where c_α controls the compression of the interface. As the interface dispersion speed cannot exceed the mixture velocity near the interface in a realistic situation [139], the magnitude of $\mathbf{u}_c$ is constrained to the maximum velocity at the interface and c_α should not exceed 1 and is often set as 1 to retain the sharpness of the interface. $\mathbf{n}$ is the unit normal vector at the interface and can be calculated using the volume fraction α_l

$$\mathbf{n} = \frac{\nabla \alpha_l}{|\nabla \alpha_l|}. \tag{2.13}$$

Equation (2.11) now looks like

$$\frac{\partial \alpha_l}{\partial t} + \nabla \cdot (\alpha_l \mathbf{u}) = \alpha_l \alpha_g \left(\frac{\psi_g}{\rho_g} - \frac{\psi_l}{\rho_l} \right) \frac{dp}{dt} + \alpha_l \nabla \cdot \mathbf{u} - \nabla \cdot \left(\alpha_l \left(1 - \alpha_l \right) \mathbf{u}_c \right). \tag{2.14}$$

In OpenFOAM code, it is written as

$$\frac{\partial \alpha_l}{\partial t} + \nabla \cdot \left(\alpha_l \left(\mathbf{u} + (1 - \alpha_l) \mathbf{u}_c \right) \right) = \alpha_l \left(1 - \alpha_l \right) \left(\frac{\psi_g}{\rho_g} - \frac{\psi_l}{\rho_l} \right) \frac{dp}{dt} + \alpha_l \nabla \cdot \mathbf{u}. \tag{2.15}$$

(iv) Momentum equation

The compressible Navier-Stokes equation reads

$$\frac{\partial \left(\rho \mathbf{u} \right)}{\partial t} + \nabla \cdot (\rho \mathbf{u} \mathbf{u}) = -\nabla p + \nabla \cdot \tau + \mathbf{f}_{st}, \tag{2.16}$$

The second term on the right-hand side of equation (2.16) is the viscous term. The viscous stress tensor of a Newtonian fluid

$$\tau = \mu \left(\nabla \mathbf{u} + \nabla \mathbf{u}^T - \frac{2}{3} (\nabla \cdot \mathbf{u}) \mathbf{I} \right), \tag{2.17}$$

where $\mathbf{I}$ is the unit tensor. The third term $\mathbf{f}_{st}$ represents the surface force acting at the interface of two fluids.

The influence of surface tension is incorporated into the momentum equation following the continuum surface force (CSF) model of Brackbill et al. [140]. The CSF surface tension model can be evaluated as

$$\mathbf{f}_{st} = \sigma \kappa \nabla \alpha_l \tag{2.18}$$

where $\kappa = -\nabla \cdot \mathbf{n}$ is the curvature at the interface and the unit normal to the interface $\mathbf{n} = \frac{\nabla \alpha_l}{|\nabla \alpha_l|}$, where the gradient of volume fraction $\nabla \alpha_l$ ensures that the surface tension force is only applied in the interface region.

(v) Equations of state for the gas and the liquid

The Tait equation [141] is adopted for the liquid phase

$$\rho_l = \rho_\infty \left(\frac{p + B}{p_\infty + B} \right)^{1/n_T}, \tag{2.19}$$

where $n_T = 7.15$ and $B = 3.046 \times 10^8$ Pa. p_∞ and ρ_∞ are the undisturbed pressure and density of the liquid.

The oscillation of the bubble gas is assumed to be adiabatic

$$\rho_g = \rho_{ref} \left(\frac{p}{p_{ref}} \right)^{1/\gamma_h}, \tag{2.20}$$

where ρ_{ref} and p_{ref} are the reference density and pressure of the bubble gas, and γ_h is the ratio of the specific heats of the gas, which is assumed to be constant over the time of the observation [142].

2.1.2 Bubble dynamics and multiphase flow

Bubble dynamics is a highly complex aspect of multiphase flow. Therefore, we utilise the numerical model described above to simulate bubble oscillation. Specific treatments in our simulations are outlined as follows.

(i) Numerical technique for axisymmetric problem in OpenFOAM

The flow field of bubble collapse near a wall is axisymmetric, meaning the fields remain unchanged in the circumferential direction. In such cases, the computational mesh can consist of a wedge-shaped slice of the flow geometry. This type of mesh for axisymmetric

solutions contains one cell across the circumferential direction, reducing the number of cells to two dimensions in the axial and radial directions, as illustrated in figure 2.2. The *wedge* boundary condition is applied to the two sloping side patches.

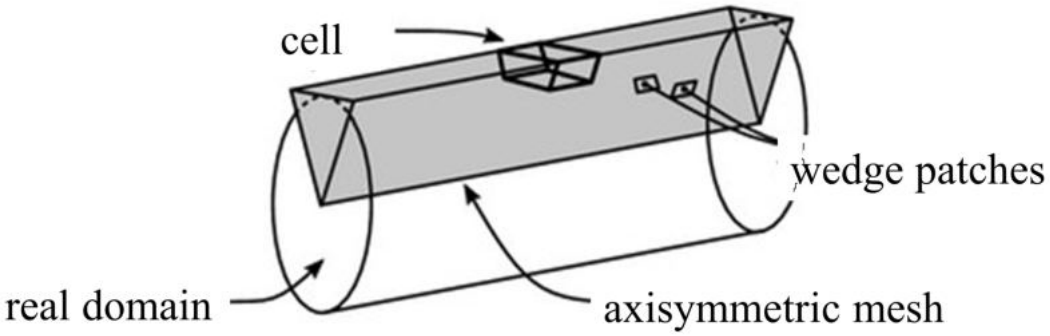

Figure 2.2: Wedge-shaped computational domain.

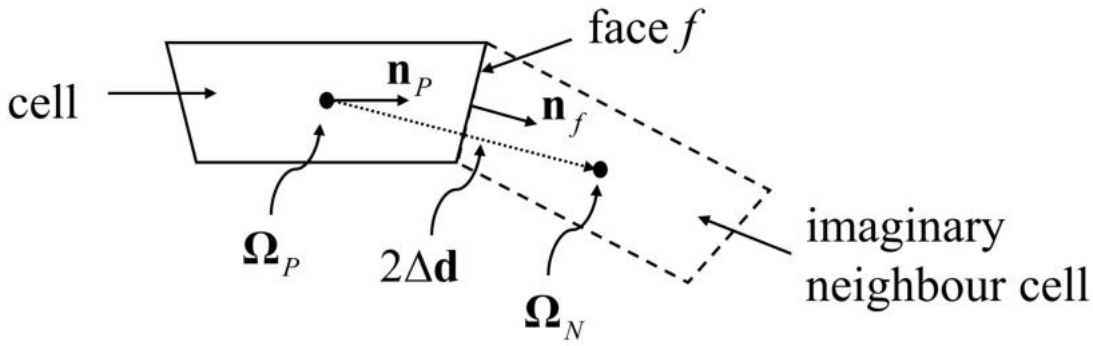

Figure 2.3: Computation of values at the wedge boundary.

As illustrated in figure 2.3, the cell value $\boldsymbol{\Omega}_P$ is transformed to the patch faces using a rotational transformation tensor $\mathbf{R}$ by

$$\boldsymbol{\Omega}_f = G\left(\mathbf{R}_f, \boldsymbol{\Omega}_P\right), \tag{2.21}$$

where P denotes the present cell, $\mathbf{R}_f$ defines a rotation between the unit vector $\mathbf{n}_P$ in the

circumferential direction at the cell centre and the unit face normal vector $\mathbf{n}_f$ by $\mathbf{n}_f = \mathbf{R}_f \cdot \mathbf{n}_P$ and can be calculated using the Euler-Rodrigues rotation formula,

$$\mathbf{R}_f = \mathbf{n}_P \cdot \mathbf{n}_f \mathbf{I} + (1 - \mathbf{n}_P \cdot \mathbf{n}_f)\, \mathbf{k}_f \mathbf{k}_f + \mathbf{n}_f \mathbf{n}_P - \mathbf{n}_P \mathbf{n}_f, \tag{2.22}$$

where $\mathbf{k}_f = \frac{\mathbf{n}_P \times \mathbf{n}_f}{|\mathbf{n}_P \times \mathbf{n}_f|}$. G is the geometric transformation which can be calculated as follows:

(1) $G(\mathbf{R}_f, \boldsymbol{\Omega}_P) = \boldsymbol{\Omega}_P$ for scalar $\boldsymbol{\Omega}_P$;

(2) $G(\mathbf{R}_f, \boldsymbol{\Omega}_P) = \mathbf{R}_f \cdot \boldsymbol{\Omega}_P$ for vector $\boldsymbol{\Omega}_P$;

(3) $G(\mathbf{R}_f, \boldsymbol{\Omega}_P) = \mathbf{R}_f \cdot \boldsymbol{\Omega}_P \cdot \mathbf{R}^T$ for tensor $\boldsymbol{\Omega}_P$.

The gradient at the face $\nabla \boldsymbol{\Omega}_f$ is calculated from $\boldsymbol{\Omega}_N$ in an imaginary neighbour cell by

$$\nabla \boldsymbol{\Omega}_f = \frac{1}{|2\mathbf{d}|} \left[G(\mathbf{R}_N, \boldsymbol{\Omega}_P) - \boldsymbol{\Omega}_P \right], \tag{2.23}$$

where N is the neighbour cell and the rotation between cell centre $\mathbf{R}_N = \mathbf{R}_f \cdot \mathbf{R}_f$.

(ii) Regarding the surface tension force

In numerical simulations in this research, the surface tension coefficient is set to zero to neglect the surface tension force at the bubble surface based on the following two considerations:

Firstly, the continuum surface force (CSF) model has been employed in the volume of fluid method to capture the bubble surface. As depicted in equation (2.18), determining the local curvature and the interface normal vector poses challenges due to the discontinuous nature of void fraction α_l, which hinders the application of conventional discretisation schemes. Inconsistent calculation of the surface tension force can result in parasitic currents. These artefacts significantly restrict the capability of the volume of fluid approach, representing a limitation of the method rather than a numerical inaccuracy [143]. In certain scenarios, parasitic currents may induce strong vortices at the interface without external forcing, poten-

tially leading to catastrophic instability or breakup. Issues with parasitic currents commonly arise in flows with high-density ratios, such as two-phase flows of bubbles in the water.

Secondly, viscous effects become significant when bubbles are tiny. However, lower accuracy in surface tension simulation can lead to parasitic currents at the interface and even instability of the bubble surface, especially when the bubble is small. To address this, a compromise is made in the current research by studying viscous effects through increased viscosity of the liquid in the simulation while maintaining the bubble at a moderately large radius. This approach allows for studying the viscous behaviour of smaller bubbles in water by applying Reynolds number similarity. However, surface tension remains important for smaller bubbles. Achieving Weber number similarity is not guaranteed in this scenario, and dynamic similarity does not strictly apply. The surface tension force has been neglected in numerical simulations to mitigate this issue.

However, neglecting the surface tension force has consequences that must be addressed. Reduced surface tension decreases resistance to interface deformation according to Laplace's law. Compared to smaller bubbles in water where surface tension effects are significant, ignoring the surface tension force in simulations may result in more intense gas–liquid interface deformation and a more concentrated micro-jet during bubble collapse [144]. Additionally, less surface energy is accumulated during cavitation bubble collapse with lower surface tension, leading to weakened collapse intensity and reduced collapse pressure [145].

(iii) Mass conservation correction

It has been noted that due to the segregated nature of the solver for compressible multiphase flow in OpenFOAM, the mass of the bubble undergoes an error over time [63, 146, 147]. To avoid the accumulation of numerical error for the mass of the bubble gas, the density of gas is updated using global mass correction, following Koch et al. [63, 147]:

Assuming that the error occurs homogeneously all over the bubble gas, we enforce the conservation of the mass of the gas phase as follows:

Initially, the mass of the bubble gas is evaluated by

$$m\left(0\right)=\rho_{g}\left(0\right)V\left(0\right), \tag{2.24}$$

where $\rho_{g}\left(0\right)$ and $V\left(0\right)$ are the density of the gas phase and the volume of the bubble at $t=0$.

Similarly, the mass of the bubble gas at time t can be calculated by

$$m\left(t\right)=\rho_{g}\left(t\right)V\left(t\right), \tag{2.25}$$

Assuming no mass transfer between phases, we have

$$m\left(t\right)=m\left(0\right). \tag{2.26}$$

Therefore, the density of the bubble gas at time t can be calculated by

$$\rho_{g}\left(t\right)=\frac{\rho_{g}\left(0\right)V\left(0\right)}{V\left(t\right)}. \tag{2.27}$$

Here, the density of the bubble gas ρ_{g} is assumed to be uniform in space. This approach has been validated by comparison to the experimental data for both spherical and non-spherical bubble cases as a mass error compensation [63, 148]. The disadvantage is that when the bubble collapses into fragments for non-spherical cases, each fragment is treated the same, regardless of the pressure inside the fragments [147].

2.2 Numerical simulation of ultrasonic cavitation using ABAQUS

ABAQUS is a commercial software package for finite element analysis, facilitating the analysis of fluid-structure interaction problems, including scenarios involving cavitation, where the

absolute pressure reaches a critical threshold, using the coupled acoustic-structural analysis strategy. This approach, increasingly employed in recent years, addresses fluid-solid coupling problems. In these simulations, solid elements such as C3D8 (Continuum, 3D, 8-node) are employed to model the structure, while acoustic elements like AC3D4 (Acoustic, Continuum, 3D, 4-node) are utilised for the liquid phase.

2.2.1 Governing equations

(i) Governing equation of the structure and its weak form

Suppose the structure V_s with surface S_s under the action of the body force $\mathbf{f}_b$ obeys the isotropic linear elastic theory. Its displacement $\mathbf{u}_s$ satisfies the linear momentum equation [149]

$$\nabla \cdot \sigma_s + \rho_s \mathbf{f}_b = \rho_s \ddot{\mathbf{u}}_s, \tag{2.28}$$

where ∇ represents the nabla operator, σ_s and ρ_s are the stress tensor and density of the structure, respectively, and $\ddot{\mathbf{u}}_s$ is the second order time derivative of $\mathbf{u}_s$ denoting the acceleration.

Introducing an arbitrary variation displacement field $\delta\mathbf{u}_s$, which adheres to the boundary conditions imposed on $\mathbf{u}_s$, ensuring consistency of behaviour at the boundaries, and integrating equation (2.28) over the structural domain V_s, an equivalent weak form for the linear momentum equation of the structure can be obtained

$$\int_{V_s} \delta\mathbf{u}_s \cdot [\nabla \cdot \sigma_s + \rho_s (\mathbf{f}_b - \ddot{\mathbf{u}}_s)] dV = 0. \tag{2.29}$$

Neglecting all body forces $\mathbf{f}_b$ (such as damping, gravity) and integrating equation (2.29) by parts gives us

$$\int_{V_s} [\nabla \cdot (\delta\mathbf{u}_s \cdot \sigma_s)\, \delta\mathbf{u}_s - \sigma_s \cdot (\nabla \cdot \delta\mathbf{u}_s) - \rho_s \ddot{\mathbf{u}}_s \delta\mathbf{u}_s] dV = 0. \tag{2.30}$$

Using the Gauss theorem with the gradient identity for the first term on the left side of equation (2.30) gives us

$$\int_{S_s} \delta \mathbf{u}_s \cdot \sigma_s \cdot \mathbf{n}^- dS - \int_{V_s} \sigma_s \cdot (\nabla \cdot \delta \mathbf{u}_s)\, dV - \int_{V_s} \rho_s \ddot{\mathbf{u}}_s \delta \mathbf{u}_s dV = 0. \tag{2.31}$$

Given the surface traction $\mathbf{t} = \mathbf{n}^- \cdot \sigma_s$, equation (2.31) can be written as

$$\int_{V_s} \rho_s \ddot{\mathbf{u}}_s \delta \mathbf{u}_s dV + \int_{S_s} \sigma_s \cdot (\nabla \cdot \delta \mathbf{u}_s)\, dV - \int_{S_s} \delta \mathbf{u}_s \cdot \mathbf{t} dS = 0, \tag{2.32}$$

where $\mathbf{n}^-$ is the unit outward normal to the structure surface.

Considering the external surface pressure from the liquid on the fluid-structure interaction, the virtual work can be calculated as

$$\delta W = \int_{S_{fs}} p_s \delta \mathbf{u}_s \cdot \mathbf{n}^- dS, \tag{2.33}$$

where p_s is the pressure acting on the fluid-structural interface S_{fs}. The weak form of the governing equation for the structure, accounting for fluid-structure interaction, can thus be expressed as

$$\int_{V_s} \rho_s \ddot{\mathbf{u}}_s \delta \mathbf{u}_s dV + \int_{V_s} \sigma_s \cdot (\nabla \cdot \delta \mathbf{u}_s)\, dV + \int_{S_{fs}} p_s \delta \mathbf{u}_s \cdot \mathbf{n}^- dS - \int_{S_s - S_{fs}} \delta \mathbf{u}_s \cdot \mathbf{t} dS = 0. \tag{2.34}$$

(ii) Governing equation of the fluid and its weak form

Assume that the liquid V_f with surface S_f is inviscid, compressible and irrotational. The momentum equation of the flow experiencing velocity-dependent momentum losses can be expressed as [25, 149–151]

$$\nabla p_f + \gamma \dot{\mathbf{u}}_f + \rho_f \ddot{\mathbf{u}}_f = 0, \tag{2.35}$$

with the linear constitutive behaviour of the liquid,

$$p_f = -K_f \nabla \cdot \mathbf{u}_f, \tag{2.36}$$

where γ is the volumetric drag, which is neglected in our calculations as it is small compared with the fluid inertia, p_f is the pressure in the fluid, $\mathbf{u}_f$, $\dot{\mathbf{u}}_f$ and $\ddot{\mathbf{u}}_f$ are the displacement, velocity and acceleration of the fluid particle, respectively, ρ_f is the density of the fluid, and K_f represents the bulk modulus of the fluid.

To obtain the partial differential equation used in direct integration transient analysis in terms of pressure p_f, equation (2.35) is divided by ρ_f and the divergence is evaluated with respect to $\mathbf{x}$, where $\mathbf{x}$ is the spatial position. In the absence of the volumetric drag, the result is then combined with the time derivatives of equation (2.36), which results in

$$\frac{1}{K_f}\ddot{p}_f - \nabla \cdot \left(\frac{1}{\rho_f}\nabla p_f\right) = 0, \tag{2.37}$$

where $\ddot{p}_f$ is the second order time derivative of p_f. This is the linear wave equation for the pressure field p_f.

Introducing an arbitrary variation field δp, which adheres to the prescribed boundary conditions of p_f ensuring uniform behaviour across the boundaries, and integrating equation (2.37) over the whole fluid domain V_f, an equivalent weak form for the equation of motion of the fluid can be obtained as follows:

$$\int_{V_f} \left(\frac{1}{K_f}\ddot{p}_f - \nabla \cdot \frac{\nabla p_f}{\rho_f}\right)\delta p dV = 0. \tag{2.38}$$

Integrating equation (2.38) by parts gives us

$$\int_{V_f} \frac{1}{K_f}\ddot{p}_f \delta p dV + \int_{V_f} \frac{1}{\rho_f}\nabla\delta p \cdot \nabla p_f dV - \int_{V_f} \nabla \cdot \left(\frac{\nabla p_f}{\rho_f}\delta p\right) dV = 0. \tag{2.39}$$

Using the Gauss theorem for the last term on the left side of equation (2.39) gives us

$$\int_{V_f} \frac{1}{K_f}\ddot{p}_f \delta p dV + \int_{V_f} \frac{1}{\rho_f}\nabla\delta p \cdot \nabla p_f dV - \int_{S_f} \mathbf{n}^- \cdot \frac{\nabla p_f}{\rho_f}\delta p dS = 0. \tag{2.40}$$

Given the boundary traction $T(\mathbf{x}) = -\frac{\mathbf{n}^- \cdot \nabla p_f}{\rho_f}$, the weak form of the governing equation for

the fluid can thus be expressed as

$$\int_{V_f} \left(\frac{1}{K_f} \ddot{p}_f \delta p + \frac{1}{\rho_f} \nabla \delta p \cdot \nabla p_f \right) dV + \int_{S_f} T(\mathbf{x}) \delta p dS = 0. \tag{2.41}$$

(iii) Fluid-structure interaction modelling

The surface-based interaction is utilised to account for fluid-structure interaction. This capability is suitable for structural and acoustic meshes with disparate node numbering and non-coincident surface meshes [149].

The transient expressions for the coupled acoustic-structural problem are equations (2.34) and (2.41). The fluid-structure coupling condition on the fluid-structure interface S_{fs}

$$\frac{\mathbf{n}^- \cdot \nabla p_f}{\rho_f} + \mathbf{n}^- \cdot \ddot{\mathbf{u}}_f = 0 \tag{2.42}$$

is enforced at the fluid nodes. The displacement of the fluid nodes on the fluid-structure interface is constraint by the structure nodes, and the pressure on the interface is evaluated by

$$\int_{S_{fs}} \left(\frac{\mathbf{n}^- \cdot \nabla p_f}{\rho_f} + \mathbf{n}^- \cdot \ddot{\mathbf{u}}_f \right) \delta p dS = 0. \tag{2.43}$$

2.2.2 Modelling of cavitation

As the detailed micro-processes of cavitation generation remain elusive [14], the one-fluid, cut-off cavitation model is employed to model the generation of vaporous cavitation [1, 40, 152–154].

It assumes that cavitation happens instantaneously when the absolute pressure in the liquid is smaller than a threshold p_c. After considering cavitation, the pressure p_f in the liquid follows

$$p_f = \max\{p_f, p_c\}. \tag{2.44}$$

The one-fluid, cut-off cavitation model solves the governing equations for a single phase, which are used to represent two separate phases of the fluid (e.g., water and vapour). It treats the cavitation region as a homogeneous single-phase area with a constant total pressure equal to the fluid's vapour pressure once the cavitation criterion is met [130]. Although the vapour phase of cavitation is not explicitly considered and is determined by the volume of the region where the pressure falls below the saturated vapour pressure, and the density of cavitation remains the same as that of the fluid and does not change during calculations, the model has successfully approximated global cavitation zones predicted by cavitation models that include phase transition [155, 156].

Chapter Three

The mechanisms of jetting, vortex sheet and vortex ring development in asymmetric bubble dynamics

This chapter is a reformatted and partially edited version of the article:

Y. Yu, J. Cui, W. R. Smith, Q. Wang, and T. G. Leighton. "The mechanisms of jetting, vortex sheet and vortex ring development in asymmetric bubble dynamics". . In: *Physics of Fluids* 35.12 (2023), p. 123320.

Authorship Statement. **Y. Yu**: Conceptualisation, Methodology, Validation, Formal analysis, Data curation, Investigation, Visualisation, Writing - Original Draft; **J. Cui**: Investigation; **W. R. Smith**: Supervision, Writing - Review & Editing; **Q. Wang**: Supervision, Writing - Review & Editing; **T. G. Leighton.**: Writing - Review & Editing.

3.1 Introduction

Based on the following considerations, this chapter studies the viscous bubble dynamics for a Reynolds number of O(10-100). Firstly, viscous effects are essential for cavitation bubbles, whose population comprises mainly tiny bubbles [69]. Secondly, extensive studies have been focused mainly on bubbles with radii of $O(100)$ μm or larger with $Re = O(10^3)$ or larger [9, 24, 55, 56, 58, 62, 63, 66, 67, 70–77, 79–90]. Thirdly, it is well known that the conditions inside a collapsing bubble essentially determine the chemical consequences of cavitation [33, 91]. Our research will accurately simulate the fluid mechanics of the bubble gas during the asymmetric collapse for the first time.

The remainder of this chapter is organised as follows. The experiment setup and the numerical model are described in section 3.2. In section 3.3, experimental results are presented for oscillations of both spherical and non-spherical bubbles. Numerical studies are further performed for bubble dynamics near a rigid boundary in section 3.4, which correlates well with the experimental data, and viscous effects on bubble dynamics are discussed. Finally, the summary of this chapter is given in section 3.5.

3.2 Methodology

In this section, we describe both the experiment setup and the computational model. The experiment uses a high-speed camera for electric spark-generated bubbles in silicone oils. The computational model is based on the volume of fluid method for two-phase viscous compressible flows.

3.2.1 Experiment

The experiment is carried out for electric spark-generated bubbles in silicone oils. Figure 3.1(a) illustrates the experimental setup used to generate a cavitation bubble and record its dynamics. The experiment is performed in a cubic acrylic container (0.3 m × 0.3 m × 0.6 m) filled with the liquid (water or silicone oils) to a depth of 0.2 m. The container is illuminated by a 2 kW LED non-strobe lamp positioned on the opposite side of the camera, passing through a white frosted glass film and a soft light plate. This arrangement allows for a more uniform projection of the light source. The images of the cavitation bubble are captured by a VRI-Phantom V611 high-speed camera working at 7900 frames per second (FPS) for 1280 × 800 resolution.

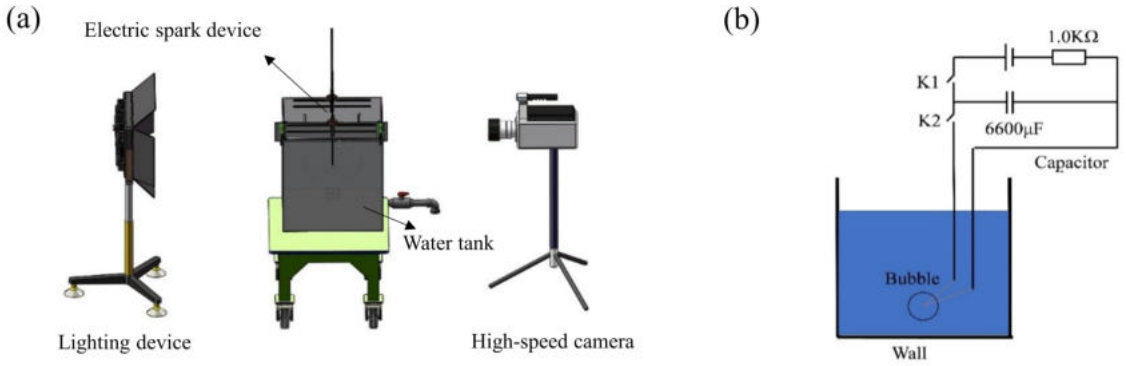

Figure 3.1: (a) Experimental setup used to generate a cavitation bubble and record its dynamics. (b) Underwater discharge circuit.

As shown in figure 3.1(b), the bubble is generated by an electric spark device. It comprises a 205 V DC power supply, a 1 kΩ resistor, a 6600 μF capacitor, and overlapping electrodes made of copper alloy. As mentioned in Cui et al. [157], electrodes extending from the capacitor poles are crossed and touched at their other ends in the liquid. Upon activating switch K1, the capacitor is charged to 205 V to convert 220 V AC into 205 V DC. Subsequently, switch K1 is deactivated and switch K2 is engaged. This discharges the

electronic energy instantaneously, leading to heating at the cross point, bubble generation, and simultaneous activation of the information acquisition button on the high-speed camera. The copper alloy wires, with a thin radius of 0.1 mm compared to the bubble radius of approximately 15 mm, are anticipated to have a minimal impact on the bubble dynamics.

Figure 3.2 shows the configuration of a bubble in the container in the experiment. The dimensionless standoff distance γ is defined as D/R_{max}, where D is the distance from the centre of the initial bubble to the bottom of the container and R_{max} is the maximum bubble radius attained in the experiment. As the bubble is about $7R_{max}$ -$10R_{max}$ from the side walls of the container and the free surface, their effects on bubble dynamics are assumed to be negligible as the amplitude for the spherically symmetric shockwaves emitted by the bubble depends on the reciprocal of the distance travelled.

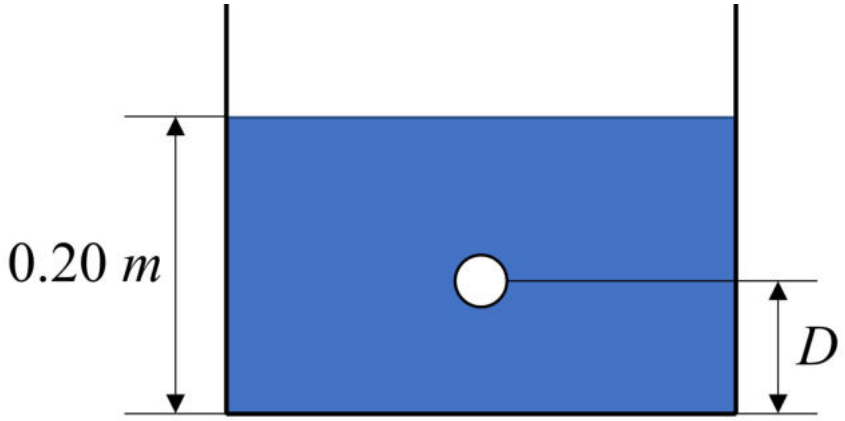

Figure 3.2: Sketch of the bubble in a container filled with the liquid in the experiment.

We choose the length scale R_{max} and the pressure scale $p_\infty - p_v$, where p_∞ is the hydrostatic pressure of the liquid, and p_v is the partial pressure of vapour inside the bubble. The Reynolds number and the Weber number of the bubble are defined as

$$Re = \frac{R_{max}\sqrt{\rho_\infty (p_\infty - p_v)}}{\mu_l}, We = \frac{R_{max}(p_\infty - p_v)}{\sigma}, \tag{3.1}$$

where ρ_∞ is the undisturbed density, μ_l is the dynamic viscosity, and σ is the surface tension

coefficient of the liquid.

3.2.2 Numerical simulation

(i) Numerical model

The governing equations of the numerical model have been fully described in chapter 2. Therefore, in this subsection, we will introduce the non-reflective boundary condition proposed based on the asymptotic behaviour, which reduces the dimension of the computational domain tenfold.

A finite truncated domain is necessary for numerical modelling to represent the infinite liquid domain. To ensure the non-reflection of shockwaves at the external boundary, a large, truncated domain with the dimension being about $100R_{max}$ is necessary [67, 83, 85], leading to a considerable demand for computational resources. Here, R_{max} is a bubble's maximum radius in an unbounded, incompressible, inviscid liquid. In the following, we formulate the far-field boundary condition using the asymptotic solution to reduce the size of the truncated domain and avoid the unphysical reflection of shockwaves at the external boundary.

Wang and Blake [132, 133] developed the weakly compressible theory for non-spherical bubble dynamics based on the compressible potential flow theory, using the method of matched asymptotic expansions. They obtained the asymptotic analytic solution for the flow far away from a bubble oscillating near a rigid flat boundary, in terms of the velocity potential $\varphi(r,t)$

$$\varphi\left(r,t\right)=-\frac{1}{2\pi r}\dot{V}\left(t-r/c\right), \tag{3.2}$$

where $V(t)$ is the transient bubble volume at time t, the over dot denotes the derivative in time t, r is the distance from a field point in the far field to the geometrical centre of the bubble, and c is the speed of sound in the liquid. The liquid velocity $\mathbf{u}\left(\mathbf{r},t\right)$ in the far field

is given as follows:

$$\mathbf{u}\left(\mathbf{r},t\right)=u\left(r,t\right)\mathbf{e}_{r}=\left(\frac{1}{2\pi r^{2}}\dot{V}\left(t-r/c\right)+\frac{1}{2\pi cr}\ddot{V}\left(t-r/c\right)\right)\mathbf{e}_{r}, \tag{3.3}$$

where $\mathbf{e}_r$ is the unit vector from the initial bubble centroid to the field point considered.

The far-field asymptotic solution (3.3) is obtained based on the potential flow theory but stands for the present viscous model, which is justified as follows. The viscous flow velocity $\mathbf{u}\left(\mathbf{r},t\right)$ has the following Helmholtz's decomposition:

$$\mathbf{u}=\nabla\varphi+\nabla\times\mathbf{A}. \tag{3.4}$$

The first component is irrotational and described by a scalar potential $\varphi(r,t)$. The second part is rotational, accounting for all the vorticity of the flow, and is described by a vector potential $\mathbf{A}$. To make this decomposition unique, it is assumed that $\nabla\cdot\mathbf{A}=0$. The vector potential $\mathbf{A}$ can be expressed in terms of the vorticity $\omega\left(\mathbf{r},t\right)$ as follows:

$$\mathbf{A}=\frac{1}{4\pi}\int\limits_{\Omega}\frac{\omega\left(\mathbf{r}',t\right)}{\left|\mathbf{r}-\mathbf{r}'\right|}dV'. \tag{3.5}$$

In this expression, $\mathbf{r}$ is the field point, and $\mathbf{r}'$ is the position of integration element dV' (the source point). The integral domain Ω is the part of the liquid domain, where the vorticity is nonzero, with a length scale of R_{max}.

Klein and Ting [158] analysed the far-field asymptotic behaviour due to vorticity within a finite domain, with the following result

$$\mathbf{A}=O\left(r^{-2}\right),r\rightarrow\infty. \tag{3.6}$$

The velocity contribution stemming from the rotational component is of $O\left(r^{-3}\right)$, and decays faster than the velocity contribution of $O\left(r^{-2}\right)$ originating from the irrotational component. The far-field behaviour of the velocity magnitude is thus given by equation (3.3) to the first two orders of approximation.

The pressure at the far field is obtained from the Bernoulli equation

$$p = p_\infty - \frac{1}{2}\rho_l u^2 + p_d, \tag{3.7}$$

where $p_d(r,t) = -\rho_l \frac{\partial \varphi}{\partial t} = \frac{\rho_l}{2\pi r}\ddot{V}(t - r/c)$. We have

$$\int_0^T p_d(r,t)\,dt = \frac{\rho_l}{2\pi r}\int_0^T \ddot{V}(t - r/c)\,dt = \frac{\rho_l}{2\pi r}\left(\dot{V}(T - r/c) - \dot{V}(0 - r/c)\right) = \frac{\rho_l}{2\pi r}\dot{V}(T - r/c). \tag{3.8}$$

Here we used $\dot{V}(-r/c) = 0$, as the bubble oscillation has not started at time $t = -r/c$.

Substituting equations (3.7) and (3.8) into equation (3.3) yields

$$c\rho_l u(r,T) = \frac{c}{r}\int_0^T p_d(r,t)\,dt + p_d(r,T). \tag{3.9}$$

This equation is similar to the early-time approximations obtained for the fluid-structure interaction by Felippa [159].

Initially, the bubble is spherical, and the flow field can be approximated using the method of images

$$\varphi(r,t) = -\frac{1}{4\pi r}\dot{V}(t - r/c) - \frac{1}{4\pi r_2}\dot{V}(t - r_2/c), \tag{3.10}$$

where r_2 is the distance from a point considered to the image of the initial bubble centroid in the flat rigid boundary. The initial velocity field is obtained using $\nabla\varphi$, and the initial pressure field is obtained using the Bernoulli equation (3.7). The first and second order time derivatives of the bubble volume are obtained from the Keller-Miksis equation for a spherical bubble [50], the derivation of which has been described in Appendix B.

(ii) Numerical setup

Consider an initially spherical bubble of high internal pressure inserted into the liquid at a standoff distance D from the boundary. As the computations are axisymmetric, a wedge-shaped domain with an opening angle of 2 degrees is constructed, with one cell wide in

the azimuthal direction. The two planes shown in figure 3.3(a) are set as the *wedge* type in OpenFOAM to ensure axial symmetry. The essentially two-dimensional computational domain is bounded by the axis of symmetry, the flat rigid non-slip wall, and the non-reflective boundary at a distance of R_{dmn} to the origin in all directions.

Figure 3.3(b) shows the meshing block's cross-sectional view. The grid spacing is uniform in a rectangular domain within the initial bubble. Outside this rectangle, the domain is split as O-block with the spacing growth rate being 1.01. The mesh near the rigid wall is refined to capture the flow within the viscous boundary layer. Figure 3.3(c) shows a schematic diagram of the computational mesh. The adaptive time step is chosen to satisfy the CFL condition [160] with the maximum Courant number being 0.02 when capturing the shockwaves.

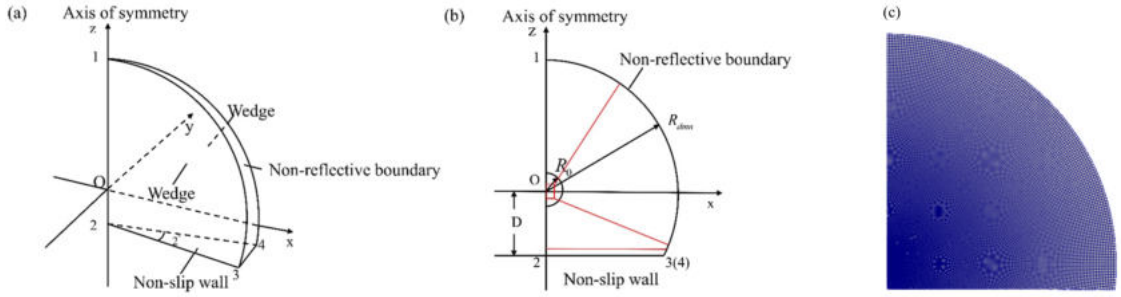

Figure 3.3: Sketch of the geometry and the boundary conditions used for the simulations of bubble dynamics near a rigid boundary. (a) 3D view of the truncated computational domain, (b) 2D projection of the computational domain in the Oxz-plane. An initially spherical bubble of high internal pressure is inserted into the liquid at a distance D from the boundary, and (c) a schematic diagram of the computational mesh.

(iii) Numerical validation

Validation of the non-reflective boundary condition at the far field. Firstly, we validate the effectiveness of the non-reflective boundary condition at the far field. The case considered is a bubble with the maximum radius $R_{max} = 600$ μm at the dimensionless standoff distance $\gamma = D/R_{max} = 1.1$. The initial conditions are $R_0 = 300$ μm, $\dot{R}_0 = 20$ m/s and $p_{b0} = 1500$ Pa. The caption to figure 3.4 provides other parameters used for calculations. This case is calculated with the computational domains being $R_{dmn} = 10R_{max}$ and $100R_{max}$, respectively. Figure 3.4 displays the excellent agreement for the equivalent bubble radius history $R_{eq} = (3V/4\pi)^{1/3}$, although one domain size is ten times larger than the other one. The CPU time is about 50 hours and 71 hours for $R_{dmn} = 10R_{max}$ and $100R_{max}$ respectively, with the Courant number being 0.5. This confirms the accuracy and effectiveness of the non-reflective boundary condition at the far field. Consequently, the domain size is set to $R_{dmn} = 10R_{max}$ for the remaining computations.

Convergence tests. The convergence tests are carried out for various element numbers, with the results displayed in figure 3.5(a) for the time histories of the equivalent bubble radius R_{eq} and figure 3.5(b) for the bubble shapes at its maximum volume during the second cycle of oscillation. The figures display the convergence of the numerical model. The results for the two higher resolutions, $N = 501671$ and 756954, are almost identical for the equivalent bubble radius histories and the bubble shapes. Therefore, $N = 501671$ is chosen for all the remaining calculations.

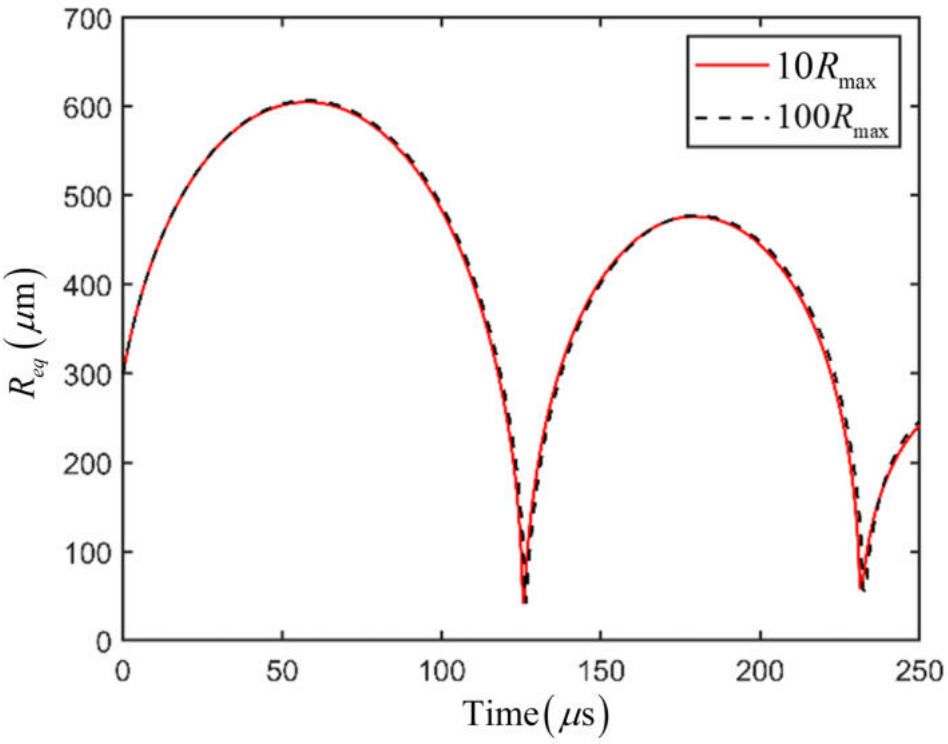

Figure 3.4: Comparison of the equivalent bubble radius histories R_{eq} obtained from different computational domain sizes $10R_{max}$ and $100R_{max}$ respectively, for a bubble with the maximum radius $R_{max} = 600$ μm at the dimensionless standoff distance $\gamma = 1.1$ from a rigid boundary. The initial conditions for the computation are $R_0 = 300$ μm, $\dot{R}_0 = 20$ m/s and $p_{b0} = 1500$ Pa. Other parameters used for calculations are $\rho_\infty = 998$ kg/m^3, $\rho_{ref} = 1.2$ kg/m^3, $p_\infty = p_{ref} = 101315$ Pa, $\mu_g = 1.73 \times 10^{-5}$ Pa $\cdot$ s, $\mu_l = 0.001$ Pa $\cdot$ s, $\gamma_h = 1.4$, $\sigma = 0.072$ N/m, and $c = 1500$ m/s.

3.3 Experimental results

3.3.1 Spherical bubble oscillation in the silicone oil

We first consider a bubble oscillating in an equivalent unbounded domain in the 1000cSt silicone oil with the density ρ_l, the dynamic viscosity μ_l, and the surface tension coefficient σ

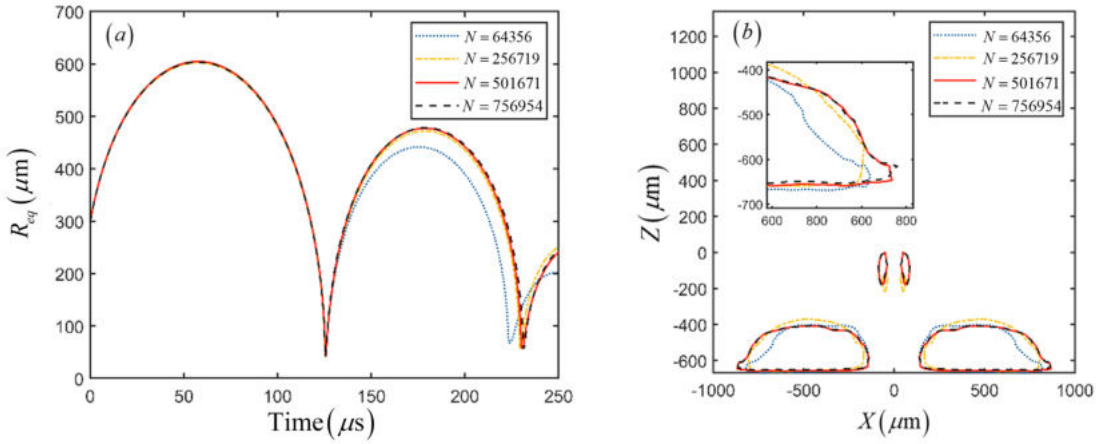

Figure 3.5: Convergence tests in terms of various element numbers: 64356, 256719, 501671, and 756954, for (a) the equivalent bubble radius R_{eq} histories and (b) the bubble shapes. Parameters used for calculations are the same as in figure 3.4.

being 975 kg/m^3, 0.975 Pa·s, and 0.021 N/m, respectively. Figure 3.6 shows the evolution of bubble shapes for two oscillation cycles. The bubble retains a nearly spherical shape during the oscillations. Figure 3.7 compares the equivalent bubble radius R_{eq} with the solution of the Keller-Miksis equation (B.26), where $p_{b0} = 659$ Pa, $R_0 = 14.74$ mm, $p_\infty = 101315$ Pa, $\gamma_h = 1.4$, $\sigma = 0.021$ N/m, and $c = 950$ m/s. As the temperature of the gas is high as a result of the thermal decomposition within the bubble induced by the copper wire, the vapour pressure p_v is set as 31000 Pa in the Keller-Miksis equation to fit with the oscillation period in the experiment. There is good agreement between the experimental results and the Keller-Miksis equation. This agreement justifies the accuracy of the experimental measurements and the Newtonian fluid model with the parameters used in the calculation.

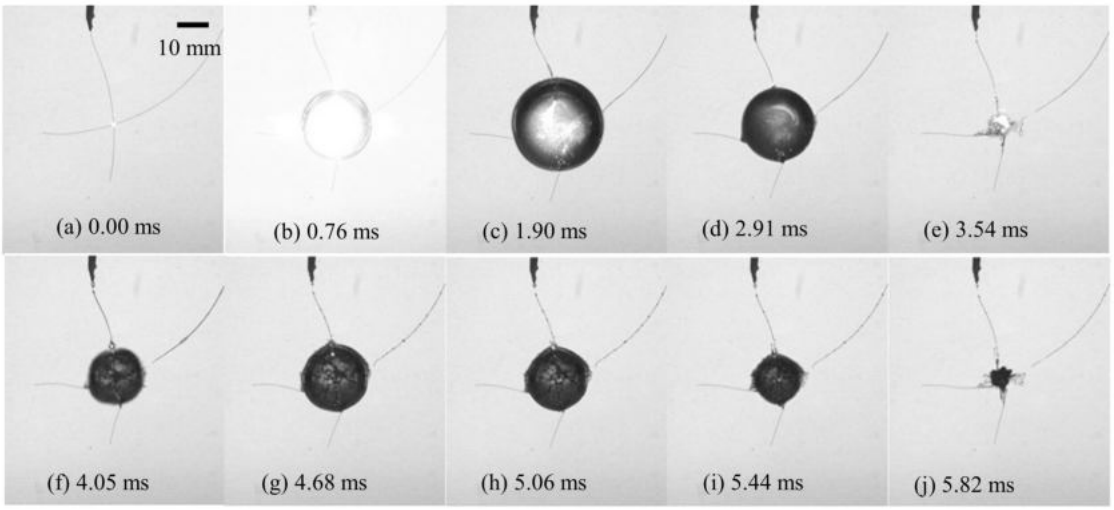

Figure 3.6: The evolution of bubble shapes for a spherical bubble oscillating in the 1000cSt silicone oil with the density ρ_l, the dynamic viscosity μ_l, and the surface tension coefficient σ being 975 kg/m^3, 0.975 Pa $\cdot$ s, and 0.021 N/m, respectively.

3.3.2 Bubble oscillation near a rigid boundary in silicone oils

The dynamics of bubbles near a rigid boundary is now under investigation within three distinct media: water, 500cSt silicone oil, and 1000cSt silicone oil. Properties of the three liquids are listed in table 3.1. The dynamic viscosities of 500cSt and 1000cSt silicone oils are 0.485 Pa $\cdot$ s and 0.975 Pa $\cdot$ s, being much larger than the water viscosity 0.001 Pa $\cdot$ s.

Type of Liquid	ρ_l(kg/m^3)	μ_l(Pa $\cdot$ s)	$\sigma(N/m)$	Re	We	$R_{max}(mm)$	$P_1(ms)$
Water	998	0.001	0.072	1.63×10^5	2.25×10^4	16.35	4.18
500cSt Silicone Oil	975	0.485	0.021	3.08×10^2	7.23×10^4	15.33	3.80
1000cSt Silicone Oil	975	0.975	0.021	1.41×10^2	6.62×10^4	14.03	3.54

Table 3.1: Properties of the liquids used in the experiment, the Reynolds and Weber numbers, the corresponding maximum equivalent bubble radius R_{max}, and the period for the first oscillation cycle P_1.

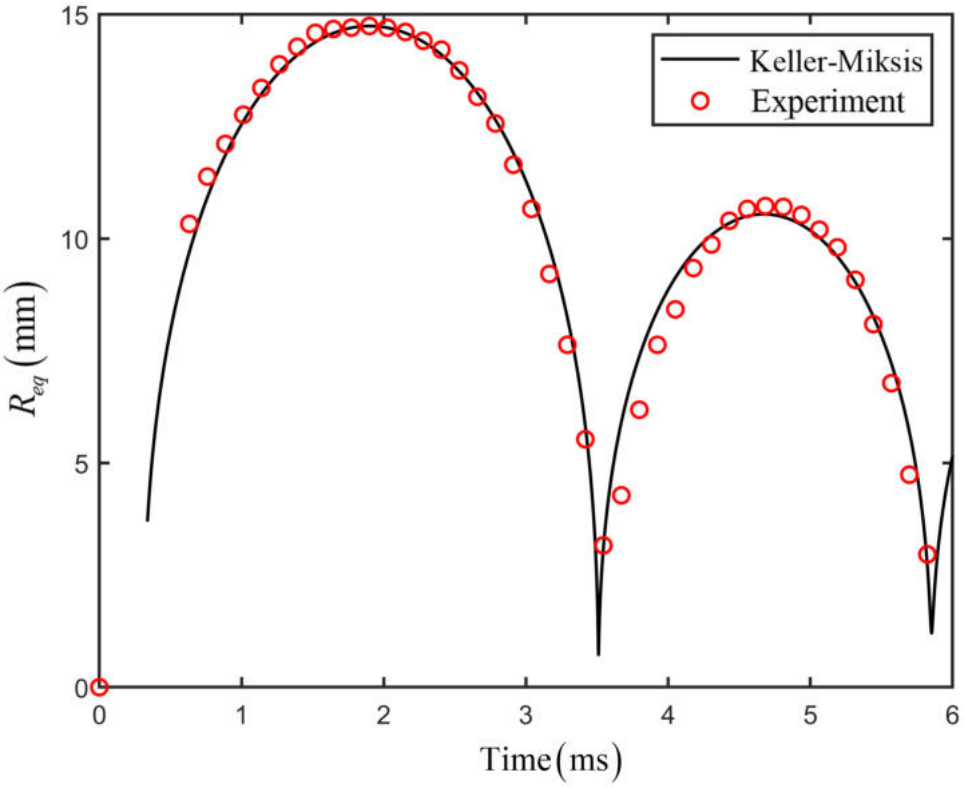

Figure 3.7: Comparison of the equivalent bubble radius R_{eq} history with the solution of the Keller-Miksis equation for a spherical bubble oscillating in the 1000cSt silicone oil for the case in figure 3.6. Other parameters used for the Keller-Miksis equation are $p_{b0} = 659$ Pa, $R_0 = 14.74$ mm, $p_v = 31000$ Pa, $p_\infty = 101315$ Pa, $\gamma_h = 1.4$, $\sigma = 0.021$ N/m, and $c = 950$ m/s.

Figure 3.8 displays the dynamics of a bubble near a rigid flat boundary located at the bottom of each frame for $\gamma \approx 1.4$ in (a) water, (b) 500cSt silicone oil, and (c) 1000cSt silicone oil, respectively. As depicted in figure 3.8(a), the bubble in water initially undergoes spherical expansion in frames (a1)-(a3). Subsequently, it collapses into a vertically elongated prolate spheroid in frames (a3)-(a7). The bubble then collapses predominantly from the upper surface in frames (a7)-(a9). A jet forms and penetrates the bubble during the early stages of the rebound in frame (a9). As the bubble rebounds, the jet penetrates the liquid between

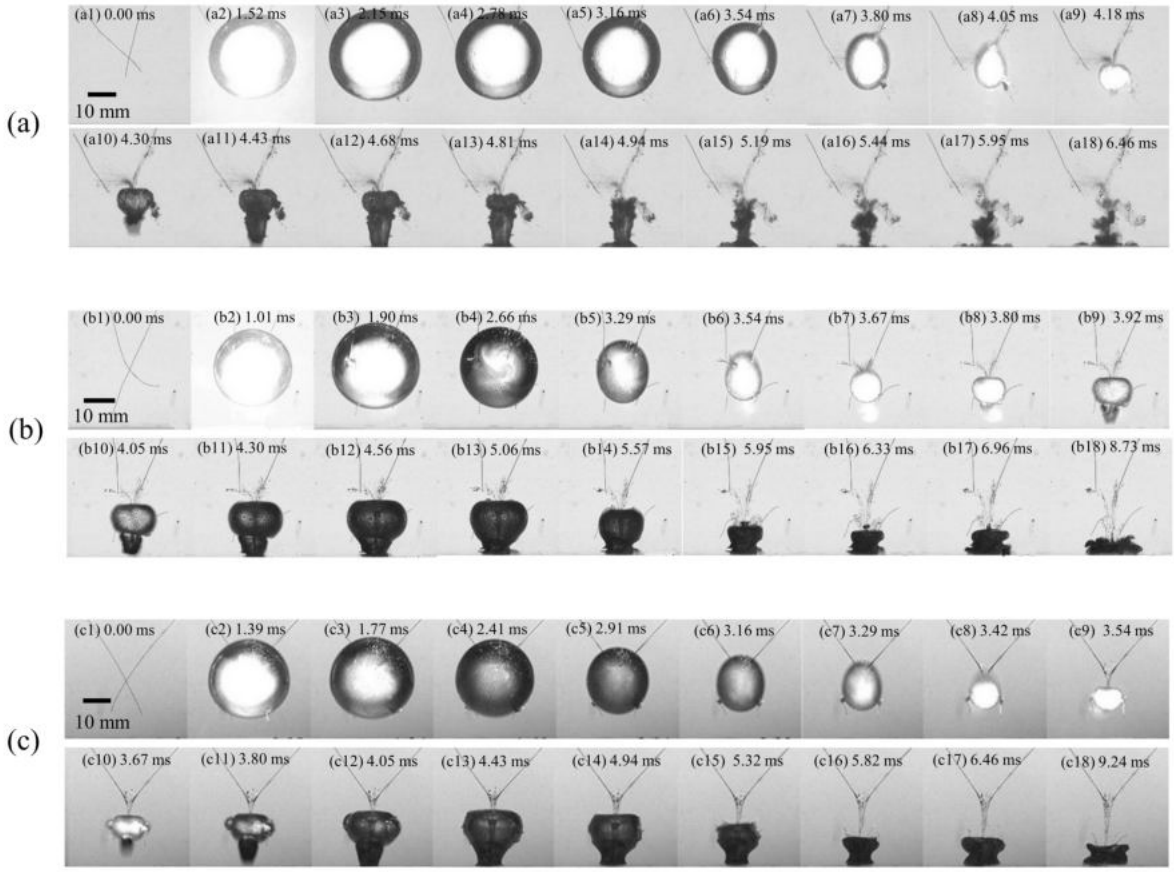

Figure 3.8: The evolution of bubble shapes for a bubble oscillating near a rigid boundary in (a) water with the viscosity μ_l being 0.001 Pa $\cdot$ s, (b) 500cSt silicone oil with the viscosity μ_l being 0.485 Pa $\cdot$ s, and (c) 1000cSt silicone oil with the viscosity μ_l being 0.975 Pa $\cdot$ s at the dimensionless standoff distance $\gamma \approx 1.4$. The densities ρ_l are 998, 975, and 975 kg/m^3, respectively. The surface tension coefficients σ are 0.072, 0.021, and 0.021 N/m, respectively. The maximum bubble radii R_{max} attained in the experiment are about 16.35, 15.33, and 14.03 mm, respectively.

the bubble and the wall, eventually impacting the wall in frames (a9)-(a12). It subsequently re-collapses and migrates to the wall in frames (a12)-(a18) when the instability develops at the bubble surface. The bubble disintegrates towards the end of the second cycle.

Figures 3.8(b) and 3.8(c) display similar features for the bubble dynamics in silicone oils. As in the case of water, the bubble expands spherically, first collapsing to a prolate spheroid, which is elongated vertically and then collapsing predominantly from the upper surface. With much larger viscosities, the bubble maximum radii are smaller in silicone oils, 15.33 mm and 14.03 mm in 500cSt and 1000cSt silicone oils, compared to 16.35 mm in water. This is because of the more significant damping effects in silicone oils. Accordingly, the periods of the first cycle are smaller in silicone oils, being 3.80 and 3.54 ms in 500cSt and 1000cSt silicone oils, compared to 4.18 ms in water.

As in the case of water, a jet forms during the early rebounding of the bubble, penetrating the bubble and then impacting the wall. However, the maximum bubble volume in the second cycle is larger than in water. The bubble then re-collapses and migrates to the wall due to the Bjerknes force of the rigid boundary. In contrast to the scenario in water, the bubble maintains stability during the second cycle in the case of silicone oils. As a result, the jet is visible in frames (b11)-(b12) of figure 3.8(b) and frames (c12)-(c14) of figure 3.8(c). A protrusion of bubble gas encloses and follows the jet after the jet has penetrated the bubble.

3.4 Numerical results

Computational results are presented and discussed in this section. This includes the validation of the computational model with experiments. Attention is paid to the generation and evolution of vortex sheets, vortex rings, flow fields, shockwave propagation, jet development and impact on the rigid boundary, and the shear stress at the rigid boundary. These details are either unavailable or difficult to obtain from experiments.

3.4.1 Comparisons with experiments

We first compare the numerical results with our experimental results for the bubble oscillating in the 500cSt silicone oil with the viscosity being 0.485 Pa $\cdot$ s and Reynolds number being 3.08×10^2 at the dimensionless standoff distance $\gamma \approx 2.0$. The computational domain size is $10R_{max}$ and parameters used for calculation are $R_0 = 10$ mm, $\dot{R}_0 = 12$ m/s and $p_{b0} = 720$ Pa. Other parameters used for calculations are provided in the caption to figure 3.9. The computational results are re-timed for the comparisons.

Figure 3.9 displays the bubble shapes at representative times. The computational and experimental results are shown on the left and right parts of frames (a1)-(f1), respectively. The rigid boundary is at the bottom of frames (a1)-(f1). Frames (a2)-(f2) represent 2D views of the simulated bubbles, while frames (a3)-(f3) present their 3D perspectives. Figure 3.9(a) is for the bubble at its maximum radius when it remains spherical. It then begins to collapse and becomes a prolate spheroid in figures 3.9(b)-(c), and a liquid jet forms at the top of the bubble surface, piercing the lower bubble surface in figure 3.9(d). A toroidal bubble accompanied by a protrusion of the lower bubble surface forms and expands towards the rigid boundary during the rebound in figure 3.9(e) and then reaches its second maximum volume in figure 3.9(f). The computation agrees well with the experiment for a bubble collapsing and rebounding in the 500cSt silicone oil at a moderately large Reynolds number.

We then compare the computational results with the experiment [88] where the Reynolds number is $Re = 6033$. Parameters used for calculations are the same as in figure 3.4. The computational results are also re-timed for the comparisons. Figure 3.10 displays the bubble shapes at representative times. The computational and experimental results are shown on the left and right parts of frames (a1)-(f1), respectively. The rigid boundary is at the bottom of frames (a1)-(f1). Frames (a2)-(f2) represent 2D views of the simulated bubbles, while frames (a3)-(f3) present their 3D perspectives. Figure 3.10(a) is for the bubble

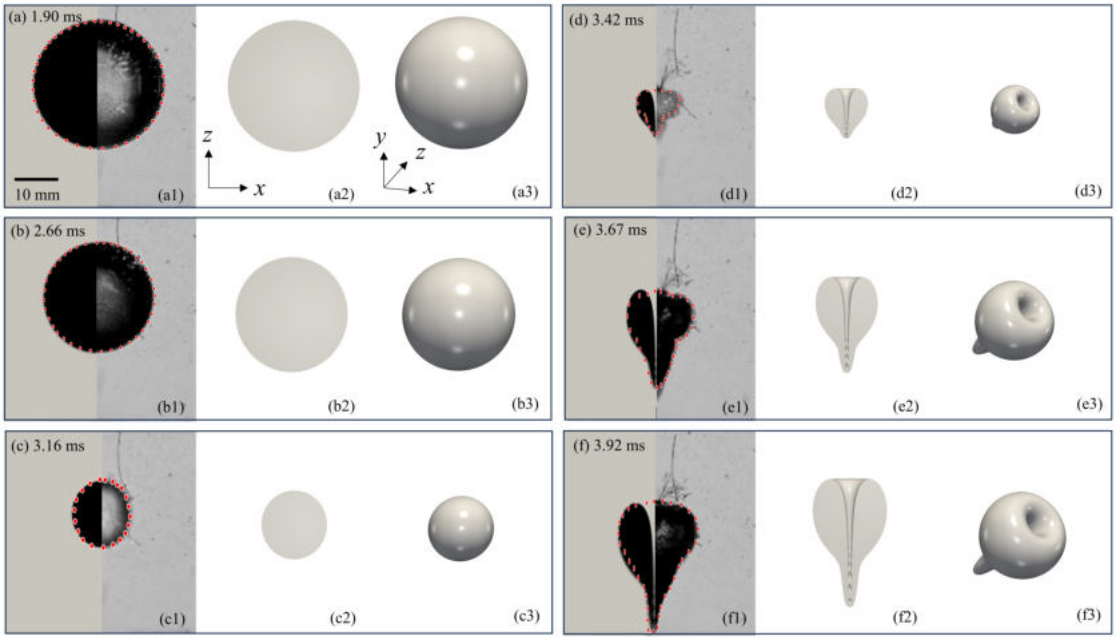

Figure 3.9: Comparison of bubble shapes between the computation and the experiment for the bubble oscillating in the 500cSt silicone oil with the viscosity being 0.485 Pa·s at typical times (a) 1.90 ms, (b) 2.66 ms, (c) 3.16 ms, (d) 3.42 ms, (e) 3.67 ms, and (f) 3.92 ms. Parameters used for the calculation are $R_0 = 10$ mm, $\dot{R}_0 = 12$ m/s and $p_{b0} = 720$ Pa, $\rho_\infty = 975$ kg/m^3, $\mu_l = 0.485$ Pa · s and $c = 950$ m/s, and the remaining parameters are the same as in figure 3.4. The left part in frames (a1)-(f1) is the computational results, while the right is the experimental results. The rigid boundary is the lower boundary of frames (a1)-(f1). The red dot displays the outer profile of the bubble shapes in the experiment. Frames (a2)-(f2) and frames (a3)-(f3) are 2D and 3D views of the simulated bubbles, respectively.

at its maximum radius when it remains spherical apart from its surface near the wall being flattened by the wall. During the late collapse stages, a liquid jet forms at the top of the bubble surface in figure 3.10(b) and impacts at the opposite bubble surface in figure 3.10(c). After the jet penetrates the bubble wall, a toroidal bubble forms, collapses continuously to its minimum volume, and rebounds in figure 3.10(d). It then reaches its second maximum volume in figure 3.10(e) and later re-collapses in figure 3.10(f).

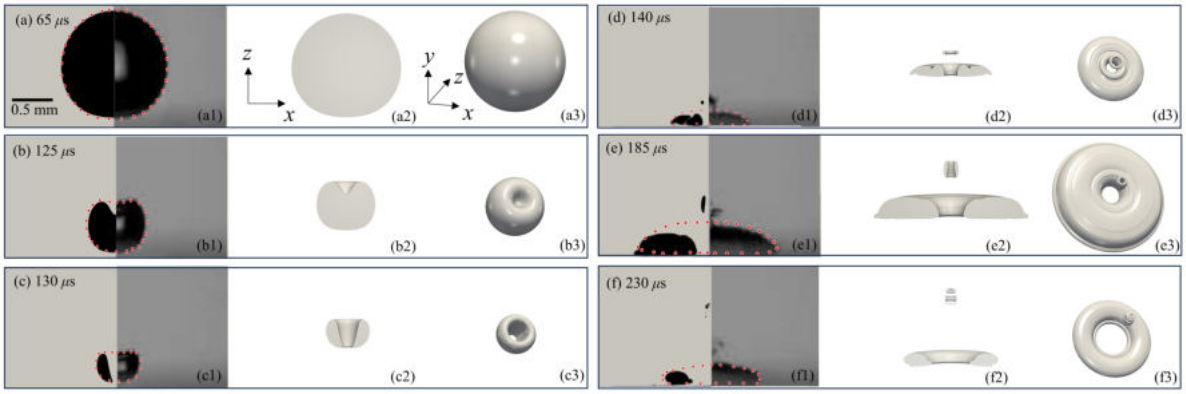

Figure 3.10: Comparison of the bubble shapes between the computation and the experiment [88] at typical times (a) 65 μs, (b) 125 μs, (c) 130 μs, (d) 140 μs, (e) 185 μs, and (f) 230 μs during the two cycles of oscillation. The parameters used for calculation are the same as in figure 3.4. The left part in frames a1-f1 is the computational results, while the right is the experimental results. The rigid boundary is the lower boundary of frames (a1)-(f1). The red dot displays the outer profile of the bubble shapes in the experiment. Frames (a2)-(f2) and frames (a3)-(f3) are 2D and 3D views of the simulated bubbles, respectively.

The computation repeats all these features observed in the experiment for the bubble expansion, collapse, rebound, and re-collapse. The computational results for the bubble shapes agree with those of the experiment during the first and second oscillation cycles. The jet is not observable in the experiments because of the reflection of light off the liquid/gas interface; nevertheless, the outer profile of the toroidal bubble of the computation is in agreement with that of the experiment.

Figure 3.11 compares the equivalent bubble radius R_{eq} history between the computation and the experiment [88]. The excellent agreement is shown for the first and second cycles of oscillation. The relative error of the maximum radius in the second cycle is about 7%, which may be due to the heat transfer and the phase change neglected in the model and/or the measurement errors in the experiment.

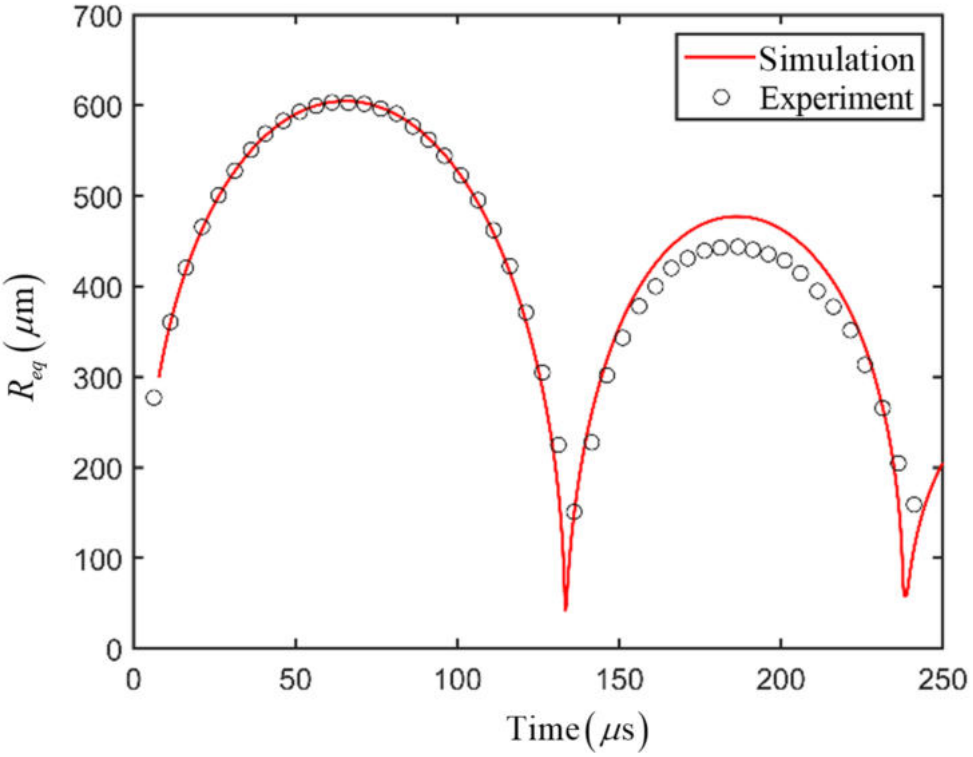

Figure 3.11: Comparison of the equivalent bubble radius R_{eq} history between the computation and the experiment [88] for the case in figure 3.10. The parameters used for the calculation are the same as in figure 3.4.

It is challenging to compute the energy loss of a bubble system associated with the emission of shockwaves at the end of the collapse. Typically, this has been handled by empirically removing a part of the bubble potential energy at the end of the first oscillation cycle [88]. Otherwise, subsequent numerical results are incorrect. Without resetting the rebounding condition, our computational results agree well with the experiments for the second oscillation cycle.

3.4.2 Bubble dynamics near a rigid boundary for $Re = O(10)$

In this subsection, we conduct numerical simulations of bubble dynamics near a rigid boundary for a Reynolds number of $O(10)$ and study the viscous effects on bubble dynamics near a rigid boundary. We will re-compute the case in figure 3.10 for $Re = 6033$ by setting $Re = 75$ (with $\mu_l = 0.08$ Pa $\cdot$ s), with all other parameters kept unchanged.

(i) Vortex ring development

Figure 3.12 displays the streamlines and velocity vectors outside and inside the bubble and the velocity and pressure contours inside the bubble. When the bubble is nearly spherical, a stagnation point exists at the centre of the bubble, from which the streamlines radiate outwards, as shown in figure 3.12(a). The part of the bubble surface furthest from the wall expands faster than the closer part, as the wall hinders the latter. Consequently, the airflow above the stagnation point moves faster than the airflow below the stagnation point, and the airflow above the stagnation point has smaller pressure, as shown in figure 3.12(b). This is consistent with the Bernoulli equation.

As a result of the pressure gradient, the stagnation point moves away from the wall along the axis of symmetry during expansion. Two kinds of streamlines form: concave shape for the upper part and convex shape for the lower part, as shown in figure 3.13(a). The streamlines are becoming denser closer to the upwards-moving stagnation point. The concave- and convex- streamlines tend to converge at the stagnation point with different velocities, and the strong velocity difference leads to the formation of the vortex sheet near the upper bubble surface as shown in figure 3.13(b).

The vortex sheet subsequently approaches the bubble interface and begins transferring momentum to the gas-liquid interface, which in turn influences the flow in the liquid close to the bubble wall. At approximately the maximum bubble volume, the stagnation point meets

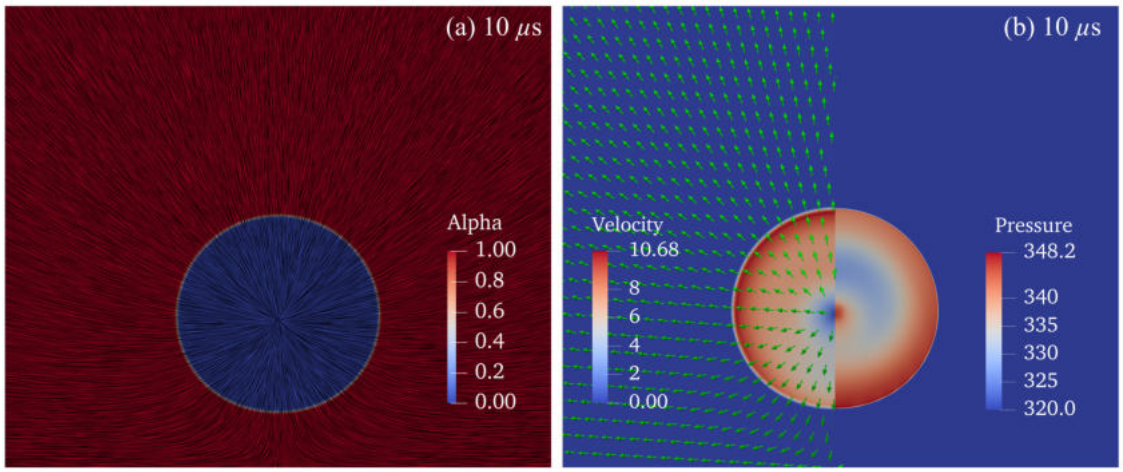

Figure 3.12: (a) Streamlines, (b) velocity vectors (left), velocity contour (left), and pressure contour (right) during early expansion when the bubble is nearly spherical. The Reynolds number is $Re = 75$ ($\mu_l = 0.08$ Pa·s), and the remaining parameters are the same as in figure 3.4.

the bubble surface in figure 3.14(a) and moves out of the bubble afterwards in figure 3.14(b). The part of the vortex sheet within the bubble decays after it meets with the interface, where it is subject to the much higher shear stress from the liquid with a much higher viscosity than gases. Due to the higher pressure zone at the stagnation point, the liquid flow above it is stopped, the part of the bubble surface furthest from the wall collapses first, and the receding bubble surface drags the surrounding liquid towards it. In the meantime, the part of the bubble surface nearest to the wall still expands, pushing the liquid between the bubble and rigid boundary outwards. This generates a circulation around the periphery of the cross-section of the bubble. A vortex ring is accordingly generated within the bubble gas at the outer rim of the vortex sheet.

During the collapse phase, the distal part of the bubble surface from the wall collapses faster, the surrounding liquid flow towards the distal part strengthens, and the vortex ring intensifies, as shown in figures 3.15(a) and 3.15(b). These three events enhance each other

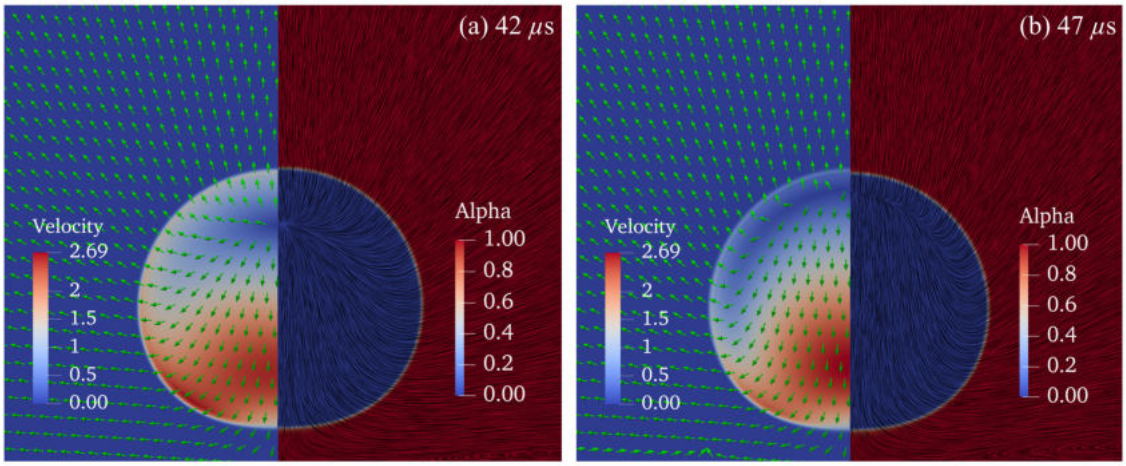

Figure 3.13: Velocity vectors (left in each figure), velocity contours (left in each figure), and streamlines (right in each figure) at (a) 42 μs and (b) 47 μs showing the formation of the vortex sheet generated from the bubble collapse near a rigid boundary for the case in figure 3.12. (Recall that the simulations are axisymmetric when visualising the 3D form of the vortex sheet).

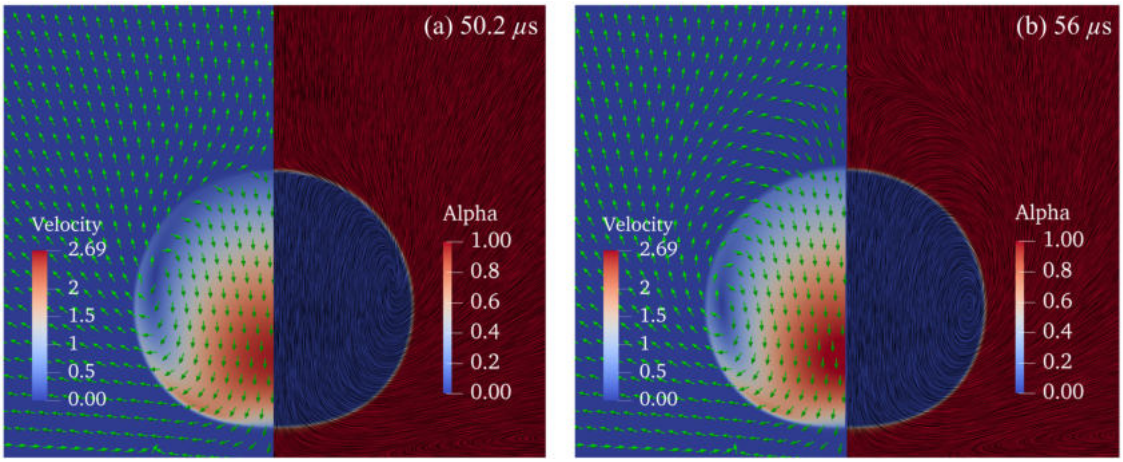

Figure 3.14: Velocity vectors (left in each figure), velocity contours (left in each figure), and streamlines (right in each figure) at (a) 50.2 μs and (b) 56 μs showing the conversion from the vortex sheet to the vortex ring for the case in figure 3.12.

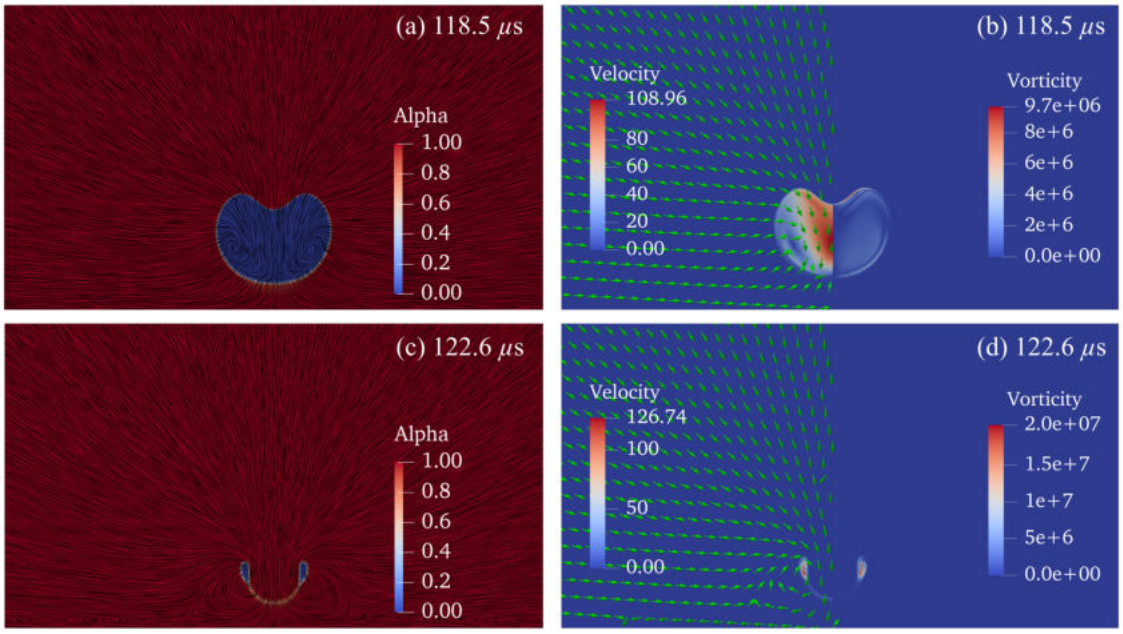

Figure 3.15: Streamlines ((a) & (c)), velocity vectors (left in (b) & (d)), velocity contours (left in (b) & (d)), and vorticity contours (right in (b) & (d)) showing the further development of the vortex ring after generation during bubble collapse for the case in figure 3.12.

during collapse, forming a positive feedback loop. A high-speed liquid jet develops, and it gets accelerated by the vortex ring at the bubble surface, which subsequently penetrates the bubble, from which it is redirected outwards after impacting on the wall as shown in figures 3.15(c) and 3.15(d). This strengthens the circulation around the vortex ring even further.

With the core of the vortex ring inside the bubble gas, much less energy loss occurs than inside the liquid. This is because the energy dissipation of a vortex ring is proportional to viscosity, and most of the energy dissipation occurs near its centre [161]. With its core inside the bubble gas, the vortex ring accelerates the jet like a bearing system.

The vortex ring associated with a toroidal bubble has been an essential topic for bubble dynamics and plays a crucial role in toroidal bubble dynamics [78, 80, 162–165]. With the concept of ideal fluid mechanics, the generation of the vortex ring is attributed to

the topological transform of the liquid domain after the bubble jet penetrates through the bubble. Here, we have revealed that the generation process of the vortex ring takes place within the bubble gas before the bubble jet penetrates through the bubble.

The new results on the vortex sheet and the vortex ring provide two mechanisms for the nanodroplet injection model [33, 91]. Both the decay of the vortex sheet as it interacts with the bubble interface and the vortex ring adjacent to the bubble interface are potential sources of nanodroplets in the hot bubble gas.

(ii) Bubble oscillation and jetting

As shown in figure 3.16, the bubble expands without significant change to the maximum volume from figure 3.16(a) to 3.16(b) for the two Reynolds numbers. At the larger Reynolds number, the jet forms earlier in figure 3.16(c) and develops to a larger and sharper jet in figure 3.16(d). When the jet impacts the opposite bubble surface in figure 3.16(d), the jet at the larger Reynolds number is nearer to the rigid boundary. The bubble for $Re = 6033$ rebounds to a larger maximum volume as shown in figure 3.16(e).

In figure 3.17(a), the equivalent bubble radius R_{eq} histories are compared for the two Reynolds numbers: $Re = 75$ and $Re = 6033$. The first cycle experiences a marginal reduction in both the maximum bubble radius and period at $Re = 75$, attributed to viscous dissipation. For $Re = 75$, a smaller jet is formed in figure 3.16(d), leading to an increase in the kinetic energy associated with the collapse process. Following the more intense collapse, a more significant amount of energy is dissipated through the emission of shockwaves towards the end of the collapse. Consequently, the bubble rebounds to a much smaller maximum radius and period during the second cycle at $Re = 75$.

Figure 3.17(b) shows the jet velocity V_{jet} histories with the time counted from the jet starting in figure 3.16(c) to the jet impacting on the opposite bubble wall in figure 3.16(d).

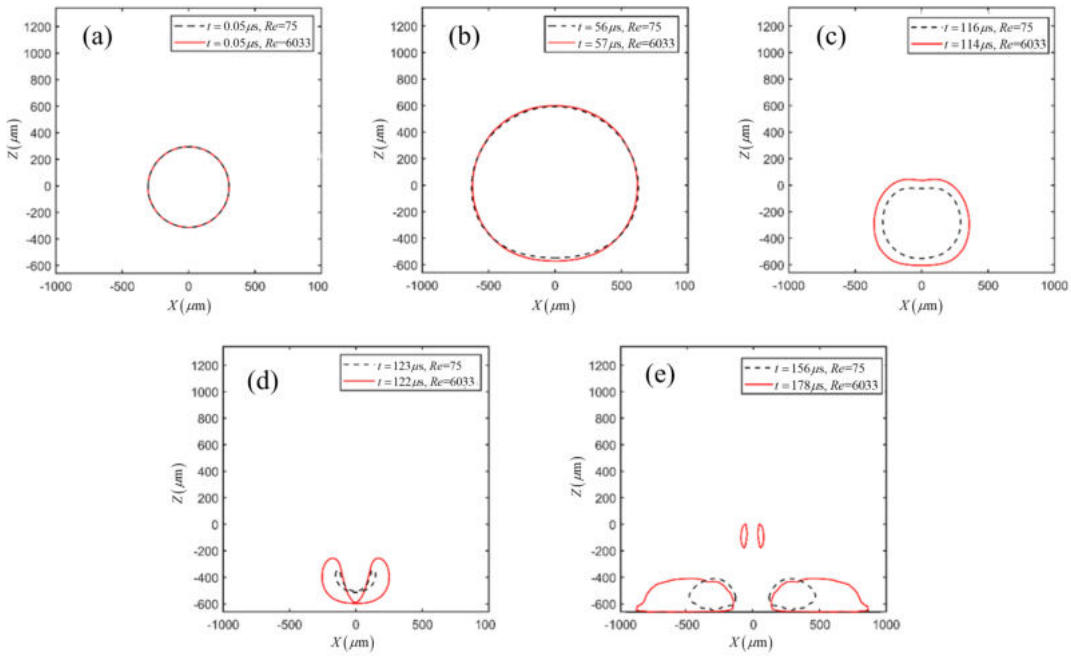

Figure 3.16: Bubble shapes evolutions near a rigid boundary for $Re = 75$, 6033 ($\mu_l = 0.08$, 0.001 Pa · s, respectively). The remaining parameters are the same as in figure 3.4.

For $Re = 6033$, the jet velocity firstly increases with time and then reaches a nearly constant value, which was also observed by Minsier et al. [82]. However, for $Re = 75$, the jet velocity increases continuously before impacting at the opposite surface, and it attains a larger value than for $Re = 6033$.

(iii) Shockwave emission and pressure on the wall

Shockwaves are emitted at the end of collapse and are associated with significant energy loss of the bubble system [81]. The shockwaves are believed to be the leading cause of the erosion of the rigid boundary [8, 9]. The pressure contours in figure 3.18 display the emission and propagation of shockwaves for $Re = 75$. A ring shockwave emits from the bubble ring at the end of the collapse in figure 3.18(a), propagates with a circular cross-section in figure 3.18(b), and impacts itself at the axis of symmetry resulting in a higher pressure in figure 3.18(c).

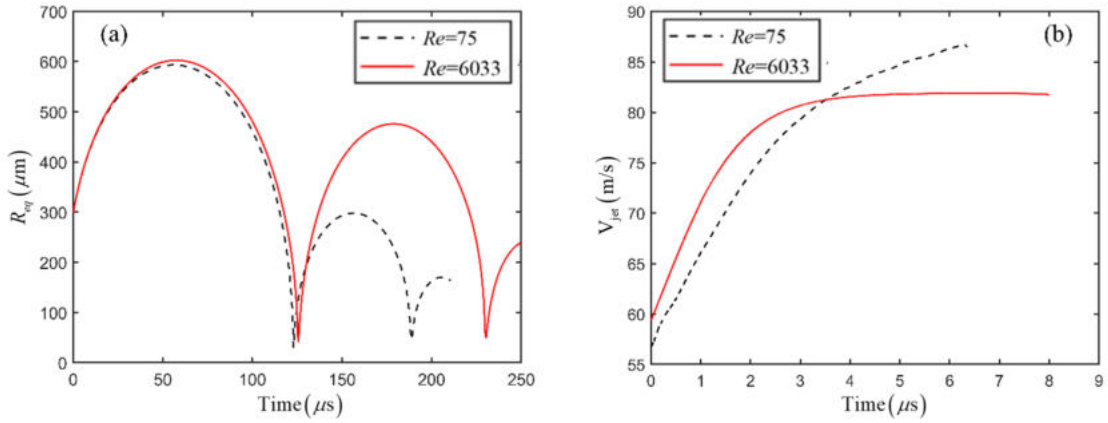

Figure 3.17: Numerical results for $Re = 75$, 6033 ($\mu_l = 0.08$, 0.001 Pa · s, respectively): (a) histories of the equivalent bubble radius R_{eq} and (b) the jet velocity V_{jet}. The remaining parameters are the same as in figure 3.4.

As a result of the further propagation of the shockwaves, two intersection points exist on the symmetry axis where the pressure is higher in figure 3.18(d). The two intersection points move in opposite directions in figure 3.18(e), and a high-pressure region forms when the shockwaves reach the rigid boundary. Subsequently, a clear reflection moving away from the rigid boundary can be observed in figure 3.18(f).

Figure 3.19 shows the pressure on the centre point of the rigid boundary (green spots in figure 3.18) as a function of time for $Re = 75$, 6033. The stronger collapse at $Re = 75$ leads to the stronger shockwave emission, and thus, the pressure on the rigid boundary is also larger. However, the shockwaves are much weaker, and the pressure on the rigid boundary is much smaller at the end of the second cycle for $Re = 75$ due to greater energy loss at the end of the first cycle of oscillation. Since shockwave emission occurs around the end of each collapse and reaches the rigid boundary shortly afterwards, the time taken to reach the first and second pressure peaks for $Re = 75$, 6033 is consistent with the oscillation periods for both Reynolds numbers, as depicted in figure 3.17.

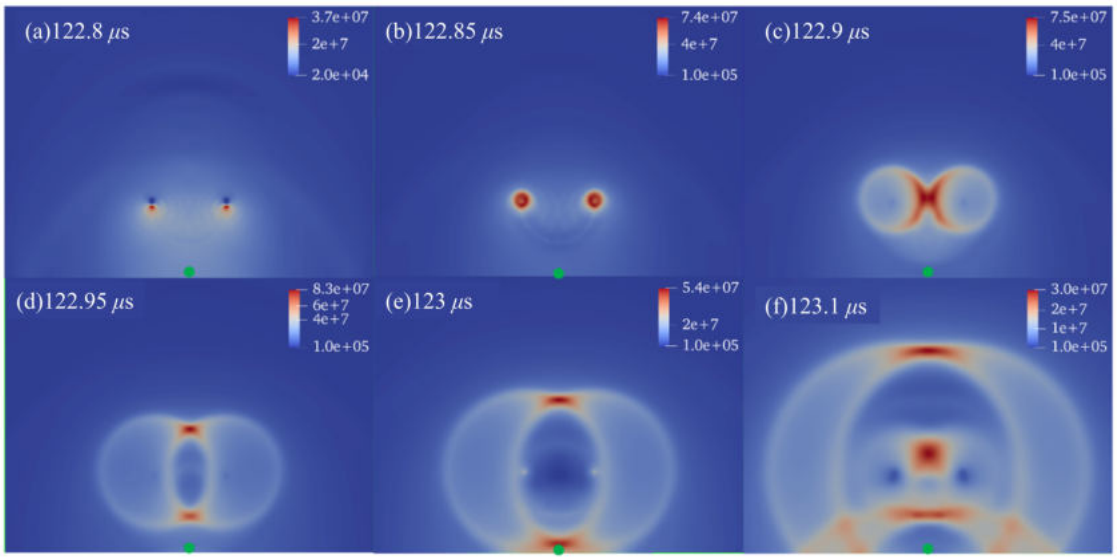

Figure 3.18: Pressure contours showing the emission and propagation of shockwaves generated at the end of the first bubble collapse for the case in figure 3.12.

(iv) Shear stress on the rigid boundary

Figure 3.20 shows the spatial-temporal distribution of the shear stress τ on the rigid boundary for $Re = 75$, using $\log_{10}|\tau|$ due to its large range of values. The direction pointing away from the axis of symmetry is defined as positive and plotted in red. The direction pointing to the axis of symmetry is negative and plotted in blue. As the bubble expands, it drives the liquid outwards, and the shear stress at the wall is outwards. Starting from the late stages of expansion for $t \geq 40$ μs, the shear stress turns inwards far away from the axis of symmetry. The transition from outwards to inwards shear stress corresponds to the stagnation ring.

The mechanism of the stagnation ring is explained as follows. Figure 3.21 shows the flow field distribution at $t = 42$ μs when the bubble is at the late stages of expansion. At certain late stages of expansion, the bubble gas pressure is lower than the hydrostatic pressure. The liquid around the bubble moves outwards owing to its inertia, and the part of the liquid near the wall has less velocity because of the shear stress of the wall. Therefore,

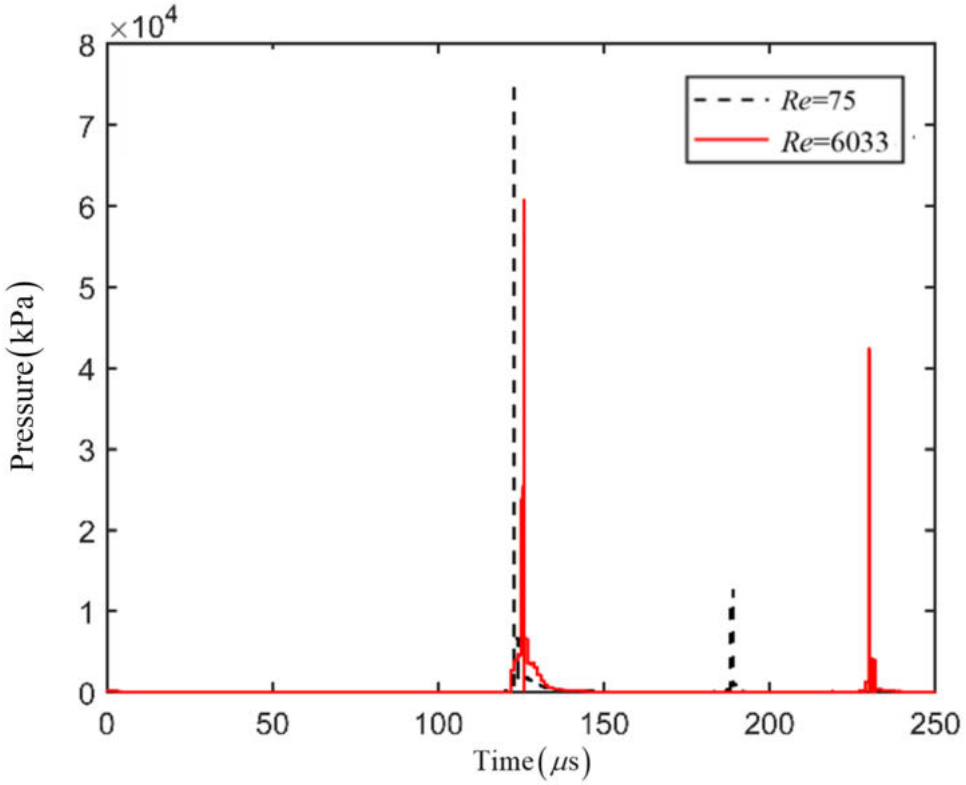

Figure 3.19: Pressure on the centre point of the rigid boundary (green spots in figure 3.18) as a function of time for $Re = 75$, 6033 ($\mu_l = 0.08$, 0.001 Pa$\cdot$s, respectively). The remaining parameters are the same as in figure 3.4.

the reversed flow towards the centre starts near the wall, far away from the axis of symmetry before the end of the expansion, resulting in the stagnation ring occurring before the end of the expansion.

The stagnation ring exists over the wall, with its radius decreasing as the bubble further expands and then collapses. During the late collapse and before rebound for 95 μs $\leq t \leq$ 120 μs, the shear stress is negative everywhere on the boundary and reaches its maximum absolute value. This is generated by the fast-shrinking bubble.

The above feature is repeated during the second cycle of oscillation. During a large

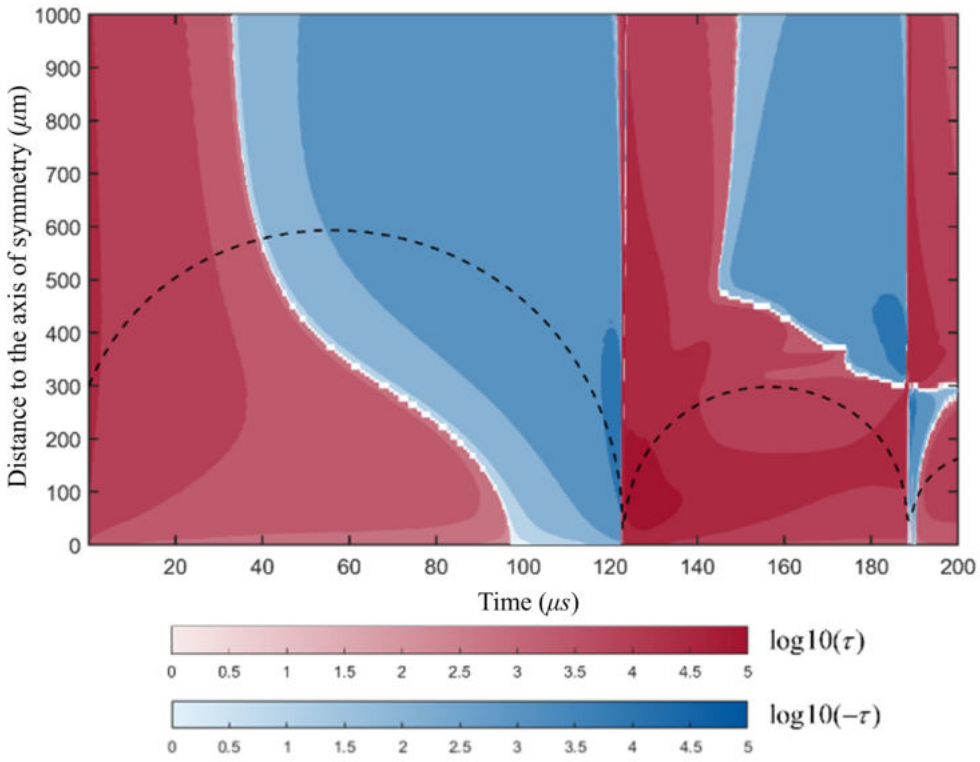

Figure 3.20: The time-space map of the wall shear stress for the case in figure 3.12. The logarithm to the base 10 is taken of the wall shear stress values before plotting due to the large range of values. The first colour bar represents the positive wall shear stress (away from the axis of symmetry), while the second one represents the negative shear stress. Overlaid is the bubble dynamics as a dashed line adapted from figure 3.17(a).

part of the rebounding, the shear stress is outwards everywhere due to the fast-spreading jet along the boundary, and a stagnation ring occurs during the later stages of the rebound, with its radius decreasing with time. However, the shear stress distribution is complex and changes rapidly due to the complex flow field caused by the toroidal bubble collapse at the end of the second cycle.

Figure 3.22 shows the time histories of the shear stress at a probe point on the rigid boundary 180 μm from the axis of symmetry (black spots in figure 3.23). For both cases,

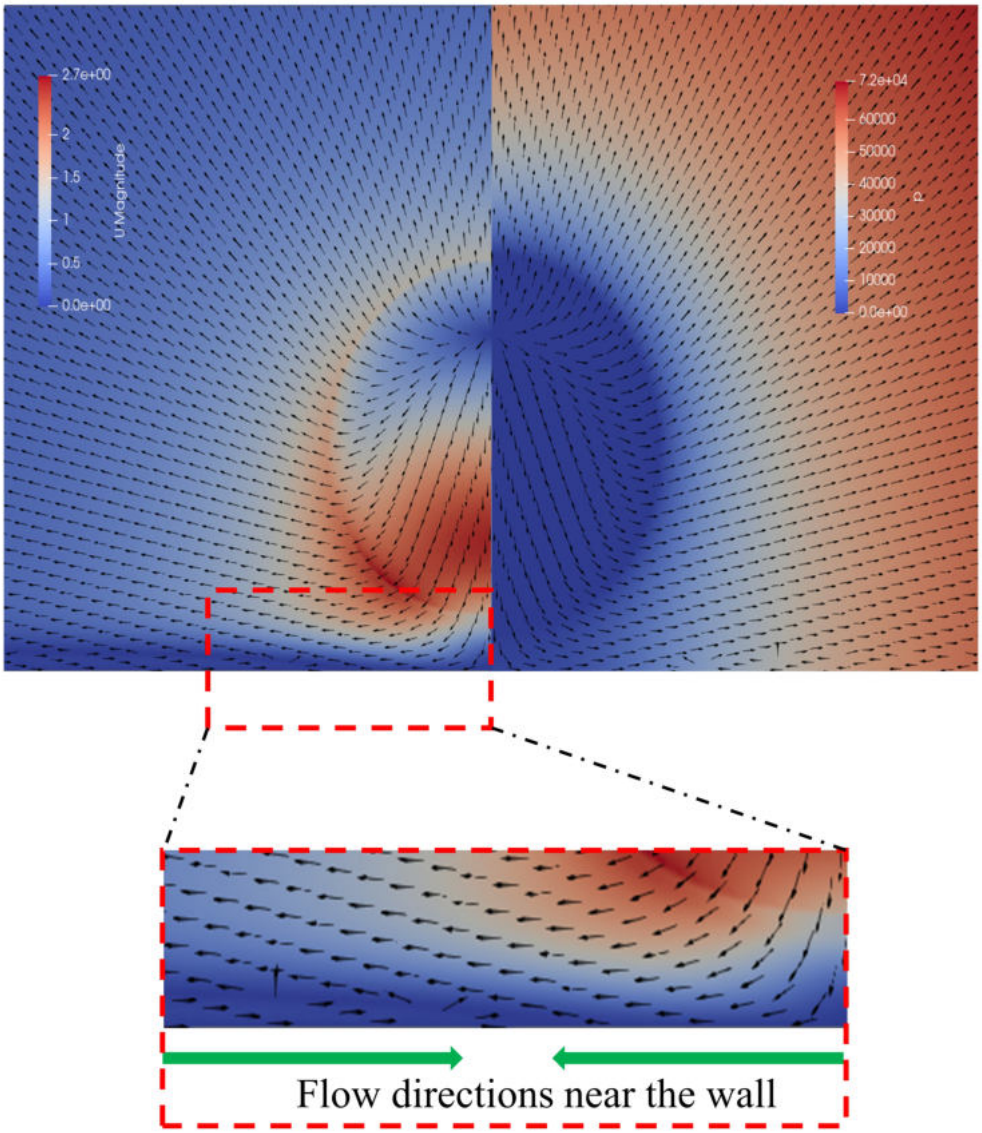

Figure 3.21: Velocity vectors (black arrows), velocity contour (left), and pressure contour (right) at $t = 42$ μs for the case in figure 3.12.

a distinct impulse with a greater magnitude and a shorter period is evident, along with a more gradual impulse characterised by a smaller magnitude and a longer period. The shear stress for $Re = 75$ is larger than that for $Re = 6033$.

Figure 3.23 displays the bubble shapes and the flow fields for $Re = 75$ at different

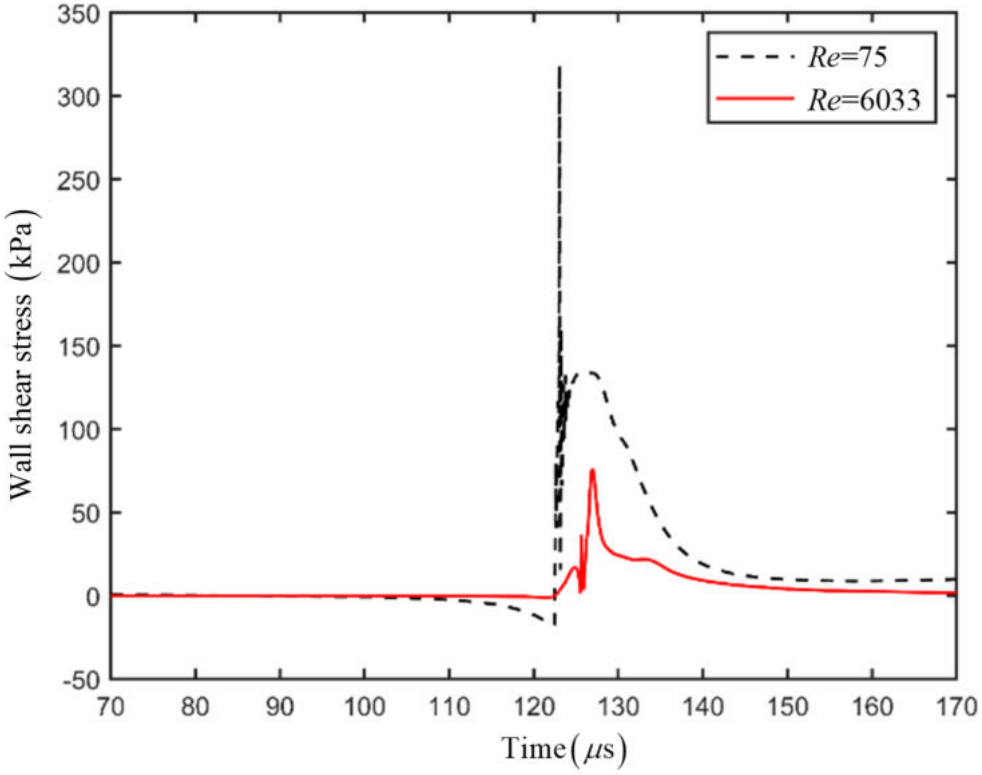

Figure 3.22: The time histories of the shear stress at a point on the rigid boundary, at 180 μm from the axis of symmetry, for Re = 75, 6033 (μ_l = 0.08, 0.001 Pa $\cdot$ s, respectively). Other parameters are the same as in figure 3.4.

times during collapse and rebound, where the probe point is marked as black spots. Figure 3.23(a) is at $t = 120$ μs when the shear stress is negative and small at the probe point. Figure 3.23(b) is at $t = 123$ μs when the shockwaves impact the probe point, resulting in the sharp impulse of shear stress in figure 3.22. Figure 3.23(c) is at $t = 127$ μs, corresponding to the milder impulse of shear stress in figure 3.22, when the jet is spreading along the wall after impacting on the rigid boundary. At $t = 150$ μs in figure 3.23(d), the jet is still spreading, but the magnitude is much smaller, which corresponds to the decreasing wall shear stress in figure 3.22.

In conclusion, when a bubble undergoes inertial collapse near a rigid boundary, sig-

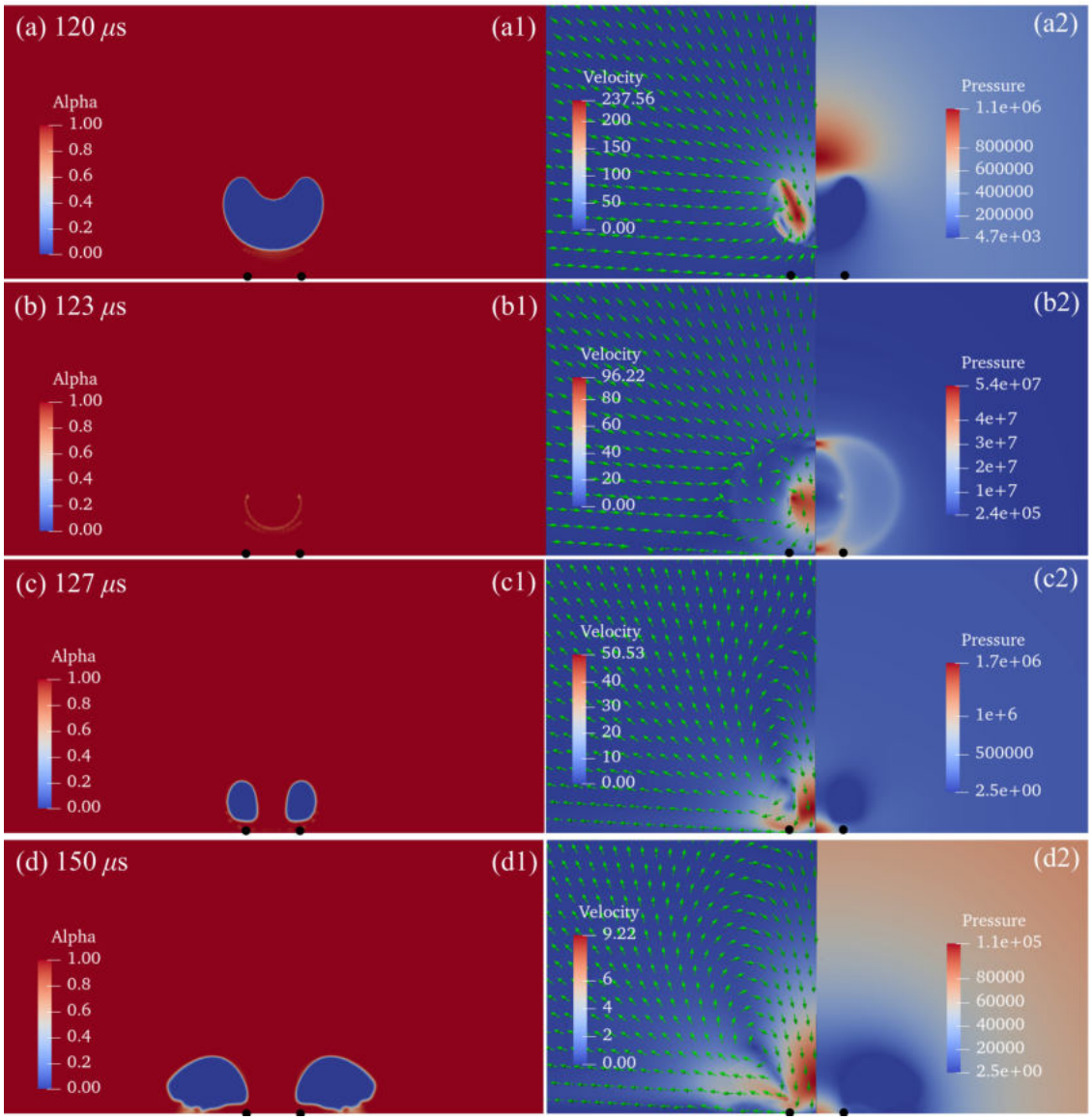

Figure 3.23: Bubble shapes (frames (a1)-(d1)) and flow fields (frames (a2)-(d2)) including velocity vectors (left in frames (a2)-(d2)), velocity contours (left in frames (a2)-(d2)) and pressure contours (right in frames (a2)-(d2)) at (a) 120 μs, (b) 123 μs, (c) 127 μs, and (d) 150 μs during bubble collapse and rebound for the case in figure 3.12.

nificant shear stress emerges primarily during the propagation of the shockwaves along the boundary and the spread of the jet along the boundary. The former has a much higher amplitude, and the latter has a longer period. They both increase with decreasing Reynolds

number.

3.5 Chapter summary

The bubble dynamics near a rigid boundary for Reynolds number O(10-100) is studied experimentally by capturing the spark-generated bubble oscillation in silicone oils. It has also been studied numerically by solving the compressible Navier-Stokes equations by extending the open-source code OpenFOAM with a newly proposed non-reflective boundary condition at the far field based on the asymptotic behaviour. New dynamic features regarding viscous effects and mechanisms underlying the bubble jetting and vortex ring are revealed.

Chapter Four

Cavitation in a periodontal pocket by an ultrasonic dental scaler: a numerical investigation

This chapter is a reformatted and partially edited version of the article:

Y. Yu, M. Mahmud, N. Vyas, W. R. Smith, Q. Wang, and A. D. Walmsley. "Cavitation in a periodontal pocket by an ultrasonic dental scaler: A numerical investigation". In: *Ultrasonics Sonochemistry* 90 (2022), p. 106178.

Authorship Statement. **Y. Yu**: Conceptualisation, Methodology, Formal analysis, Data curation, Investigation, Visualisation, Writing - Original Draft; **M. Mahmud**: Validation; **N. Vyas**: Resources;**W. R. Smith**: Supervision, Writing - Review & Editing; **Q. Wang**: Supervision, Writing - Review & Editing, Funding acquisition; **A. D. Walmsley**: Supervision, Writing - Review & Editing, Funding acquisition.

4.1 Introduction

Previous studies have confirmed that cavitation occurs around dental scaler tips and aids the cleaning process [37, 38, 122]. Increasing the cavitation generated by an oscillating scaler tip will lead to novel clinical approaches to the cleaning process. However, there is currently little understanding of the cavitation behaviour when the scaler tip is in a confined space, e.g., a scaler in a periodontal pocket as shown in figure 4.1(a) [126]. In this chapter, we will study the effects of the hole volume, taper ratio, and immersion depth of the scaler tip on cavitation generation in a periodontal pocket by numerical simulations.

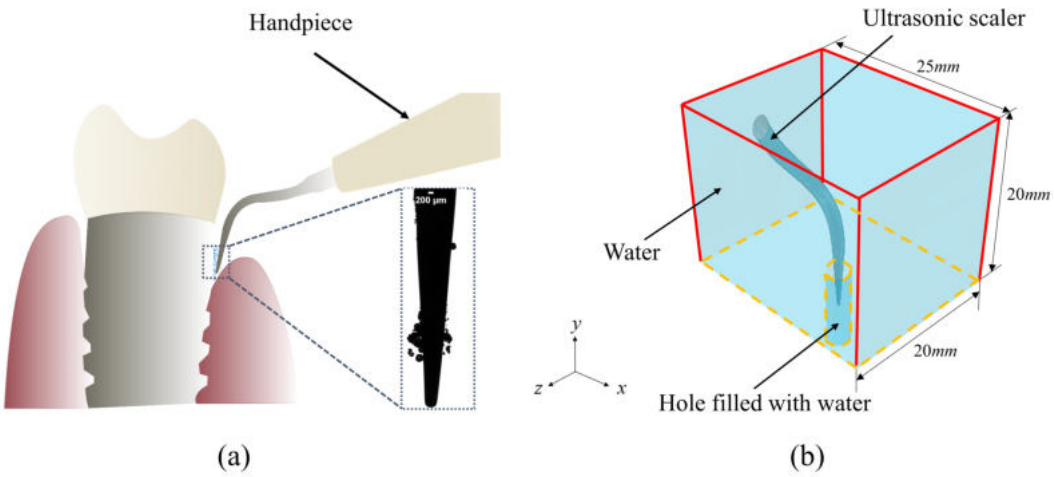

Figure 4.1: (a) Schematic problem description of ultrasonic scaler tip and its vibration in a periodontal pocket [126], and (b) 3D view of the computational domain where the periodontal pocket is simplified to a hole.

The numerical model is described in section 4.2, and it is validated in section 4.3 by comparing numerical results with the experimental data for the displacement at the free end of the scaler and the cavitation pattern near the scaler tip for a scaler operating in unbounded water. In section 4.4, the formation of cavitation due to a scaler vibrating in

a hole is analysed, and parametric analyses have been carried out to study the effects of the hole volume, taper ratio, and immersion depth of the scaler tip on cavitation generation around the scaler tip in the hole. Finally, the summary of this chapter is given in section 4.5.

4.2 Physical and numerical model

4.2.1 Problem description

Considering a dental scaler tip vibrating inside a periodontal pocket (hole) filled with water, as illustrated in figure 4.1(b). A numerical model is described for the three-dimensional, non-linear, and transient interactions between the scaler vibration, the liquid flow, and the cavitation development. The configuration is assumed to be symmetric in a vertical plane, chosen as the Oxy-plane with the y-axis vertical. The cubic part of the computational domain is 25 mm $\times$ 20 mm $\times$ 20 mm in x, y, and z directions, respectively. The section near the circular cylinder base of the scaler is much thicker than the free end of the scaler and does not deform significantly [40]. We thus truncate the part that does not deform with the truncated scaler face S_{ts} as shown in figure 4.2(a), where a prescribed one-dimensional harmonic oscillation along the axis of symmetry of the circular cylinder base is defined. Its displacement is $A\sin(\omega t)$, where A is the amplitude and ω is the angular frequency. The choice of the truncated computational domain size is validated in section 4.3. The vibration of the scaler tip generates pressure waves in water, which results in cavitation formation.

As shown in figure 4.2(b), the truncated part of the scaler is assumed to be an elastic structure with the domain V_s and its surface $S_s = \mathrm{S}_{fs} \cup \mathrm{S}_{ts}$, where S_{fs} is the fluid-structure interface within the truncated computational domain, and S_{ts} is the truncated scaler surface.

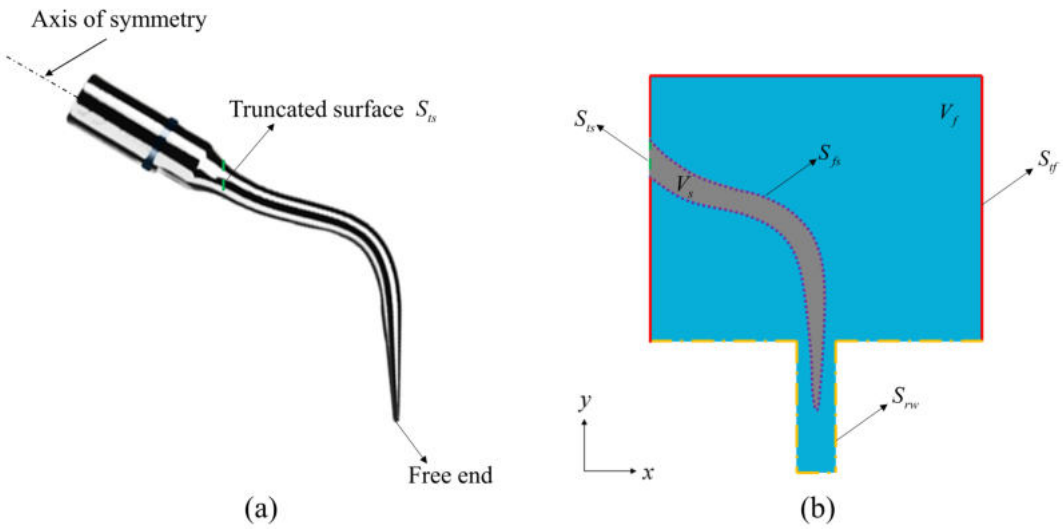

Figure 4.2: The illustration of (a) the scaler with the truncated surface S_{ts}, and (b) the cross-section of the computational domain at the *Oxy*-plane indicating the position of the displacement boundary condition at S_{ts}, the fluid-structure interface S_{fs}, the rigid wall surface S_{rw} and the truncated water planes S_{tf}.

The truncated water domain used for numerical simulations is denoted as V_f bounded by the interface surface S_{fs}, the rigid wall surface S_{rw} consisting of the bottom of the container and the hole wall, and the five truncated water planes S_{tf} of the cubic part of the computational domain. The boundary conditions imposed on these surfaces are introduced in the following subsections.

4.2.2 Numerical model

The weak form for the linear momentum equation of the structure (scaler) can be expressed as

$$\int_{V_s} \rho_s \ddot{\mathbf{u}}_s \delta \mathbf{u}_s dV + \int_{V_s} \sigma_s \cdot (\nabla \cdot \delta \mathbf{u}_s)\, dV + \int_{S_{fs}} p_s \delta \mathbf{u}_s \cdot \mathbf{n}^{-} dS - \int_{S_{ts}} \delta \mathbf{u}_s \cdot \mathbf{t} dS = 0. \tag{4.1}$$

The weak form for the equation of motion of the fluid can be expressed as

$$\int_{V_f} \left(\frac{1}{K_f} \ddot{p}_f \delta p + \frac{1}{\rho_f} \nabla \delta p \cdot \nabla p_f \right) dV + \int_{S_{rw} \cup S_{fs} \cup S_{tf}} T(\mathbf{x}) \delta p dS = 0, \tag{4.2}$$

where $T(\mathbf{x})$ is the boundary traction, determined by the boundary conditions on surfaces S_{rw}, S_{fs} and S_{tf}. The derivations of the weak forms can be found in chapter 2.

Two boundary conditions for the fluid part S_{rw} and S_{tf} except for the interface of fluid-structure S_{fs}, which has been described in chapter 2, should be prescribed. S_{rw} represents the rigid immobile wall where the acceleration of the particles $\ddot{\mathbf{u}}_f = 0$, and we apply this boundary condition by prescribing

$$T_{rw}(\mathbf{x}) = \mathbf{n}^- \cdot \ddot{\mathbf{u}}_f = 0. \tag{4.3}$$

The non-reflective boundary at the truncated water planes S_{tf}

$$T_{tf}(\mathbf{x}) = -\frac{\mathbf{n}^- \cdot \nabla p_f}{\rho_f} = -\frac{\cos(\theta)}{\sqrt{\rho_f K_f}} \dot{p}_f, \tag{4.4}$$

where θ is the angle between the sound wave and the normal to the truncated boundary surface.

The one-fluid, cut-off cavitation model is applied to model the cavitation generated by an oscillating scaler. The details of this model can be found in chapter 2.

4.3 Numerical validations

The water parameters are chosen as follows: the density $\rho_f = 1000$ kg/m^3, the bulk modulus $K_f = \rho_f c^2 = 2140$ MPa, where c is the speed of sound in water and the cavitation pressure threshold $p_c = 2300$ Pa, which is the saturated vapour pressure for water at room temperature of 20 ^{o}C. The scaler (Tip 10P, Acteon Group, USA) is made of stainless steel with

the density $\rho_s = 8000$ kg/m^3, the Young's modulus $E = 224$ GPa, and the Poisson's ratio $\nu = 0.3$ [166]. The amplitude and the angular frequency of the harmonic oscillation of the truncated end of the scaler are chosen as $A = 0.01$ mm and $\omega = 19500$ rad/s (approx. 31 kHz), which could be used for a clinical setting, respectively.

The computational domain is meshed with unstructured tetrahedral meshes with varying densities to fit the computational domain and save CPU time. For the structural part with 0.1 million elements, the mesh size ranges from 0.01 mm near the scaler tip, where a higher displacement occurs, to 0.06 mm near the truncated surface of the scaler. For the fluid part, the mesh size is 0.01 mm in the hole, which is the region of interest in this study, 0.02 mm on the fluid-structural interface and 1.00 mm on the bottom of the cuboid. With the sizes mentioned above, the total element number for the fluid domain is approximately 12 million.

4.3.1 Choice of time step

Choosing an appropriate time step in explicit finite element analysis is critical to prevent exceeding the stability limit, significantly influencing numerical simulation results' reliability and accuracy [149]. As the duration for which a state accurately represents the problem is inherently short, determining the stability limit precisely is often impractical. Therefore, conservative estimates are often utilised, potentially decreasing computational efficiency. In numerical simulations, we utilise the automatic time incrementation feature provided by ABAQUS, which automatically selects increments as close as possible to the stability limit while ensuring high computational efficiency.

4.3.2 Mesh convergence tests

The convergence tests are carried out for various element numbers (coarse: 2 million; medium: 8 million; fine: 12 million; very fine: 16 million), with the results displayed in figure 4.3 for the time history of the cavitation density in the hole. The computational domain with the radius of the circular cylinder hole being 1.5 mm and the depth being 10 mm is adopted. The results for the two higher resolutions are close. Therefore, the mesh resolution for the fine mesh with 12 million elements, as described above, is adopted for all subsequent calculations.

4.3.3 The truncated computational domain

To test if the truncated computational domain is sufficient, we will compare the computational results with two truncated domains, denoted as $V_f \cup V_s$ as shown in figure 4.2(b), and a larger computational domain denoted as $V_f' \cup V_s'$ as shown in figure 4.4(a).

The results compared are the displacement of the scaler tip and the time-averaged cavitation density in the hole over the simulation time 500 μs. With a 20% difference in volume, the displacements for the two fluid domains are very close in figure 4.4(b), and the time-averaged cavitation is 0.319 for $V_f \cup V_s$ and 0.317 for $V_f' \cup V_s'$. Therefore, the smaller truncated computational domain $V_f \cup V_s$ is suitable and chosen for all remaining calculations to save CPU time.

4.3.4 Comparisons with experimental results

We validate the computational results with experiments for the scaler tip vibrating in an unbounded expanse of water, as there are available experimental results for this case. Ex-

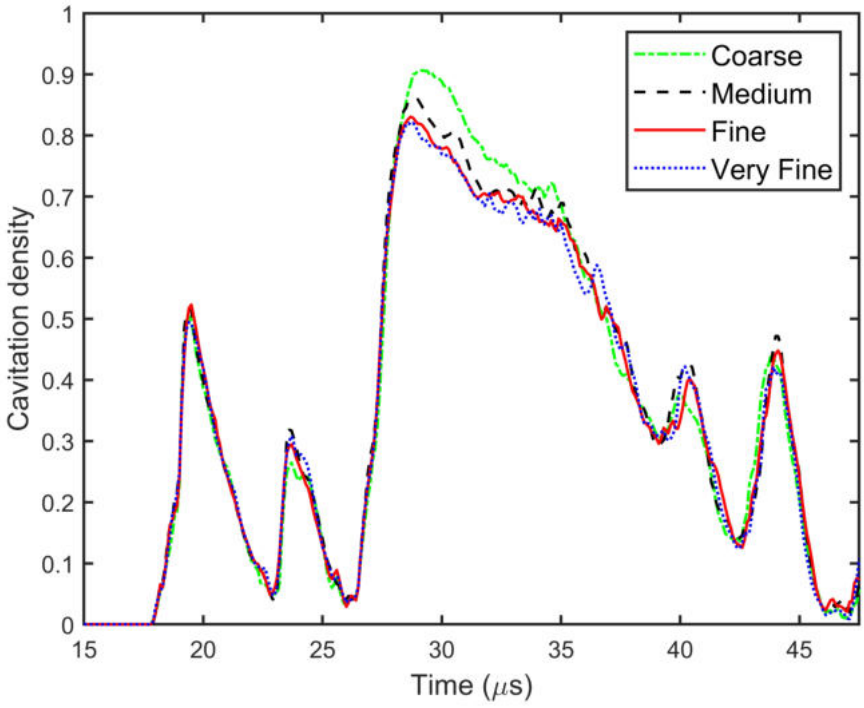

Figure 4.3: Mesh convergence tests regarding the time history of the cavitation density within the hole. Element numbers are 2 million, 8 million, 12 million, and 16 million for coarse, medium, fine, and very fine mesh, respectively. The hole is a circular cylinder shape with radius $r = 1.5$ mm, depth $H = 10.0$ mm and the immersion depth of the scaler tip in the hole $h = 5.0$ mm. The amplitude A and the angular frequency ω of the harmonic oscillation of the scaler handpiece are 0.01 mm and 195000 rad/s (approx. 31 kHz). Other parameters used in the calculations are $\rho_f = 1000$ kg/m^3, $K_f = \rho_f c^2 = 2140$ MPa, $p_c = 2300$ Pa, $\rho_s = 8000$ kg/m^3, the Young's modulus $E = 224$ GPa, and $\nu = 0.3$ [166].

perimental high-speed images were acquired of an ultrasonic scaler tip vibrating in a water tank using a previously described setup [37]. Briefly, a P5 Newtron XS dental ultrasonic scaler was used in conjunction with Tip 10P to generate the cavitation around the scaler. Imaging was done in brightfield mode using a high-speed camera (Fastcam mini AX200, Photron, Japan). The scaler position was fixed by attaching it to an *xyz* translation stage

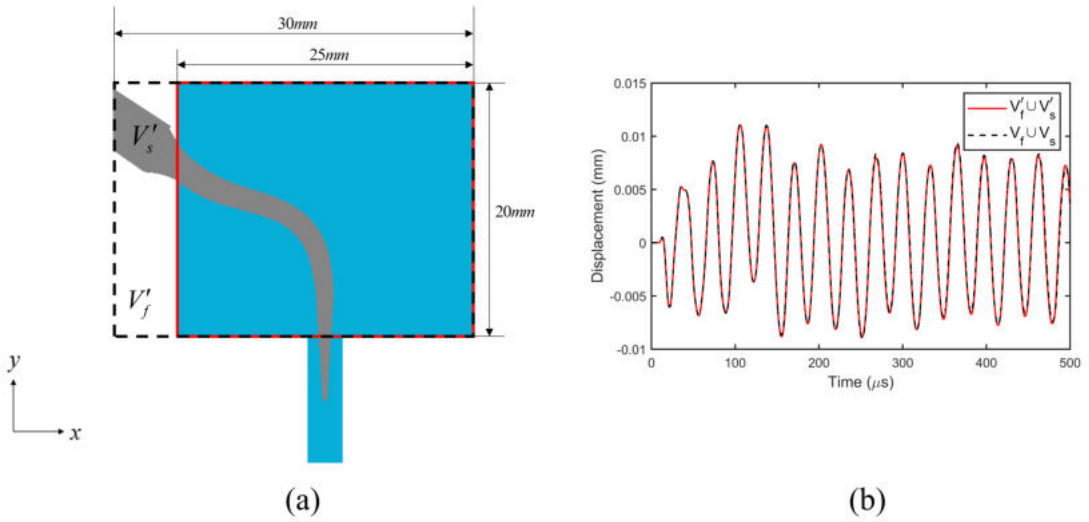

Figure 4.4: (a) Illustration of the two truncated computational domains at Oxy-plane with different sizes. (b) Comparison of the displacement of the free end of the scaler tip along the x-axis for the computational domains $V_f \cup V_s$ and $V_f' \cup V_s'$. Other parameters used in the calculations are the same as in figure 4.3.

(PT3, Thorlabs Inc, NJ, USA) and a high-precision rotation mount (PRO1/M, Thorlabs Inc, NJ, USA). The axial rotation of the scaler tip was maintained during experiments.

We compare the computational results with experiments in terms of the displacement of the free end of the scaler tip denoted by "+" in figure 4.5(b), as well as the cavitation pattern around the scaler tip. The boundary condition for the surface S_{rw} of the fluid domain in figure 4.2(b) is set as the non-reflective boundary (equation 4.4) to satisfy the equivalent infinite fluid domain in the experiment. Figure 4.5(a) depicts the comparison of the scaler tip displacement in the global x-direction. For the first few oscillation cycles, the computational results are associated with some transient oscillations as the initial conditions are set as the quiescent water flow. In contrast, the experimental data were recorded after many cycles with repeated steady oscillation. After the first few cycles, the displacement of the computational results rapidly stabilises and agrees well with the experimental data.

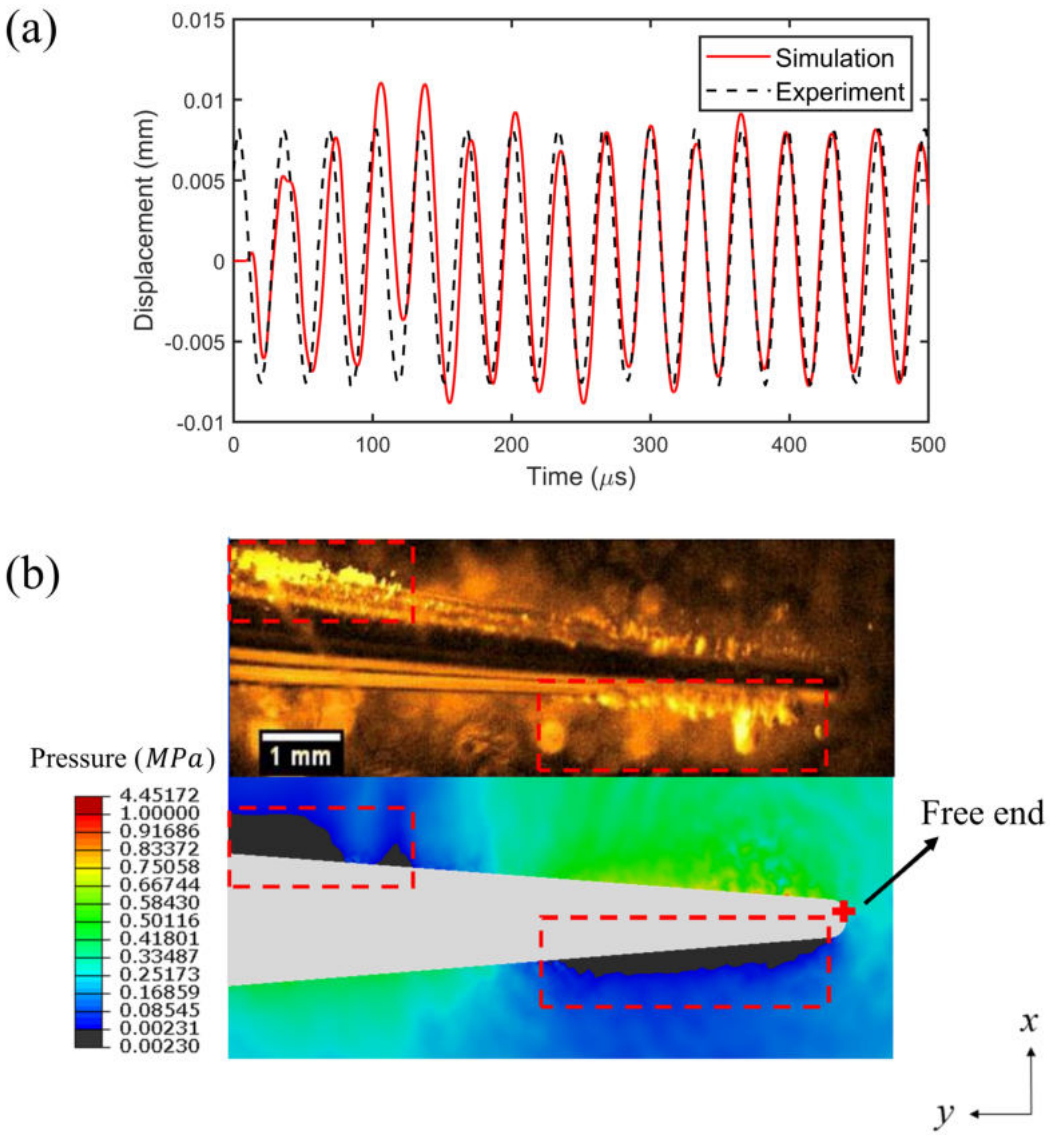

Figure 4.5: Comparisons with experiments in terms of (a) the displacement of the free end of the scaler tip denoted by "+" in figure 4.4(b) along the x-axis, and (b) the cavitation pattern (black area) around the scaler tip at $t = 348.5$ μs in the simulation on Oxy-plane and in the experiment. Parameters used in the calculations are the same as in figure 4.3.

Figure 4.5(b) displays the contours of the pressure in the fluid where the predicted area of cavitation is in black at $t = 348.5$ μs and the corresponding experimental image of

the cavitation zone near the straight part of the vibrating scaler tip [37]. The computational results display two cavitation zones, shown in the dashed rectangles; one is beneath the tip, near the tip end, and the other is above the tip and away from the tip end. The present model predicts the main cavitation zones well. Some other bubbles can also be observed in the experiment from figure 4.5(a). This discrepancy could be due to the inaccuracy of the present model and/or the pre-existing air bubbles that grow due to rectified diffusion [167, 168].

4.4 Numerical results

A parametric study has been carried out to investigate the cavitation density in the hole in terms of the hole volume, taper ratio of the hole, and immersion depth of the scaler tip. The depth of the holes in our simulations is 10 mm, considering advanced periodontitis where the periodontal pocket depth can reach 10 mm or deeper [169]. Considering safety in a clinical setting, the vibrating scaler should not touch the tooth or the gum tissue. Therefore, our simulations adopted a wide range of hole sizes and immersion depths corresponding to the safety concerns, which will be provided in the following subsections. The simulation time is 500 μs for each case, and the time-averaged cavitation density is evaluated for comparisons.

4.4.1 Cavitation around a scaler tip

Figure 4.6 compares the pressure contours for a scaler tip vibrating (a) in an unbounded, infinite domain and (b) in a hole. For a scaler tip vibrating in the infinite domain, the pressure contour is only shown within the corresponding liquid domain for the scaler tip oscillating in a hole. The results demonstrate that much more cavitation is generated around the scaler tip vibrating in a hole. The average energy of acoustic wave per unit volume e is related to

the pressure wave amplitude p_f by [170]

$$e = \frac{{p_f}^2}{2\rho_f c^2}. \tag{4.5}$$

For the scaler tip placed in a hole with rigid boundaries, more ultrasonic energy will be confined in the hole in the form of pressure waves with higher amplitude. Thus, the pressure in the liquid is more likely to be lower than the vapour pressure, resulting in a higher likelihood of cavitation formation in the hole.

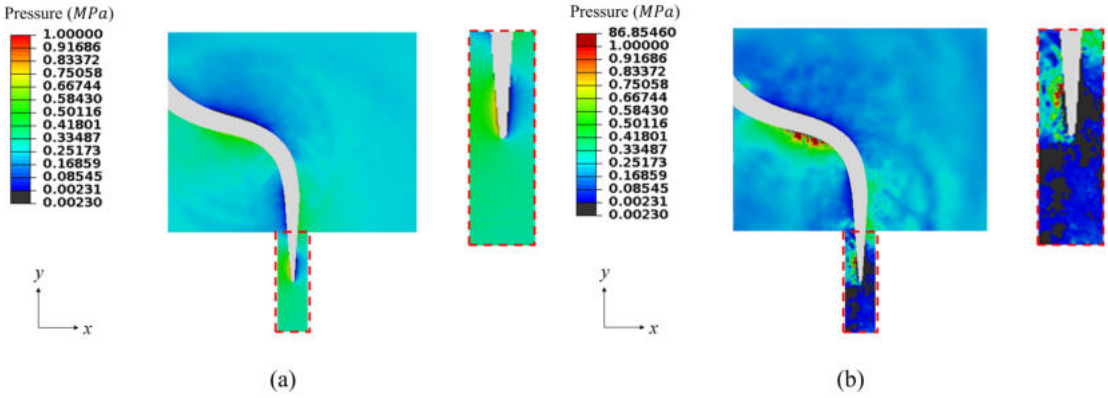

Figure 4.6: Pressure contours showing the cavitation pattern for a scaler vibrating in (a) an unbounded, infinite domain, and (b) a hole at $t = 399$ μs. The black area denotes the area of cavitation. Other parameters used in the calculations are the same as in figure 4.3.

4.4.2 Effects of the hole volume

Figure 4.7(a) shows the schematic diagram for a dental scaler vibrating at dimensionless immersion depth h/H of 0.5 in circular cylinder-shaped holes with the depth of the hole H being 10 mm and the radius r being 0.8, 1.5 and 2 mm, respectively. The volume of each hole is approximately 20.1, 70.7, 125.7 mm^3 respectively.

Figure 4.7(b) shows that the time-averaged cavitation density increases as the hole volume decreases. As the time-averaged energy introduced into the fluid in the hole from

the vibrating scaler is constant, the ultrasonic energy per unit volume increases with the hole volume decreasing. This results in stronger ultrasonic pressure waves in the hole and produces more cavitation in the hole.

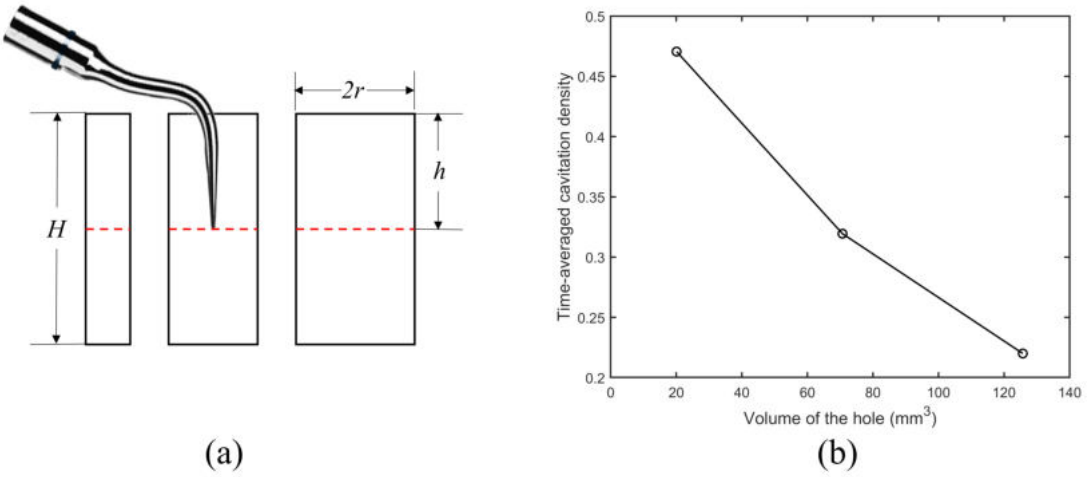

Figure 4.7: (a) Schematic diagram for a dental scaler vibrating in holes with the volume being approximately 20.1, 70.7, 125.7 mm^3 (from left to right). (b) Time-averaged cavitation density in the hole versus the volume of the hole. The dimensionless immersion depth of the scaler tip in the hole is 0.5. Other parameters used in the calculations are the same as in figure 4.3.

4.4.3 Effects of the taper ratio

The taper ratio is defined as $\eta = r_o/r_b$, where r_o and r_b are the radius of the circular opening and bottom of the hole, respectively. Figure 4.8(a) shows the schematic diagram for a dental scaler vibrating at dimensionless immersion depth h/H of 0.5 in holes with the depth H being 10 mm and the volume being 70.7 mm^3. The taper ratio η is 0.35, 1 and 2.75, respectively.

Figure 4.8(b) shows that the time-averaged cavitation density increases with the taper

ratio. The smaller hole opening for the larger taper ratio reduces the wave propagation and associated energy transport outside the hole. The more considerable ultrasonic energy retained in the hole results in stronger pressure waves and, thus, more cavitation in the hole. If a scaler tip has a lid to seal the hole opening, more cavitation will be generated in the hole, enhancing cleaning effects.

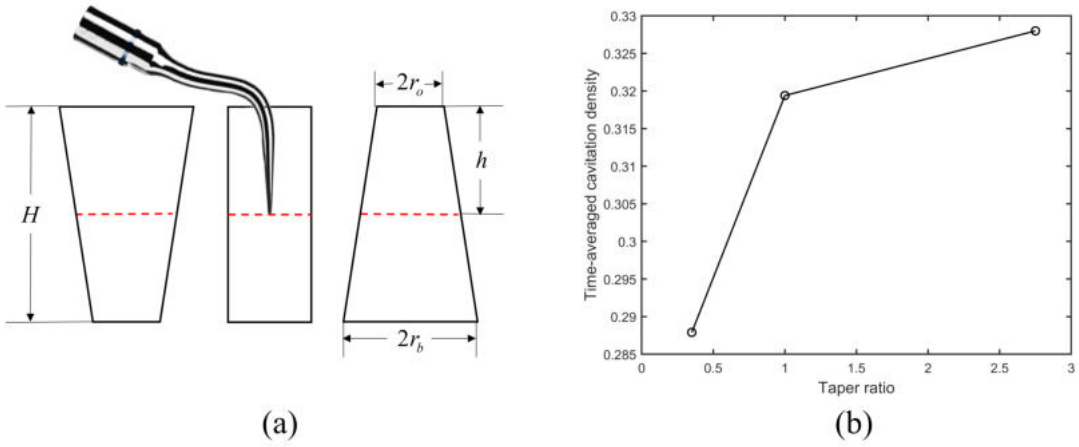

Figure 4.8: (a) Schematic diagram for a dental scaler vibrating in holes with the depth H being 10 mm and the volume being 70.7 mm^3. The taper ratio η is 0.35, 1 and 2.75 (from left to right). (b) Time-averaged cavitation density in the hole versus the taper ratio of the hole. The dimensionless immersion depth of the scaler tip in the hole is 0.5, and other parameters used in the calculations are the same as in figure 4.3.

4.4.4 Effects of the immersion depth

Figure 4.9(a) shows the schematic diagram for a dental scaler vibrating in a hole with the depth of the hole H being 10 mm, the volume being 70.7 mm^3 and the taper ratio being 1 at the dimensionless immersion depth h/H of 0, 0.5 and 0.75, respectively.

Figure 4.9(b) shows that the time-averaged cavitation density increases as the im-

mersion depth of the scaler tip increases. With a larger immersion depth, more energy is introduced into the liquid in the hole, leading to stronger pressure waves in the hole. Consequently, cavitation is more likely to be generated.

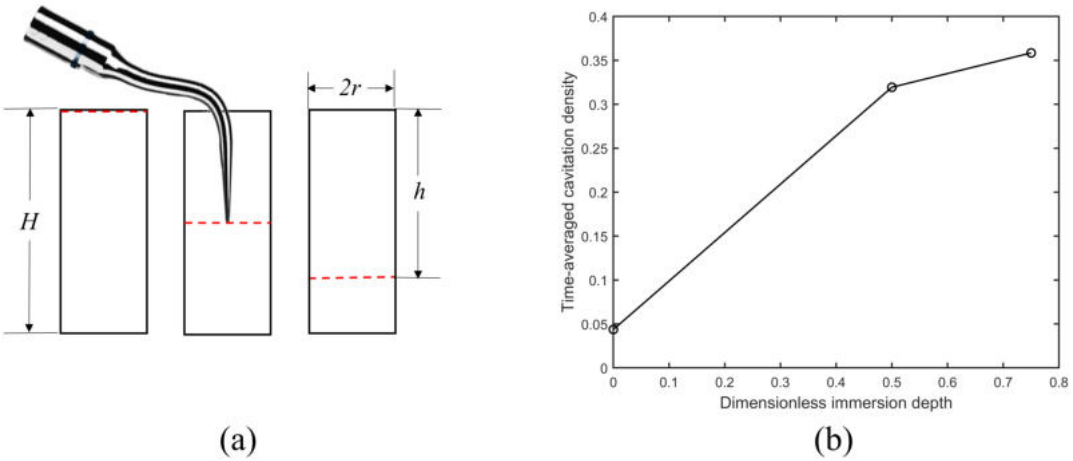

Figure 4.9: (a) Schematic diagram for a dental scaler vibrating in holes with the volume being 70.7 mm^3 and the taper ratio being 1. The dimensionless immersion depths are 0, 0.5, and 0.75 (from left to right). (b) Time-averaged cavitation density in the hole versus the dimensionless immersion depth of the scaler tip. Other parameters used in the calculations are the same as in figure 4.3.

Figure 4.10 shows pressure contours in the three cases with different immersion depths at $t = 399$ μs when the oscillation is relatively stable. Cavitation can be observed in the hole when the immersion depth is 0. This means cleaning effects exist even if the scaler is placed just above the hole. The cavitation density and the cleaning effects increase significantly with the immersion depth.

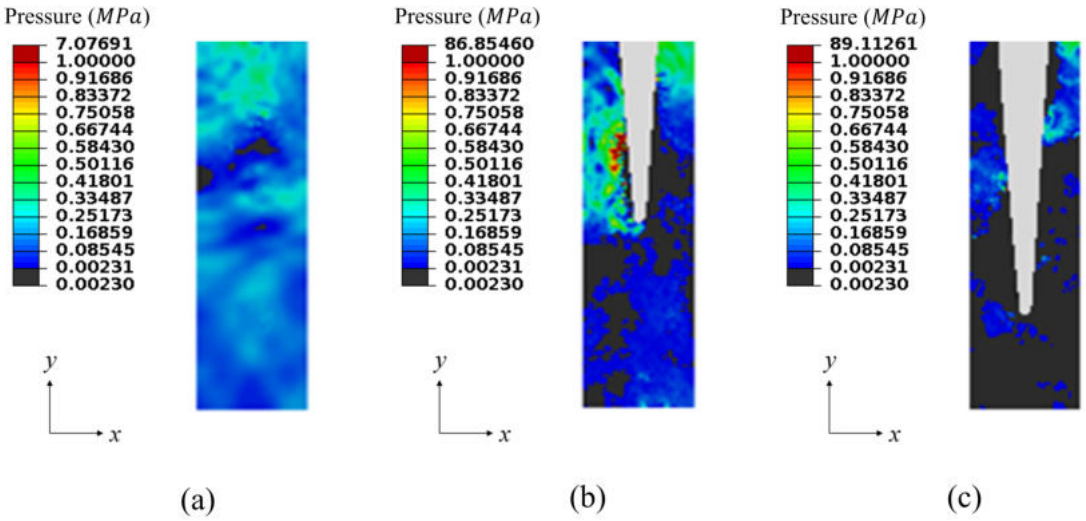

Figure 4.10: Pressure contours at $t = 399$ μs for cases with dimensionless immersion depths being (a) 0, (b) 0.5, and (c) 0.75 on the Oxy-plane of the hole. The black area denotes the area of cavitation. Other parameters used in the calculations are the same as in figure 4.3.

4.5 Chapter summary

A parametric study has been performed to investigate the effects of the volume of the hole, the taper ratio η and the immersion depth of the scaler tip on cavitation generation by an ultrasonic dental scaler vibrating in a periodontal pocket using a coupled acoustic-structural finite element method.

Chapter Five

Numerical investigation of cavitation in periodontal pockets: insights for enhancing cleaning efficiency

This chapter is a reformatted and partially edited version of the article:

Y. Yu, W. R. Smith, Q. Wang, and A. D. Walmsley. "Numerical investigation of cavitation in periodontal pockets: insights for enhancing cleaning efficiency". In: *Ultrasonics Sonochemistry* 100 (2023), p. 106625.

Authorship Statement. **Y. Yu**: Conceptualisation, Methodology, Validation, Formal analysis, Data curation, Investigation, Visualisation, Writing - Original Draft; **W. R. Smith**: Supervision, Writing - Review & Editing; **Q. Wang**: Supervision, Writing - Review & Editing, Funding acquisition; **A. D. Walmsley**: Supervision, Writing - Review & Editing, Funding acquisition.

5.1 Introduction

This chapter extends the research conducted by Manmi et al. [40] and the findings presented in chapter 4. We consider the influence of soft tissue and investigate the effects of the operation conditions and the scaler's cross-sectional shape on cavitation generation to optimise the utilisation and design of ultrasonic scalers.

The physical and numerical model will be described in section 5.2. Validation will be conducted in section 5.3, comparing the numerical results with experimental cavitation images for a scaler vibrating near a wall. Parametric studies investigating the effects of vibration amplitude, frequency, and cross-sectional shapes of the dental scaler on cavitation generation will be presented in section 5.4. Finally, the summary of this chapter is given in section 5.5.

5.2 Physical and numerical model

5.2.1 Problem description

An ultrasonic dental scaler is assumed to undergo vibrations within a water-filled periodontal pocket, as illustrated in figure 5.1(a). A cubic truncated computational domain with dimensions 20 mm $\times$ 30 mm $\times$ 20 mm in the x, y, and z directions is selected, as depicted in figure 5.1(b). The tooth surface is represented as a rigid plane. The periodontal pocket with gum tissue is modelled as a circular cylinder with a radius of 6.5 mm, having a truncated cone removed with the cone radius changing from 5 mm to 2.5 mm and a cone depth of 10 mm, as depicted in figure 5.2. The scaler tip is located 5 mm deep in the pocket and vibrates parallel to the tooth surface plane along the x-axis, maintaining a 1.8 mm distance from the

tooth surface.

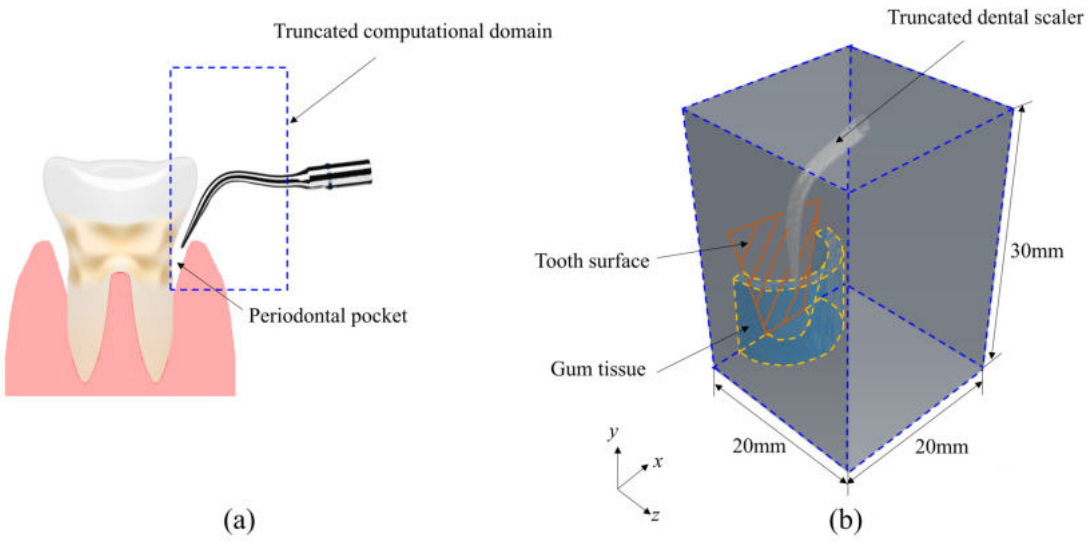

Figure 5.1: (a) Schematic illustration of the ultrasonic dental scaler and the periodontal pocket, and (b) 3D truncated domain in Cartesian coordinates.

Previous studies [40, 41] have shown that the scaler tip displacement remains unaffected by the truncated surface when the truncation is near the circular cylinder base. Consequently, in this study, the scaler is truncated at S_{ts}, as depicted in figure 5.3(a), to reduce the computational domain size and save CPU time. We define a harmonic oscillation at the truncated surface S_{ts} of the scaler with the direction along the axis of symmetry in figure 5.3(a) and the displacement of $A\sin(2\pi ft)$, where A denotes the amplitude and f represents the frequency. As shown in figure 5.3(b), the scaler is denoted as V_{s1} and its surface $S_s = S_{ls} \cup S_{ts}$, where S_{ls} represents the liquid-scaler interface. The gum tissue is V_{s2}, and the liquid-tissue interface is S_{lg}. The truncated liquid domain is represented by V_l, bounded by the scaler surface S_{ls}, the gum tissue surface S_{lg}, the tooth surface S_{rt}, and all the remaining truncated planes S_{tf}.

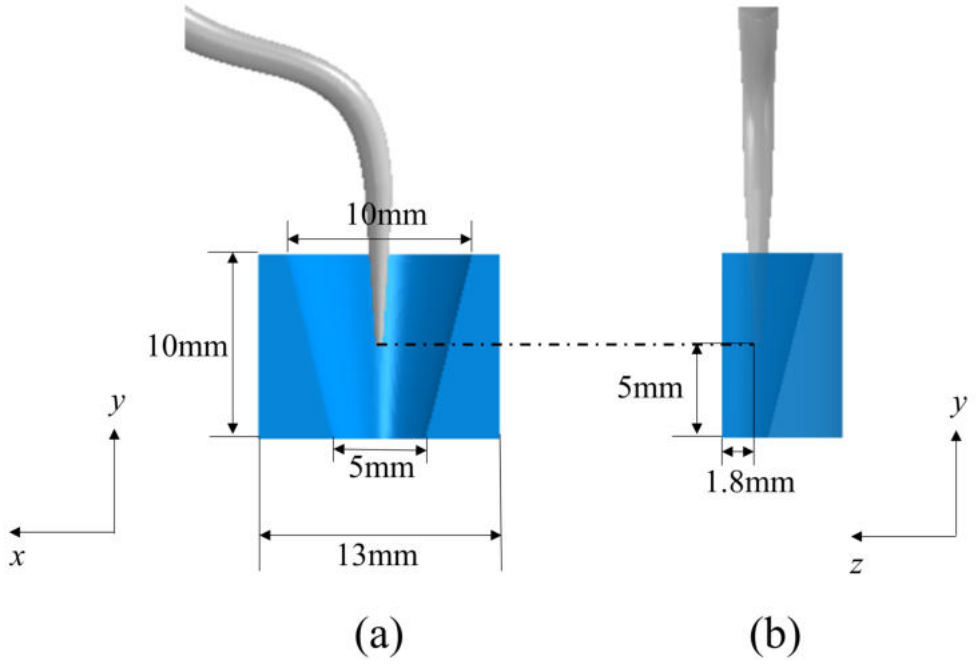

Figure 5.2: The simplified representation of the periodontal pocket with gum tissue and the positions of the scaler in (a) the x-y plane and (b) the y-z plane.

5.2.2 Numerical model

In this work, the structure, including both the scaler and the gum tissue, is governed by the momentum equation [149], with its weak form being

$$\int_{V_s} \rho_s \ddot{\mathbf{u}}_s \delta \mathbf{u}_s dV + \int_{V_s} \sigma_s \cdot (\nabla \cdot \delta \mathbf{u}_s)\, dV + \int_{S_{ls} \cup S_{lg}} p_s \delta \mathbf{u}_s \cdot \mathbf{n}^- dS - \int_{S_{ts}} \delta \mathbf{u}_s \cdot \mathbf{t} dS = 0. \tag{5.1}$$

where the Cauchy stress tensor of the structure σ_s is computed using Hooke's law for the linear elastic material of the scaler and the Ogden model for the hyperelastic material of gum tissue.

The Ogden model [134, 135] has the following the strain energy function

$$U(\lambda_1, \lambda_2, \lambda_3) = \sum_{i=1}^{n} \frac{\mu_i}{\alpha_i} (\lambda_1^{\alpha_i} + \lambda_2^{\alpha_i} + \lambda_3^{\alpha_i} - 3), \tag{5.2}$$

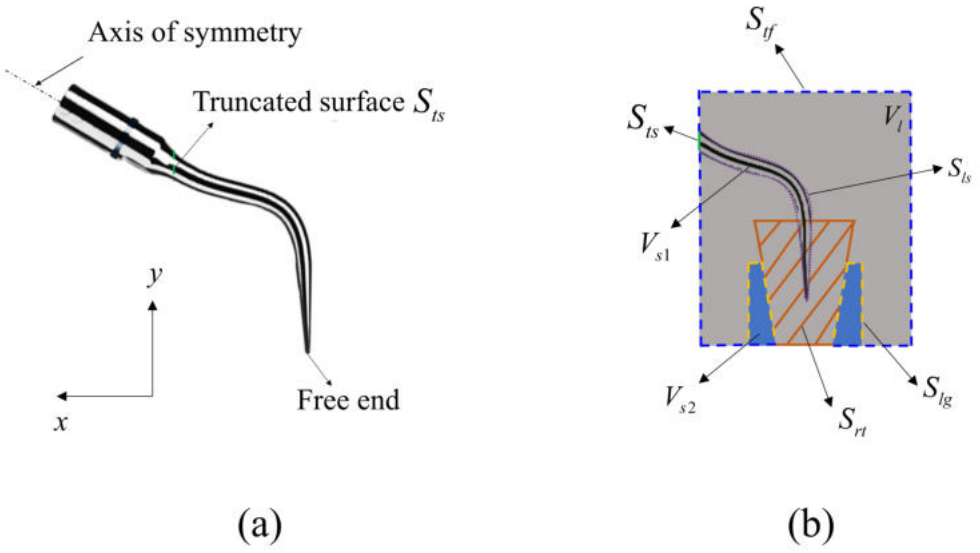

Figure 5.3: (a) The position of the truncated and free end of the scaler tip. (b) Cross-sectional view of the computational domain at the x-y plane indicating the locations of the displacement boundary condition at S_{ts}, the liquid-scaler interface S_{ls}, the liquid-tissue interface S_{lg}, the tooth surface S_{rt} and the truncated surfaces of the computational domain S_{tf}.

where λ_j, $j = 1, 2, 3$, are the principal stretches, μ_i and α_i are material parameters of the Ogden model, which can be determined from material tests, and n is the order of the Ogden model and $n = 3$ is adopted in this chapter. The Cauchy stress σ_s is obtained by differentiating the strain energy density function $U(\lambda)$ with respect to the stretch λ [134, 135].

The equivalent weak form of the momentum equation for finite element analysis of the liquid can be written as

$$\int_{V_f} \left(\frac{1}{K_f} \ddot{p}_f \delta p + \frac{1}{\rho_f} \nabla \delta p \cdot \nabla p_f \right) dV + \int_{S_{rt} \cup S_{ls} \cup S_{lg} \cup S_{tf}} T(\mathbf{x}) \delta p dS = 0. \tag{5.3}$$

where $T(\mathbf{x})$ is the boundary traction, determined by the boundary conditions on surfaces

S_{rt}, S_{ls}, S_{lg} and S_{tf}. For the tooth surface S_{rt}, a rigid immobile wall is applied, while for the truncated surfaces S_{tf} of the liquid domain, a non-reflective boundary condition is implemented to avoid the reflection of pressure waves from the truncated boundaries. The fluid-structure interaction is considered at the interfaces S_{ls} and S_{lg}, which are the liquid-scaler and liquid-tissue interfaces. Further details of the derivation of weak forms (5.1) and (5.3), the model of fluid-structure interaction, and the boundary conditions can be found in chapters 2 and 3.

The one-fluid, cut-off cavitation model, described in chapter 2, is incorporated into the overall model to capture the instantaneous effects of cavitation.

5.3 Numerical validations

5.3.1 Numerical setup

Parameters used for liquid modelling include: the liquid density $\rho_f = 1000$ kg/m^3, the liquid bulk modulus $K_f = 2140$ MPa, and the saturated vapour pressure of the liquid $p_c = 2300$ Pa. The scalers are modelled using the following parameters: the density $\rho_{s1} = 8000$ kg/m^3, Young's modulus $E = 224$ GPa, and Poisson's ratio $\nu = 0.3$ [166]. Polydimethylsiloxane (PDMS) is a hyperelastic material widespread in biomedical research and technology, often employed as a substitute for soft tissue [171]. The density of PDMS is $\rho_{s2} = 980$ kg/m^3 and its hyperelastic properties [172] are represented by the 3^{rd} order Ogden model in our simulations to mimic gum tissue. Strain-stress curves are presented in figure 5.4, and the material parameters for the 3^{rd} order Ogden model are μ_1 = -0.102 MPa, μ_2 = -0.095 MPa, μ_3 = -0.117 MPa, $\alpha_1 = 5.226$, $\alpha_2 = 5.448$, and α_3 = -5.545.

Varying densities are adopted for the discretisation of the computational domain.

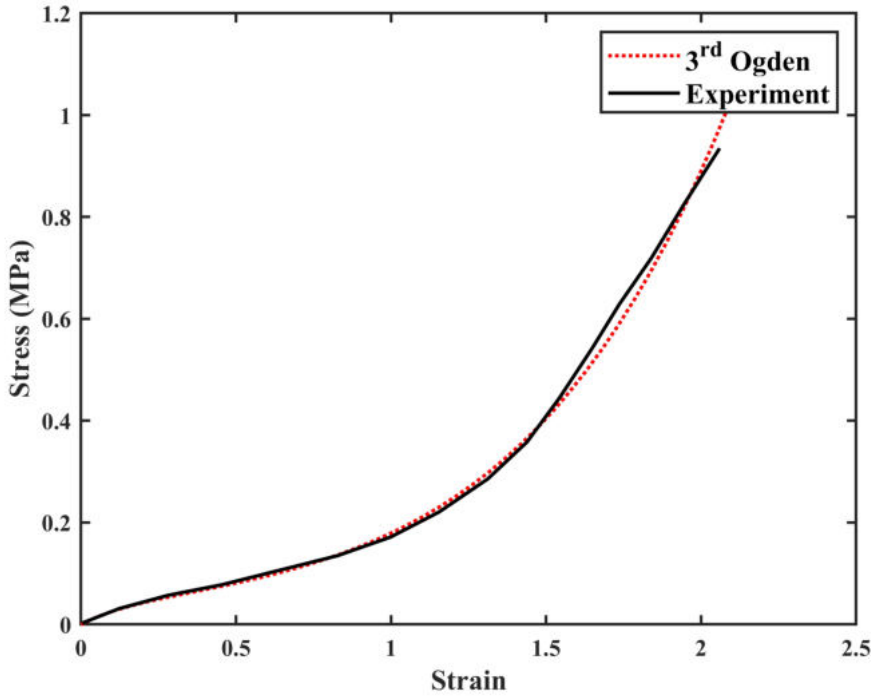

Figure 5.4: Strain-stress curves of PDMS obtained from the experiment [172] and the fitting results using the 3^{rd} Ogden model in the simulations.

The scaler component is modelled using approximately 0.1 million C3D4 solid elements, commonly employed for modelling solid structures. The mesh sizes range from 0.01 mm in proximity to the scaler tip, where larger displacements are anticipated, to 0.06 mm closer to the truncated surface of the scaler. The fluid domain is meshed with acoustic elements (AC3D4), progressively growing from 0.015 mm near the scaler surface to 0.2 mm at the outer boundary of the fluid domain. The gum tissue is meshed with C3D8 solid elements with a uniform size of 0.1 mm. The computational domain contains approximately 8 million elements following the criteria mentioned above.

5.3.2 Mesh convergence test

The convergence test is carried out using varying numbers of elements, including coarse (about 1 million), medium (about 3 million), fine (about 8 million), and very fine (about 12 million). The results in figure 5.5 show cavitation volume history within the periodontal pocket. The truncated surface of the scaler oscillates harmonically at the amplitude $A = 0.01$ mm and the frequency $f = 31$ kHz. Similar results are obtained for the two sets of mesh with higher resolutions. Consequently, the mesh resolution employed for the fine mesh consisting of 8 million elements, as detailed in subsection 5.3.1, is applied to all subsequent simulations.

5.3.3 Comparison with the experiment

To validate the numerical model, we compare the numerical results of the cavitation pattern with the experimental image when an ultrasonic dental scaler undergoes vibrations close to a wall. The experimental image was acquired from an ultrasonic dental scaler that undergoes vibrations in a water tank. More details of the experiment setup can be found in Vyas et al.[37]. As shown in figure 5.6(a), the scaler oscillates parallel to the wall in the experiment, maintaining a 0.5 mm distance from the wall, replicating a clinical setting to avoid potential damage from accidental contact with the wall. In this specific case, the gum tissue V_{s2} in figure 5.3(b) is set as the liquid to simulate the scaler's proximity to a wall.

Previous experiments and simulations were conducted in an unbounded domain, revealing cavitation clouds occurring on both sides of the scaler tip in the direction of displacement [37, 40, 41]. However, cavitation occurs on the side of the tip closest to the wall with the proximity to a wall in both experiments and simulations, as shown in figures 5.6(b) and 5.6(c). The cavitation pattern in the simulation closely matches the experimental results.

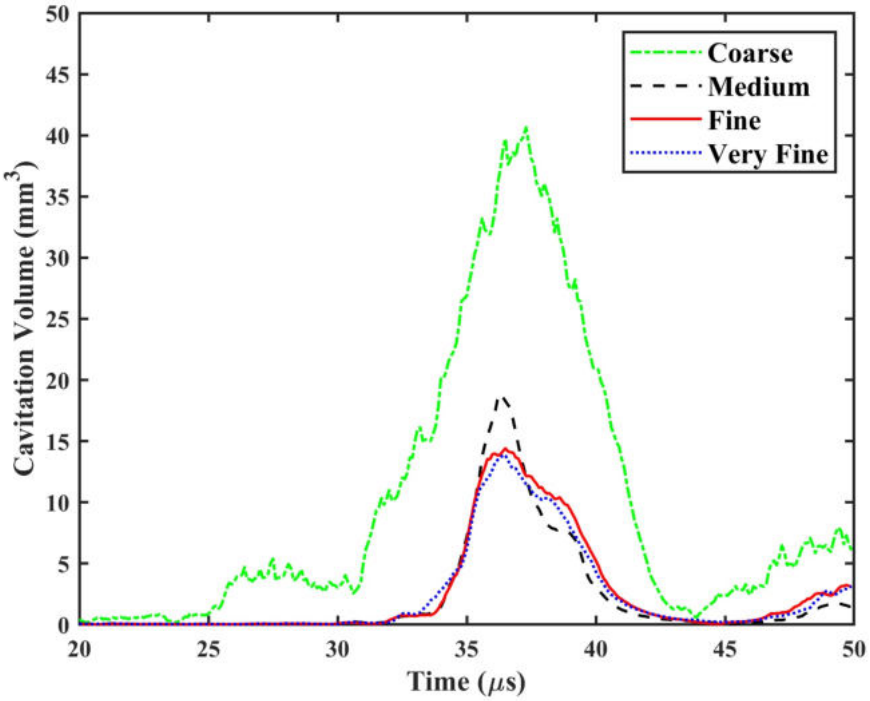

Figure 5.5: Mesh convergence tests for the cavitation volume within the periodontal pocket over time. The element numbers are about 1 million, 3 million, 8 million, and 12 million. The truncated surface of the scaler oscillates harmonically at the amplitude $A = 0.01$ mm and the frequency $f = 31$ kHz. Other parameters for the calculations are $\rho_f = 1000$ kg/m^3, $K_f = 2140$ MPa, $p_c = 2300$ Pa, $\rho_{s1} = 8000$ kg/m^3, $E = 224$ GPa, $\nu = 0.3$, $\rho_{s2} = 980$ kg/m^3, μ_1 = -0.102 MPa, μ_2 = -0.095 MPa, μ_3 = -0.117 MPa, $\alpha_1 = 5.226$, $\alpha_2 = 5.448$, and α_3 = -5.545.

5.4 Numerical results

In clinical settings, ultrasonic dental scalers often operate at frequencies ranging from 20 to 51 kHz, and the amplitude of oscillation can be adjusted by varying the input power of the instrument. We conduct parametric studies to investigate the effects of the oscillation amplitude A and frequency f of the dental scaler on cavitation volume within the periodontal

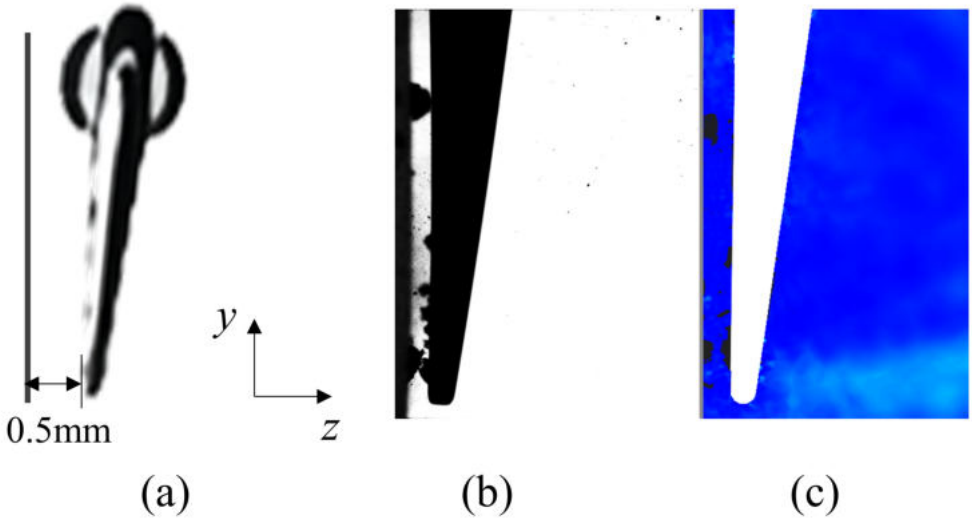

Figure 5.6: (a) Schematic of the scaler near a wall in the experiment, (b) a high-speed experimental cavitation image, and (c) the contour of the liquid pressure. The black region represents cavitation, where the pressure reduces to the cavitation limit of 2300 Pa. Other parameters are the same as in figure 5.5.

pocket. Additionally, we explore the influence of the cross-sectional shape of the scaler tip on cavitation generation. The simulation is conducted for a duration of 500 μs, and the time-averaged void fraction in the periodontal pocket, representing the amount of cavitation generated and indicating the cleaning effects implicitly, is evaluated.

5.4.1 Effects of the vibration amplitude

To analyse the impact of the scaler's oscillation amplitude A on cavitation generation, we simulate the dental scaler oscillating in the periodontal pocket with both soft and nearly rigid (by setting the gum tissue with the same material as the scaler) boundaries at various amplitudes A ranging from 0.005 to 0.02 mm and a frequency f of 31 kHz.

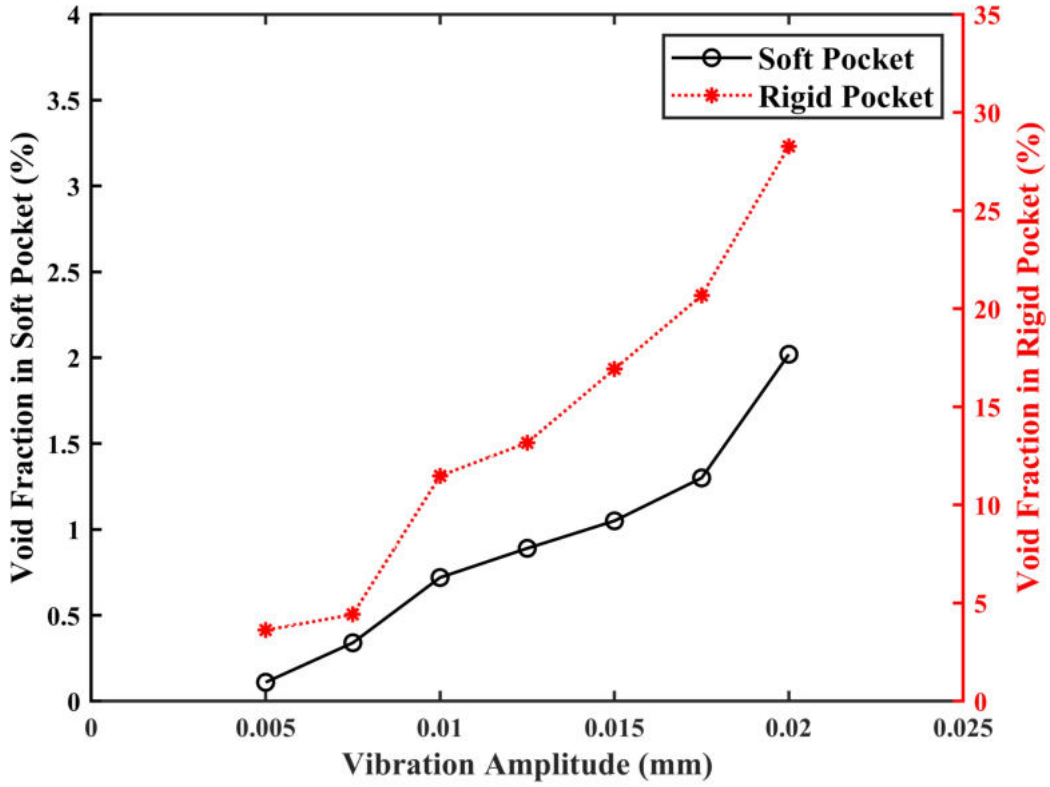

Figure 5.7: Void fraction in the periodontal pocket with both soft and nearly rigid boundaries plotted against the scaler tip's oscillation amplitude A. The oscillation amplitude A ranges from 0.005 to 0.02 mm, and other parameters are the same as in 5.5.

Figure 5.7 illustrates that the void fraction increases with the vibration amplitude for both soft and nearly rigid boundaries. The energy density of a linear plane harmonic acoustic wave can be estimated as

$$I = \frac{1}{2}\rho_f c(2\pi f_p)^2 A_p^2, \tag{5.4}$$

where f_p and A_p are the oscillation frequency and amplitude of the liquid particle. At the same oscillation frequency, the energy transferred to the liquid increases significantly with the amplitude, leading to more cavitation.

Figure 5.7 also demonstrates that less cavitation is generated when the pocket bound-

ary is soft. This is because a substantial part of ultrasonic energy propagated into the liquid has been absorbed by the soft boundary and transformed into elastic wave energy rather than being reflected at the rigid boundary.

5.4.2 Effects of the vibration frequency

To analyse the impact of the scaler's frequency on cavitation generation, we simulate the dental scaler oscillating in the periodontal pocket with both soft and nearly rigid boundaries at various frequencies f ranging from 20 to 45 kHz, with an amplitude A of 0.01 mm.

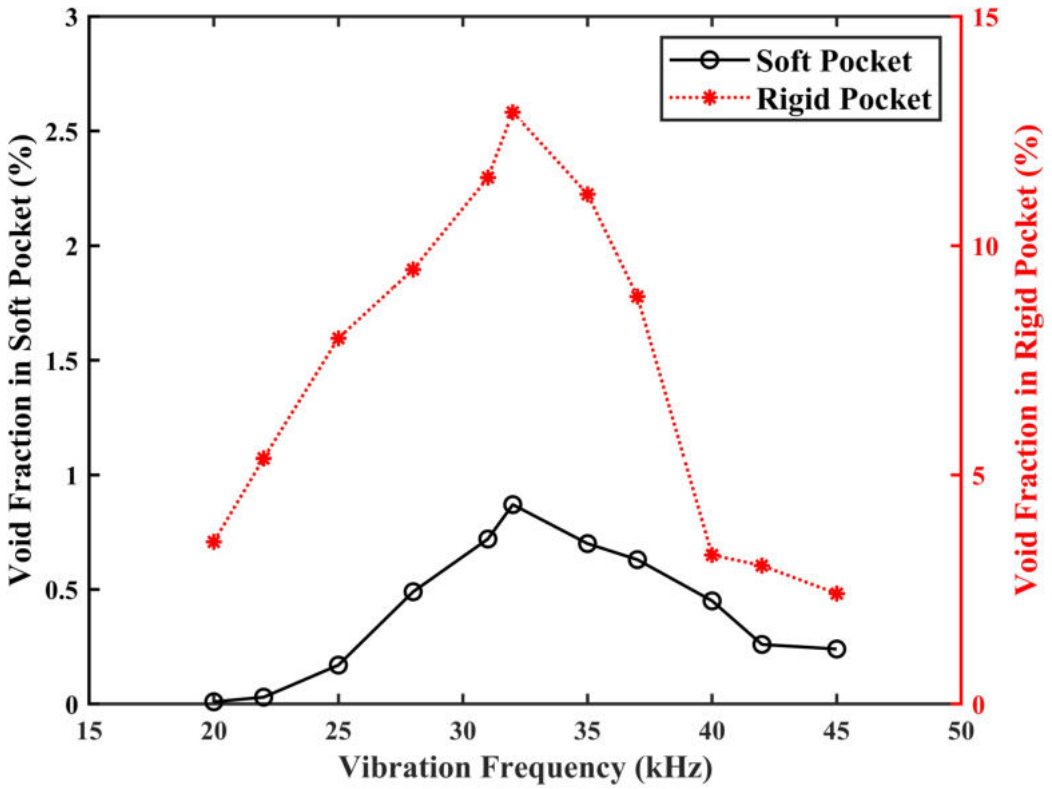

Figure 5.8: Void fraction in the periodontal pocket with both soft and nearly rigid boundaries plotted against the scaler's vibration frequency f. The vibration frequency f ranges from 20 to 45 kHz, and other parameters are the same as in figure 5.5.

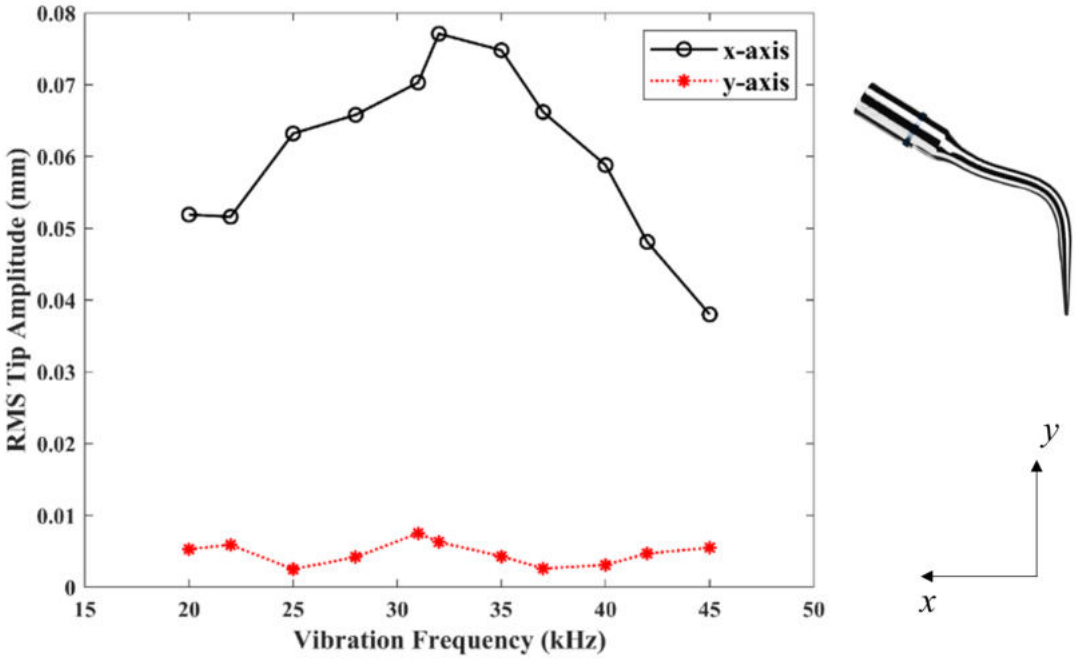

Figure 5.9: The root mean square (RMS) amplitude of the scaler tip along the x- and y-axes plotted against the vibration frequency f of the scaler tip. The vibration frequency f ranges from 20 to 45 kHz, and other parameters are the same as in figure 5.5.

As shown in figure 5.8, the void fraction within the periodontal pocket increases with the vibration frequency, attaining its peak value at approximately 32 kHz before gradually decreasing. Figure 5.9 displays the root mean square (RMS) amplitude of the scaler tip along the x- and y- axes, which is evaluated by

$$A_{RMS} = \sqrt{\frac{1}{N}\sum_{i=1}^{N} A_i^2}, \tag{5.5}$$

where A_{RMS} represents the RMS amplitude, A_i denotes the i^{th} simulated amplitude, and N is the total number of samples. The amplitude along the x-axis follows the same trend as the void fraction and is significantly larger than that along the y-axis. To analyse this pattern, the natural frequency of the scaler undergoing vibrations without the presence of surrounding liquid is evaluated using ABAQUS, which is 34.7 kHz. The natural frequency

of the scaler's vibrations in the liquid should decrease due to the effect of the added mass to the system by the liquid. Therefore, the peak value of the void fraction and scaler tip amplitude at 32 kHz in figures 5.8 and 5.9 correspond to the resonance of the system subject to the oscillation of the scaler.

5.4.3 Effects of the shape of the scaler tip cross-section

We now analyse the impact of the cross-sectional shape of the scaler tip on cavitation generation. Three cross-sectional shapes are considered, as shown in figure 5.10: Type A: a thin cross-section to the direction of the displacement of the scaler tip; Type B: a circular cross-section; and Type C: a blunt cross-section. These three cross-sectional shapes are kept in the same area. The amplitude A and the frequency f are 0.01 mm and 31 kHz, respectively.

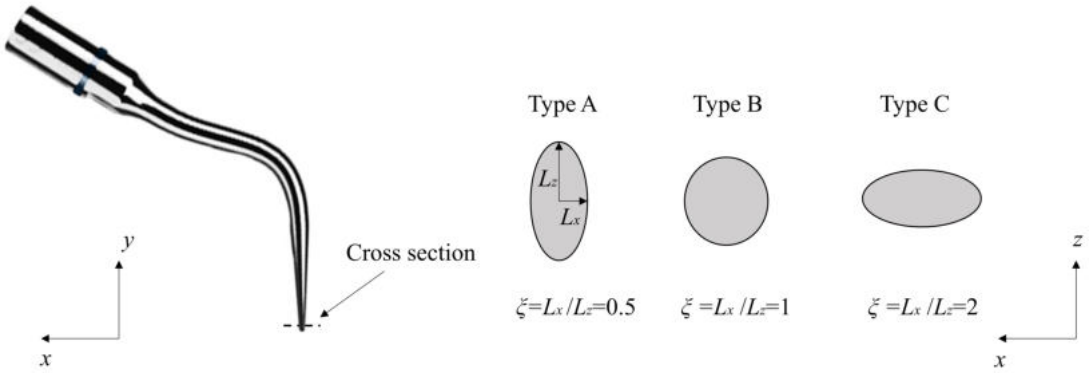

Figure 5.10: Schematics showing various cross-sectional shapes of dental scalers, where the x-axis is along the scaler tip displacement direction. Type A: a thin cross-section ($\xi = 0.5$), Type B: a circular cross-section ($\xi = 1$), and Type C: a blunt cross-section ($\xi = 2$).

Figure 5.11 illustrates that the void fraction in the periodontal pocket increases as the ratio $\xi = L_x/L_z$ decreases. Figure 5.12 displays the RMS amplitude of the scaler tip along the x- and y- axes, which follow the same trend as the void fraction. The moment of

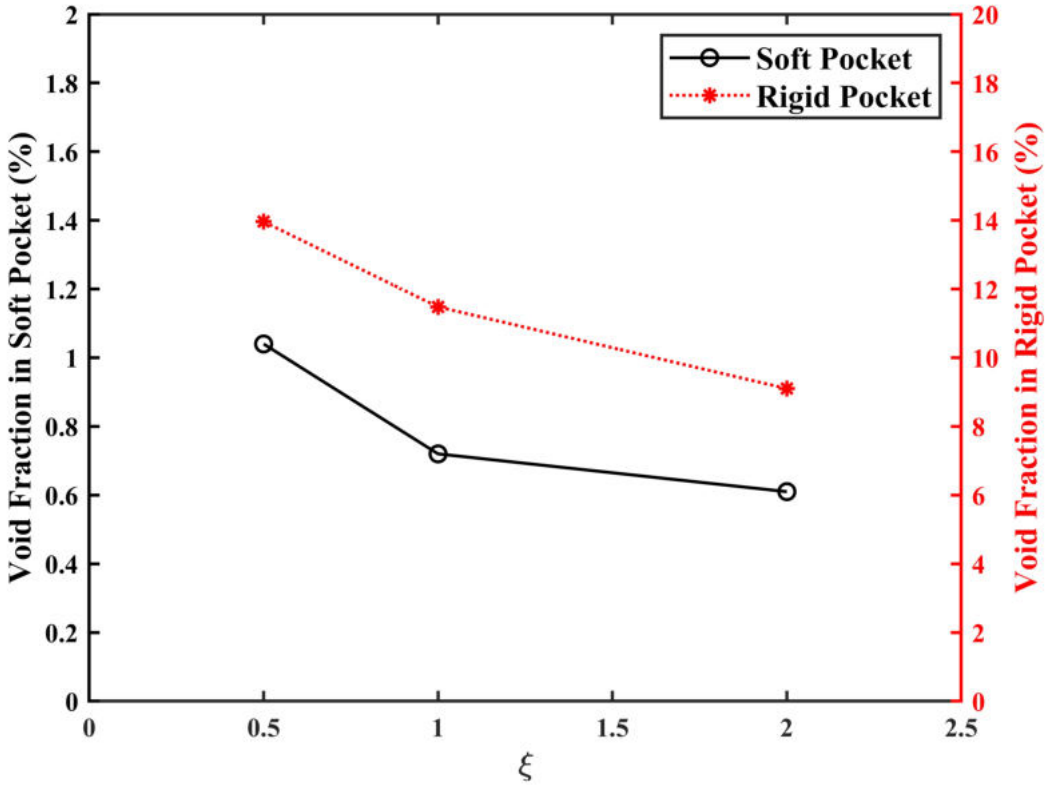

Figure 5.11: Void fraction in the periodontal pocket with both soft and nearly rigid boundaries, generated by dental scalers with different cross-sectional shapes (Type A: a thin cross-section $\xi = 0.5$, Type B: a circular cross-section $\xi = 0.5$, and Type C: a blunt cross-section $\xi = 0.5$). Parameters are the same as in figure 5.5.

inertia of area (also known as the second moment of area) for the cross-section of the scaler tip can be calculated by [173]

$$I_{zz} = \frac{\pi L_x^3 L_z}{4}. \tag{5.6}$$

Following equation (5.6), the moments of inertia of area for Type A, Type B, and Type C are $I_{Azz} = \frac{\pi R^4}{8}$, $I_{Bzz} = \frac{\pi R^4}{4}$, and $I_{Czz} = \frac{\pi R^4}{2}$, respectively, where R is the radius of the cross-section of Type B. According to the Euler–Bernoulli bending theory [174], the deflection w

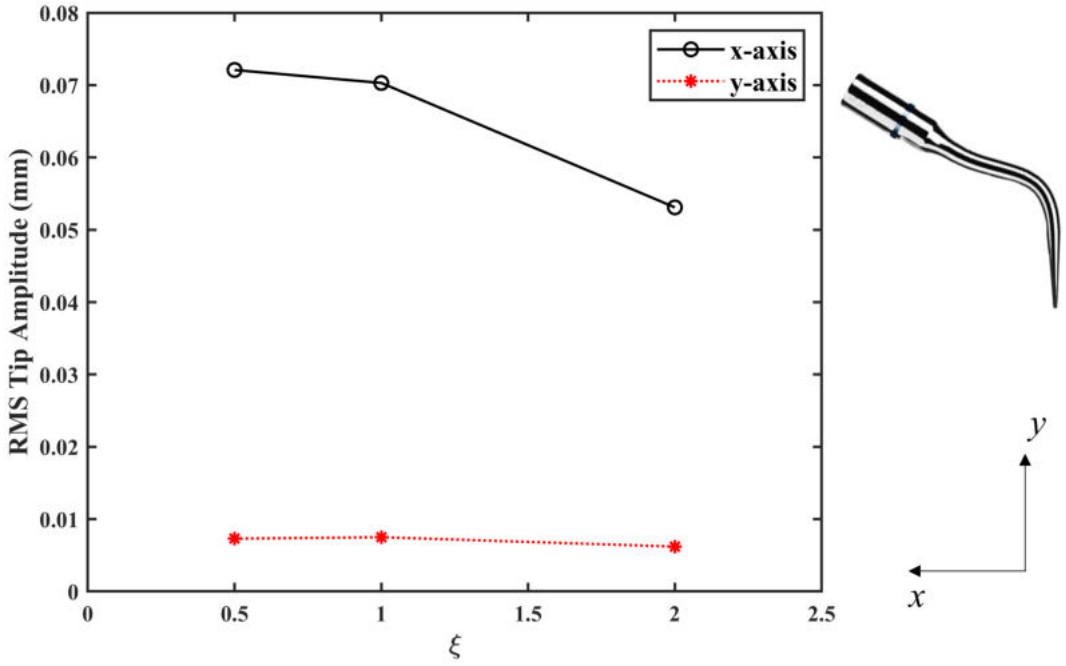

Figure 5.12: The RMS amplitude of the scaler tip along the x- and y- axes for dental scalers with different cross-sectional shapes (Type A: a thin cross-section $\xi = 0.5$, Type B: a circular cross-section $\xi = 1$, and Type C: a blunt cross-section $\xi = 2$). Other parameters are the same as in figure 5.5.

of a slender beam can be described by

$$\frac{\partial^2 w}{\partial y^2} = \frac{M}{EI}, \tag{5.7}$$

where M is the applied bending moment at a given position, E is the Young's modulus of the material, and y is the position along the beam. The deflection of a bending beam is inversely proportional to the moment of inertia of the area of the beam's cross-section. Therefore, with the same input power for the scaler, the scaler tip vibrates at a larger amplitude as the thickness along the main direction of oscillation (x-axis) decreases, increasing cavitation generation.

Manufacturers have designed different shaped tips for various cleaning applications

inside the mouth. For instance, broader and larger tips are used to clean mineralised plaque deposits above the gum line, while much thinner tips are used for subgingival cleaning. To enhance the effective use of ultrasonic scalers in a non-touch mode, modifying the shape of the scaler tip to decrease the moment of inertia of area for the cross-section and increase the tip oscillation amplitude, resulting in more cavitation generation, can be beneficial.

5.5 Chapter summary

Considering the impact of soft tissue of the periodontal pocket, we have conducted a parametric study numerically to explore the effects of vibration amplitude, frequency, and the cross-sectional shape of the dental scaler on cavitation generation. The clinical relevance of these findings is that when dealing with a periodontal pocket with severe inflammation, clinical operators are advised to adjust the frequency of the scaler to match its natural frequency and increase the amplitude to maximise cavitation and cleaning effects.

Chapter Six

Summary, conclusions and possible developments

6.1 Summary and conclusions

This thesis explores the dynamics of a single bubble in a viscous compressible liquid near a rigid boundary at a moderately large Reynolds number of O(10-100) and the application of cavitation bubbles in dental cleaning.

(1) Chapter 3. The mechanisms of jetting, vortex sheet and vortex ring development in asymmetric bubble dynamics

The bubble dynamics near a rigid boundary for Reynolds number O(10-100) is studied experimentally and numerically. New dynamic features are revealed.

(i) Mechanisms underlying the bubble jetting and vortex ring

During expansion, the distal part of the bubble surface from the wall expands faster than the closer part, as the latter is hindered by the wall. Accordingly, the bubble gas on

the distal side flows faster away from the stagnation point, initially at the bubble centre, and has smaller pressure according to the Bernoulli equation. As a result, the stagnation point moves away from the wall during expansion, and a vortex sheet forms inside the bubble as the streamlines converge to the stagnation point with different velocities.

As the vortex sheet approaches the bubble interface, it transfers momentum to the gas-liquid interface, influencing the liquid flow close to the bubble wall. At approximately the maximum bubble volume, the stagnation point moves out of the bubble. The high-pressure zone at the stagnation point drives the distal bubble surface to collapse first and fastest, pulling the side liquid inwards. In the meantime, the part of the bubble surface nearest the wall still expands, pushing the liquid between the bubble and the rigid boundary outwards. This generates a circulation around the side cross-section of the bubble. A vortex ring is accordingly generated within the bubble gas at the outer rim of the vortex sheet as the vortex sheet decays, owing to the higher shear stress from the liquid.

The distal bubble surface collapses faster during the collapse, the liquid flow towards the distal part strengthens, and the vortex ring intensifies. These events enhance each other in a positive feedback loop. A high-speed liquid jet develops at the distal bubble surface, accelerated by the vortex ring. The liquid jet subsequently penetrates the bubble and is redirected outwards after impacting the wall. This, in turn, strengthens the circulation around the vortex ring.

With the core of the vortex ring inside the bubble gas, much less energy loss occurs than inside the liquid. This is because the energy dissipation of a vortex ring is proportional to viscosity, and most energy dissipation occurs near its centre. With its core inside the bubble gas, the vortex ring accelerates the jet like a bearing system. These new insights into the gas flow inside the bubble provide supporting evidence for the nanodroplet injection model.

(ii) Viscous effects

The jet is shallower due to viscosity effects and has less kinetic energy at a smaller Reynolds number. With less kinetic energy associated with the jet, the bubble collapses violently to a smaller minimum value, producing stronger shockwaves. With significantly more energy radiated due to the stronger shockwaves, the subsequent oscillation during the second cycle has a smaller maximum radius. The period of oscillation is energy dependent; therefore, the period also reduces due to the energy reduction.

The pressure on the wall is more significant due to the stronger shockwave emission at the end of the first cycle when the Reynolds number is smaller. As more energy is radiated due to stronger shockwaves at the end of the first cycle, the shockwaves are much weaker, and the pressure on the rigid boundary is much smaller at the end of the second cycle.

An oscillating bubble in a higher viscous liquid is more stable. A bubble often breaks up after the first cycle of oscillation in water. A bubble often remains stable in higher viscosity liquid after multiple oscillation cycles.

For a bubble in inertial collapse near a rigid boundary, the significant shear stress at the boundary occurs primarily as the shockwaves propagate and the jet spreads along the boundary. The former has a much higher amplitude, and the latter has a longer period. They both increase with decreasing Reynolds number.

(2) Chapter 4. Cavitation in a periodontal pocket by an ultrasonic dental scaler: a numerical investigation

A parametric study for an ultrasonic dental scaler oscillating in a periodontal pocket has been performed to investigate the effects of the volume of the periodontal pocket, the taper ratio η and the immersion depth of the scaler tip on the cavitation generated. Based on the numerical results, it can be concluded that:

More cavitation around a scaler tip is generated when it is vibrating in a hole, and the cavitation density increases as the hole volume decreases. This is because the ultrasound energy per unit volume increases inversely with the hole volume.

The cavitation density increases with the taper ratio as more energy remains in the hole due to the increased blocking effect. The cleaning effects should be improved by adding a lid to the scaler tip to cover the hole opening.

Cavitation forms in the hole even if the scaler is placed above the hole. The cavitation density increases significantly with the immersion depth of the scale tip in the hole.

The cavitation density varies when the scaler tip is put in periodontal pockets with various shapes and immersion depths. The increase in cavitation density may result in increased cleaning efficiency. In this regard, the numerical model developed in this study can aid in further optimisation studies that allow the ultrasonic scaler to be used in a non-touching technique more efficiently.

(3) Chapter 5. Numerical investigation of cavitation in periodontal pockets: insights for enhancing cleaning efficiency

A parametric study has been undertaken to explore the impacts of vibration amplitude, frequency, and the cross-sectional shape of the dental scaler on cavitation generation. The following new features/phenomena are observed.

Cavitation generated in the periodontal pocket with a soft boundary is significantly less than that with a nearly rigid boundary. This is because a significant part of the acoustic energy is transformed into the elastic wave energy of the soft boundary.

Increasing the scaler's oscillation amplitude at a fixed oscillation frequency leads to higher cavitation levels as more ultrasonic energy is introduced into the liquid.

Cavitation within the periodontal pocket reaches the peak value when the vibration frequency is 32 kHz for the dental scaler tip 10P. This frequency closely matches the natural frequency of the scaler, and the peak cavitation coincides with the maximum amplitude of the scaler tip. This phenomenon is attributed to the resonance of the system.

The scaler tip's cross-sectional shape significantly influences the scaler tip's oscillation amplitude and the cavitation generation within the periodontal pocket. When the cross-sectional area is constant, an increase in the scaler tip's amplitude and cavitation generation can be achieved by reducing the thickness of the scaler tip along its main oscillation direction. This finding can potentially optimise the structural design of dental scalers for better cleaning effects.

6.2 Possible developments

Regarding the study of single bubble dynamics, a numerical model with a newly proposed non-reflective boundary condition has been established with the volume of fluid interface capturing method. However, non-conservation of mass is observed at the end of collapse, which could be attributed to the precision of the interface capturing method needs to be improved. A high-precision interface capturing method, such as a cut-cell method based on the Eulerian-Lagrangian method, can be developed.

Regarding the study of ultrasonic cavitation in dental cleaning, the cleaning effects are investigated implicitly by evaluating the amount of cavitation generated. This evaluation approach can be further improved if dental plaque biofilms can be modelled. Moreover, a more accurate model for cavitation bubble clusters will enhance the reliability of the cavitation predicted by numerical simulations.

Appendix One

Derivation of Rayleigh-Plesset equation for a spherical bubble

Spherical bubble oscillation in an incompressible liquid is mathematically described by the Rayleigh–Plesset equation [43]. Derivation of the equations is described herein.

Consider a spherical bubble in an infinite incompressible liquid. Set spherical coordinates (r, ϕ, θ) with the origin at the bubble centre. Every function then depends on only one spatial variable, r, the distance from the bubble centre to the point considered, and time t. As such, the velocity $\mathbf{u}$ in the liquid satisfies

$$\mathbf{u} = u(r,t)\,\mathbf{e}_r, \tag{A.1}$$

where $\mathbf{e}_r$ is the unit coordinate vector for the r-coordinate. Namely, $u_r = u(r,t), u_\phi = u_\theta = 0$.

The unknown functions in the problem to be determined are: (1) The bubble radius history $R(t)$ in terms of time t; (2) In the liquid domain $r \geq R(t)$, the velocity $u(r,t)$ and the pressure $p(r,t)$ induced by the evolution of the bubble.

Assuming the liquid is incompressible, the continuity equation of the liquid flow reads

$$\nabla \cdot \mathbf{u} = 0. \tag{A.2}$$

The divergence of $\mathbf{u}$ in spherical coordinates is

$$\nabla \cdot \mathbf{u} = \frac{1}{r^2}\frac{\partial\left(r^2 u_r\right)}{\partial r} + \frac{1}{r\sin\theta}\frac{\partial\left(\sin\theta u_\theta\right)}{\partial\theta} + \frac{1}{r\sin\theta}\frac{\partial\left(u_\phi\right)}{\partial\phi}. \tag{A.3}$$

Using the symmetry of the modelling, i.e. $\mathbf{u} = \left(u\left(r,t\right),0,0\right)$, we have

$$\nabla \cdot \mathbf{u} = \frac{1}{r^2}\frac{\partial\left(r^2 u\right)}{\partial r} = 0. \tag{A.4}$$

This yields

$$r^2 u\left(r,t\right) = c'(t), \tag{A.5}$$

for $r \geq R(t)$, where $c'(t)$ is a function depending only on time.

When mass transfer through the interface is neglected, the liquid velocity at the interface $u\left(R,t\right)$ is equal to the interface velocity. Thus, we have

$$r^2 u\left(r,t\right) = c'(t) = R^2 u\left(R\left(t\right),t\right) = R^2(t)\dot{R}(t), \tag{A.6}$$

Namely

$$u\left(r,t\right) = \frac{c'(t)}{r^2} = \frac{R^2(t)\dot{R}(t)}{r^2}. \tag{A.7}$$

The velocity of the liquid flow at a point due to an oscillating spherical bubble is inversely proportional to the square of the distance r from the point considered to the bubble centre.

The Navier-Stokes equations for an incompressible liquid flow read

$$\rho\left(\frac{\partial\mathbf{u}}{\partial t} + \mathbf{u}\cdot\nabla\mathbf{u}\right) = \rho\mathbf{f} - \nabla p + \mu\nabla^2\mathbf{u}. \tag{A.8}$$

Here, $\mathbf{f}$ is the body force, ρ and μ are the density and dynamic viscosity of the liquid.

Its r-component in spherical coordinates is given by

$$\rho\left(\frac{du_r}{dt}-\frac{u_\theta^2+u_\phi^2}{r}\right)=-\frac{\partial p}{\partial r}+\rho f_r+\mu\left(\nabla^2 u_r-\frac{2u_r}{r^2}-\frac{2}{r^2}\frac{\partial u_\theta}{\partial\theta}-\frac{2u_\theta\cot\theta}{r^2}-\frac{2}{r^2\sin\theta}\frac{\partial u_\phi}{\partial\phi}\right), \tag{A.9}$$

where $\frac{d}{dt}=\frac{\partial}{\partial t}+u_r\frac{\partial}{\partial r}+\frac{u_\theta}{r}\frac{\partial}{\partial\theta}+\frac{u_\phi}{r\sin\theta}\frac{\partial}{\partial\phi}$, $\nabla^2=\frac{1}{r^2}\frac{\partial}{\partial r}\left(r^2\frac{\partial}{\partial r}\right)+\frac{1}{r^2\sin^2\phi}\frac{\partial^2}{\partial\theta^2}+\frac{1}{r^2\sin\phi}\frac{\partial}{\partial\phi}\left(\sin\phi\frac{\partial}{\partial\phi}\right)$.

Using $u_r=u\left(r,t\right),u_\phi=u_\theta=0$, we have

$$\rho\left(\frac{\partial u}{\partial t}+u\frac{\partial u}{\partial r}\right)=-\frac{\partial p}{\partial r}+\mu\left(\frac{1}{r^2}\frac{\partial}{\partial r}\left(r^2\frac{\partial u}{\partial r}\right)-\frac{2u}{r^2}\right), \tag{A.10}$$

or

$$\frac{\partial u}{\partial t}+u\frac{\partial u}{\partial r}=-\frac{1}{\rho}\frac{\partial p}{\partial r}+\nu\left(\frac{1}{r^2}\frac{\partial}{\partial r}\left(r^2\frac{\partial u}{\partial r}\right)-\frac{2u}{r^2}\right),\nu=\frac{\mu}{\rho}. \tag{A.11}$$

Substituting $u\left(r,t\right)=\frac{c'(t)}{r^2}$ yields

$$\frac{\partial}{\partial t}\frac{c'\left(t\right)}{r^2}+\frac{c'\left(t\right)}{r^2}\frac{\partial}{\partial r}\left(\frac{c'\left(t\right)}{r^2}\right)=-\frac{1}{\rho}\frac{\partial p}{\partial r}+\nu\left(\frac{1}{r^2}\frac{\partial}{\partial r}\left(r^2\frac{\partial}{\partial r}\left(\frac{c'\left(t\right)}{r^2}\right)\right)-\frac{2c'\left(t\right)}{r^4}\right). \tag{A.12}$$

Thus, we have

$$\frac{\dot{c}'}{r^2}-2\frac{c'^2}{r^5}=-\frac{1}{\rho}\frac{\partial p}{\partial r}. \tag{A.13}$$

In this very particular case, the viscous term of the Navier-Stokes equations cancelled automatically. Thus, for both a viscous and non-viscous fluid, the momentum equation remains the same.

Integrating the above equation (A.13) with respect to r from $r=R\left(t\right)$ to $r\to\infty$ yields

$$\int_{R(t)}^{\infty}\left(\frac{\dot{c}'}{r^2}-2\frac{c'^2}{r^5}\right)dr=-\int_{R(t)}^{\infty}\frac{1}{\rho}\frac{\partial p}{\partial r}dr. \tag{A.14}$$

Noticing the density is a constant for an incompressible flow, we have

$$\frac{\dot{c}'}{R}-\frac{1}{2}\frac{c'^2}{R^4}=\frac{p_B\left(t\right)-p_{amb}}{\rho},p_B\left(t\right)=p\left(R\left(t\right),t\right),p_{amb}=p|_{r\to\infty}. \tag{A.15}$$

Here, $p_B(t)$ is the transient liquid pressure at time t at the bubble surface $r = R(t)$, and p_{amb} is the ambient pressure.

Substituting $c'(t) = R^2(t)\dot{R}(t)$ into the above equation yields

$$\rho\left(R\ddot{R} + \frac{3}{2}\dot{R}^2\right) = p_B(t) - p_{amb}. \tag{A.16}$$

As the liquid is quiescent, the ambient pressure p_{amb} is the hydrostatic pressure p_∞. Considering the surface tension and viscous effects, the transient liquid pressure at the bubble surface can be calculated by

$$p_B = p_v + p_{b0}\left(\frac{R_0}{R}\right)^{3\gamma_h} - 4\mu\frac{\dot{R}}{R} - \frac{2\sigma}{R}, \tag{A.17}$$

where p_v is the vapour pressure, p_{b0} is the initial bubble gas pressure, R_0 and R are the initial and transient bubble radii, γ_h is the ratio of the specific heats of the gas, and σ is the surface tension coefficient.

Substituting equation (A.17) into equation (A.16) yields

$$\rho\left(R\ddot{R} + \frac{3}{2}\dot{R}^2\right) = p_v + p_{g0}\left(\frac{R_0}{R}\right)^{3\gamma_h} - p_{amb} - \frac{2\sigma}{R} - 4\mu\frac{\dot{R}}{R}. \tag{A.18}$$

This equation, known as the Rayleigh-Plesset equation, allows us to determine the temporal evolution of the bubble radius $R(t)$ and consequently the pressure field in the liquid, when the ambient pressure p_{amb} and the initial conditions are given.

Appendix Two

Derivation of Keller-Miksis equation for a spherical bubble

The Rayleigh–Plesset equation describes the spherical bubble oscillation in an incompressible liquid. When considering the weak compressibility of the liquid with low Mach number, the spherical bubble oscillation can be described by the Keller-Miksis equation [47]. Derivation of the equations is described herein.

A compressible inviscid flow is governed by the equation of mass conservation

$$\frac{\partial \rho}{\partial t} + \nabla \cdot (\rho \mathbf{u}) = 0, \tag{B.1}$$

and the equation for momentum conservation in the absence of body forces

$$\frac{\partial \mathbf{u}}{\partial t} + \mathbf{u} \cdot \nabla \mathbf{u} = -\frac{1}{\rho} \nabla p. \tag{B.2}$$

By assuming the flow is irrotational, we may introduce a velocity potential φ such that $\mathbf{u} = \nabla \varphi$. With this definition equation (B.1) is rewritten as

$$\nabla^2 \varphi + \frac{1}{\rho} \left(\frac{\partial \rho}{\partial t} + \nabla \varphi \cdot \nabla \rho \right) = 0. \tag{B.3}$$

Noticing $\mathbf{u}\cdot\nabla\mathbf{u} = \nabla\frac{u^2}{2} - \mathbf{u}\times\nabla\times\mathbf{u} = \nabla\frac{u^2}{2} - \mathbf{u}\times\nabla\times\nabla\varphi$, equation (B.2) becomes

$$\frac{\partial}{\partial t}\nabla\varphi + \nabla\frac{u^2}{2} = -\frac{1}{\rho}\nabla p. \tag{B.4}$$

As $p = p(\rho)$, equation (B.4) can be expressed as

$$\frac{\partial}{\partial t}\nabla\varphi + \nabla\frac{u^2}{2} = -c^2\frac{\nabla\rho}{\rho}, \tag{B.5}$$

where $c = \sqrt{\frac{dp}{d\rho}}$, which is the speed of sound.

Equation (B.6) is integrated once to give the Bernoulli equation, assuming here c is a constant,

$$\frac{\partial\varphi}{\partial t} + \frac{u^2}{2} + c^2\ln\rho = c^2\ln\rho_\infty. \tag{B.6}$$

where ρ_∞ is the undisturbed density at the far field.

Taking the derivative of equation (B.6) with respect to time gives us

$$\frac{\partial^2\varphi}{\partial t^2} + \frac{\partial}{\partial t}\left(\frac{u^2}{2}\right) + c^2\frac{1}{\rho}\frac{\partial\rho}{\partial t} = 0. \tag{B.7}$$

Subtracting equation (B.3) by equation (B.7) divided by c^2 yields

$$\nabla^2\varphi - \frac{1}{c^2}\frac{\partial^2\varphi}{\partial t^2} = \frac{1}{2c^2}\frac{\partial u^2}{\partial t} - \nabla\varphi\cdot\frac{\nabla\rho}{\rho}. \tag{B.8}$$

Using equation (B.5), equation (B.8) can be written as

$$\begin{aligned}
&\nabla^2\varphi - \tfrac{1}{c^2}\tfrac{\partial^2\varphi}{\partial t^2} = \tfrac{1}{2c^2}\tfrac{\partial u^2}{\partial t} - \nabla\phi\cdot\tfrac{\nabla\rho}{\rho}\\
&= \tfrac{1}{2c^2}\tfrac{\partial u^2}{\partial t} + \tfrac{1}{c^2}\nabla\varphi\cdot\left(\tfrac{\partial\nabla\varphi}{\partial t} + \tfrac{1}{2}\nabla u^2\right)\\
&= \tfrac{1}{2c^2}\left(\tfrac{\partial u^2}{\partial t} + \nabla\varphi\cdot\nabla u^2\right) + \tfrac{1}{2c^2}\tfrac{\partial}{\partial t}|\nabla\varphi|^2\\
&= \tfrac{1}{2c^2}\tfrac{du^2}{dt} + \tfrac{1}{2c^2}\tfrac{\partial u^2}{\partial t}
\end{aligned} \tag{B.9}$$

Here $\frac{d}{dt}$ in equation(B.9) is the Lagrangian derivative. Under the assumption that $c \gg u$ we can linearise the above equation to obtain

$$\Delta\varphi = \frac{1}{c^2}\frac{\partial^2\varphi}{\partial t^2}. \tag{B.10}$$

Consider a spherical bubble in a compressible liquid. Set spherical coordinates (r, ϕ, θ) with the origin at the bubble centre. Every function then depends on only one spatial variable, r, the distance from the bubble centre to the point considered, and time t. As such, the velocity $\mathbf{u}$ in the liquid satisfies

$$\mathbf{u} = u\left(r, t\right) \mathbf{e}_r, \tag{B.11}$$

where $\mathbf{e}_r$ is the unit coordinate vector for the r-coordinate. Namely, $u_r = u\left(r, t\right), u_\phi = u_\theta = 0$. One can verify the curl of the velocity field is zero. The liquid flow due to the bubble is a potential flow.

Assuming the bubble wall velocity is small compared to the speed of sound in the liquid, the flow is a weakly compressible flow. It thus satisfies the wave equation (equation B.10).

Due to spherical symmetry, equation (B.10) becomes

$$\frac{1}{r^2}\frac{\partial \varphi}{\partial r}\left(r^2 \frac{\partial \varphi}{\partial r}\right) = \frac{1}{c^2}\frac{\partial^2 \varphi}{\partial t^2}, \tag{B.12}$$

since the Laplace operator in spherical coordinates take the following form

$$\nabla^2 = \frac{1}{r^2}\frac{\partial}{\partial r}\left(r^2 \frac{\partial}{\partial r}\right) + \frac{1}{r^2 \sin^2\phi}\frac{\partial^2}{\partial \theta^2} + \frac{1}{r^2 \sin\phi}\frac{\partial}{\partial \phi}\left(\sin\phi \frac{\partial}{\partial \phi}\right). \tag{B.13}$$

The general solution of the wave equation (B.12) under spherical symmetry is obtained as follows:

$$\varphi = -\frac{f\left(t - r/c\right)}{r} - \frac{g\left(t + r/c\right)}{r}. \tag{B.14}$$

Using the Sommerfeld radiation condition, for a wave propagating away from its source, we have

$$\varphi = -\frac{f\left(t - r/c\right)}{r}. \tag{B.15}$$

The kinematic boundary condition at the bubble surface takes the form

$$\begin{aligned}\dot{R} &= \frac{\partial\varphi}{\partial r}\Big|_{r=R} = \frac{\partial\varphi(R,t)}{\partial r} = \left(\frac{\dot{f}(t-r/c)}{cr} + \frac{f(t-r/c)}{r^2}\right)_{r=R} \\ &= \frac{\dot{f}(t-R/c)}{cR} + \frac{f(t-R/c)}{R^2}.\end{aligned} \tag{B.16}$$

Using equation (B.15) we have

$$\varphi\left(R,t\right) = -\frac{f\left(t-R/c\right)}{R}, \tag{B.17}$$

and

$$\frac{\partial\varphi\left(R,t\right)}{\partial t} = -\frac{\dot{f}\left(t-R/c\right)}{R}. \tag{B.18}$$

Using these two equations, equation (B.16) can be written as

$$\frac{\partial\varphi\left(R,t\right)}{\partial t} = -c\left(\dot{R} + \frac{\varphi\left(R,t\right)}{R}\right). \tag{B.19}$$

Using Bernoulli's equation,

$$\frac{\partial\varphi}{\partial t} + \frac{1}{2}u^2 + \frac{p}{\rho} = \frac{p_{amb}}{\rho}, \tag{B.20}$$

at the bubble surface, we have

$$\frac{\partial\varphi\left(R,t\right)}{\partial t} + \frac{1}{2}\dot{R}^2 + \frac{p_B}{\rho} = \frac{p_{amb}}{\rho}. \tag{B.21}$$

This can be written as

$$\frac{\partial\varphi\left(R,t\right)}{\partial t} + \frac{1}{2}\dot{R}^2 = -\frac{p_B - p_{amb}}{\rho} = \Delta. \tag{B.22}$$

Substituting equation (B.19) into equation (B.22) yields

$$R\dot{R} + \varphi\left(R,t\right) - \frac{1}{2c}R\dot{R}^2 = -\frac{1}{c}R\Delta. \tag{B.23}$$

Noticing that

$$\begin{aligned}\frac{d\varphi(R(t),t)}{dt} &= \frac{\partial\varphi(R,t)}{\partial t} + \frac{\partial\varphi(R,t)}{\partial r}\dot{R} \\ &= \frac{\partial\varphi(R,t)}{\partial t} + \dot{R}^2 \\ &= \frac{\partial\varphi(R,t)}{\partial t} + \frac{1}{2}\dot{R}^2 + \frac{1}{2}\dot{R}^2 \\ &= \Delta + \frac{1}{2}\dot{R}^2,\end{aligned} \tag{B.24}$$

and performing $\frac{d}{dt}$ to equation (B.23), we obtain

$$\begin{aligned}
&\tfrac{d\left(R\dot{R}\right)}{dt} + \left(\Delta + \tfrac{1}{2}\dot{R}^2\right) - \tfrac{1}{2c}\tfrac{dR\dot{R}^2}{dt} = -\tfrac{1}{c}\tfrac{dR\Delta}{dt} \\
&\Rightarrow R\ddot{R} + \tfrac{3}{2}\dot{R}^2 - \tfrac{1}{2c}\left(\dot{R}^3 + 2R\dot{R}\ddot{R}\right) = -\Delta - \tfrac{1}{c}\left(\dot{R}\Delta + R\tfrac{d\Delta}{dt}\right) \\
&\Rightarrow \left(1 - \tfrac{\dot{R}}{c}\right)R\ddot{R} + \left(1 - \tfrac{\dot{R}}{3c}\right)\tfrac{3}{2}\dot{R}^2 = -\left(1 + \tfrac{\dot{R}}{c}\right)\Delta - \tfrac{R}{c}\tfrac{d\Delta}{dt}.
\end{aligned} \tag{B.25}$$

As $\Delta = -\frac{p_B - p_{amb}}{\rho}$, equation (B.25) can be rewritten as

$$\left(1 - \frac{\dot{R}}{c}\right)R\ddot{R} + \left(1 - \frac{\dot{R}}{3c}\right)\frac{3}{2}\dot{R}^2 = \left(1 + \frac{\dot{R}}{c}\right)\frac{p_B - p_{amb}}{\rho} + \frac{R}{\rho c}\frac{d}{dt}\left(p_B - p_{amb}\right). \tag{B.26}$$

where p_B can be calculated by equation (A.17). For a bubble in a quiescent liquid, the ambient pressure p_{amb} is equal to the hydrostatic pressure p_∞.

This is the Keller-Miksis equation for the time history of the radius, *R(t)*, for a bubble in a weakly compressible liquid. The Keller-Miksis equation holds for $\left|\dot{R}\right|/c \ll 1$. Note that this weakly compressible Keller–Miksis equation (B.26) reduces to the incompressible Rayleigh–Plesset equation (A.18) as $c \to \infty$.

References

[1] C. Brennen. *Cavitation and bubble dynamics*. Cambridge University Press, 2014.

[2] J. Carlton. *Marine propellers and propulsion*. Butterworth-Heinemann, 2018.

[3] X. Luo, B. Ji, and Y. Tsujimoto. "A review of cavitation in hydraulic machinery". In: *Journal of Hydrodynamics* 28.3 (2016), pp. 335–358.

[4] E. Grist. *Cavitation and the centrifugal pump: a guide for pump users*. Routledge, 2023.

[5] R. Arndt. "Cavitation in fluid machinery and hydraulic structures". In: *Annual Review of Fluid Mechanics* 13.1 (1981), pp. 273–326.

[6] T. Rus, M. Dular, B. Širok, M. Hočevar, and I. Kern. "An investigation of the relationship between acoustic emission, vibration, noise, and cavitation structures on a Kaplan turbine". In: *Journal of FluidS Engineering* 129.9 (2007), pp. 1112–1122.

[7] G. Reisman, Y. Wang, and C. Brennen. "Observations of shock waves in cloud cavitation". In: *Journal of Fluid Mechanics* 355 (1998), pp. 255–283.

[8] Y. Tomita and A. Shima. "Mechanisms of impulsive pressure generation and damage pit formation by bubble collapse". In: *Journal of Fluid Mechanics* 169 (1986), pp. 535–564.

[9] A. Philipp and W. Lauterborn. "Cavitation erosion by single laser-produced bubbles". In: *Journal of Fluid Mechanics* 361 (1998), pp. 75–116.

[10] M. Kornfeld and L. Suvorov. "On the destructive action of cavitation". In: *Journal of Applied Physics* 15.6 (1944), pp. 495–506.

[11] C. Naude and A. Ellis. "On the mechanism of cavitation damage by nonhemispherical cavities collapsing in contact with a solid boundary". In: *Journal of FluidS Engineering* 83.4 (1961), pp. 648–656.

[12] M. Plesset and R. Chapman. "Collapse of an initially spherical vapour cavity in the neighbourhood of a solid boundary". In: *Journal of Fluid Mechanics* 47.2 (1971), pp. 283–290.

[13] J. Blake and D. Gibson. "Cavitation bubbles near boundaries". In: *Annual Review of Fluid Mechanics* 19.1 (1987), pp. 99–123.

[14] W. Lauterborn and T. Kurz. "Physics of bubble oscillations". In: *Reports on Progress in Physics* 73.10 (2010), p. 106501.

[15] R. Apfel. "Acoustic cavitation: a possible consequence of biomedical uses of ultrasound." In: *The British Journal of Cancer. Supplement* 5 (1982), p. 140.

[16] T. Juhasz, X. Hu, L. Turi, and Z. Bor. "Dynamics of shock waves and cavitation bubbles generated by picosecond laser pulses in corneal tissue and water". In: *Lasers in Surgery and Medicine* 15.1 (1994), pp. 91–98.

[17] C. Coussios and R. Roy. "Applications of acoustics and cavitation to noninvasive therapy and drug delivery". In: *Annual Review of Fluid Mechanics* 40 (2008), pp. 395–420.

[18] G. Curtiss, D. Leppinen, Q. Wang, and J. Blake. "Ultrasonic cavitation near a tissue layer". In: *Journal of Fluid Mechanics* 730 (2013), pp. 245–272.

[19] K. Kooiman, H. Vos, M. Versluis, and N. De Jong. "Acoustic behavior of microbubbles and implications for drug delivery". In: *Advanced Drug Delivery Reviews* 72 (2014), pp. 28–48.

[20] A. Coleman, J. Saunders, L. Crum, and M. Dyson. "Acoustic cavitation generated by an extracorporeal shockwave lithotripter". In: *Ultrasound in Medicine & Biology* 13.2 (1987), pp. 69–76.

[21] C. Church. "A theoretical study of cavitation generated by an extracorporeal shock wave lithotripter". In: *The Journal of the Acoustical Society of America* 86.1 (1989), pp. 215–227.

[22] M. Arora, L. Junge, and C. Ohl. "Cavitation cluster dynamics in shock-wave lithotripsy: Part 1. Free field". In: *Ultrasound in Medicine & Biology* 31.6 (2005), pp. 827–839.

[23] J. Freund. "Suppression of shocked-bubble expansion due to tissue confinement with application to shock-wave lithotripsy". In: *The Journal of the Acoustical Society of America* 123.5 (2008), pp. 2867–2874.

[24] E. Brujan, K. Nahen, P. Schmidt, and A. Vogel. "Dynamics of laser-induced cavitation bubbles near elastic boundaries: influence of the elastic modulus". In: *Journal of Fluid Mechanics* 433 (2001), pp. 283–314.

[25] H. Zhou, T. Liu, R. Guo, R. Liu, and P. Song. "Numerical investigation on water blast response of freestanding carbon fiber reinforced composite sandwich plates with square honeycomb cores". In: *Applied Composite Materials* 26 (2019), pp. 605–625.

[26] E. Zilonova, M. Solovchuk, and T. Sheu. "Bubble dynamics in viscoelastic soft tissue in high-intensity focal ultrasound thermal therapy". In: *Ultrasonics Sonochemistry* 40 (2018), pp. 900–911.

[27] C. Tempany, N. McDannold, K. Hynynen, and F. Jolesz. "Focused ultrasound surgery in oncology: overview and principles". In: *Radiology* 259.1 (2011), pp. 39–56.

[28] S. Feinstein, P. Shah, R. Bing, S. Meerbaum, E. Corday, B. Chang, G. Santillan, and Y. Fujibayashi. "Microbubble dynamics visualized in the intact capillary circulation". In: *Journal of the American College of Cardiology* 4.3 (1984), pp. 595–600.

[29] J. Bull. "Cardiovascular bubble dynamics". In: *Critical Reviews™ in Biomedical Engineering* 33.4 (2005), pp. 299–346.

[30] K. Suslick. "Sonochemistry". In: *Science* 247.4949 (1990), pp. 1439–1445.

[31] V. Moholkar, P. S. Kumar, and A. Pandit. "Hydrodynamic cavitation for sonochemical effects". In: *Ultrasonics Sonochemistry* 6.1-2 (1999), pp. 53–65.

[32] T. Mason and J. Lorimer. *Applied Sonochemistry: the uses of power ultrasound in chemistry and processing*. Wiley-Vch Weinheim, 2002.

[33] K. Suslick, N. Eddingsaas, D. Flannigan, S. Hopkins, and H. Xu. "The chemical history of a bubble". In: *Accounts of Chemical Research* 51.9 (2018), pp. 2169–2178.

[34] C. Ohl, M. Arora, R. Dijkink, V. Janve, and D. Lohse. "Surface cleaning from laser-induced cavitation bubbles". In: *Applied Physics Letters* 89.7 (2006), p. 074102.

[35] G. Chahine, A. Kapahi, J. Choi, and C. Hsiao. "Modeling of surface cleaning by cavitation bubble dynamics and collapse". In: *Ultrasonics Sonochemistry* 29 (2016), pp. 528–549.

[36] F. Reuter, S. Lauterborn, R. Mettin, and W. Lauterborn. "Membrane cleaning with ultrasonically driven bubbles". In: *Ultrasonics Sonochemistry* 37 (2017), pp. 542–560.

[37] N. Vyas, E. Pecheva, H. Dehghani, R. Sammons, Q. Wang, D. Leppinen, and A. Walmsley. "High speed imaging of cavitation around dental ultrasonic scaler tips". In: *PLoS One* 11.3 (2016), e0149804.

[38] N. Vyas, H. Dehghani, R. Sammons, Q. Wang, D. Leppinen, and A. Walmsley. "Imaging and analysis of individual cavitation microbubbles around dental ultrasonic scalers". In: *Ultrasonics* 81 (2017), pp. 66–72.

[39] N. Vyas, K. Manmi, Q. Wang, A. Jadhav, M. Barigou, R. Sammons, S. Kuehne, and A. Walmsley. "Which parameters affect biofilm removal with acoustic cavitation? A review". In: *Ultrasound in Medicine & Biology* 45.5 (2019), pp. 1044–1055.

[40] K. Manmi, W. Wu, N. Vyas, W. Smith, Q. Wang, and A. Walmsley. "Numerical investigation of cavitation generated by an ultrasonic dental scaler tip vibrating in a compressible liquid". In: *Ultrasonics Sonochemistry* 63 (2020), p. 104963.

[41] Y. Yu, M. Mahmud, N. Vyas, W. Smith, Q. Wang, and A. Walmsley. "Cavitation in a periodontal pocket by an ultrasonic dental scaler: A numerical investigation". In: *Ultrasonics Sonochemistry* 90 (2022), p. 106178.

[42] Q. Wang and K. Manmi. "Three dimensional microbubble dynamics near a wall subject to high intensity ultrasound". In: *Physics of Fluids* 26.3 (2014), p. 032104.

[43] L. Rayleigh. "VIII. On the pressure developed in a liquid during the collapse of a spherical cavity". In: *The London, Edinburgh, and Dublin Philosophical Magazine and Journal of Science* 34.200 (1917), pp. 94–98.

[44] M. Plesset. "The dynamics of cavitation bubbles". In: *Journal of Applied Mechanics* 16.3 (1949), pp. 277–282.

[45] C. Herring. *Theory of the pulsations of the gas bubble produced by an underwater explosion*. Columbia University, Division of National Defense Research, 1941.

[46] L. Trilling. "The collapse and rebound of a gas bubble". In: *Journal of Applied Physics* 23.1 (1952), pp. 14–17.

[47] J. Keller and I. Kolodner. "Damping of underwater explosion bubble oscillations". In: *Journal of Applied Physics* 27.10 (1956), pp. 1152–1161.

[48] R. Hickling and M. Plesset. "Collapse and rebound of a spherical bubble in water". In: *The Physics of Fluids* 7.1 (1964), pp. 7–14.

[49] H. Flynn. "Cavitation dynamics. I. A mathematical formulation". In: *The Journal of the Acoustical Society of America* 57.6 (1975), pp. 1379–1396.

[50] J. Keller and M. Miksis. "Bubble oscillations of large amplitude". In: *The Journal of the Acoustical Society of America* 68.2 (1980), pp. 628–633.

[51] S. Fujikawa and T. Akamatsu. “Effects of the non-equilibrium condensation of vapour on the pressure wave produced by the collapse of a bubble in a liquid”. In: *Journal of Fluid Mechanics* 97.3 (1980), pp. 481–512.

[52] A. Prosperetti and A. Lezzi. “Bubble dynamics in a compressible liquid. Part 1. First-order theory”. In: *Journal of Fluid Mechanics* 168 (1986), pp. 457–478.

[53] A. Lezzi and A. Prosperetti. “Bubble dynamics in a compressible liquid. Part 2. Second-order theory”. In: *Journal of Fluid Mechanics* 185 (1987), pp. 289–321.

[54] A. Zhang, S. Li, P. Cui, S. Li, and Y. Liu. “A unified theory for bubble dynamics”. In: *Physics of Fluids* 35.3 (2023), p. 033323.

[55] W. Lauterborn and H. Bolle. “Experimental investigations of cavitation-bubble collapse in the neighbourhood of a solid boundary”. In: *Journal of Fluid Mechanics* 72.2 (1975), pp. 391–399.

[56] A. Vogel, W. Lauterborn, and R. Timm. “Optical and acoustic investigations of the dynamics of laser-produced cavitation bubbles near a solid boundary”. In: *Journal of Fluid Mechanics* 206 (1989), pp. 299–338.

[57] I. Akhatov, O. Lindau, A. Topolnikov, R. Mettin, N. Vakhitova, and W. Lauterborn. “Collapse and rebound of a laser-induced cavitation bubble”. In: *Physics of Fluids* 13.10 (2001), pp. 2805–2819.

[58] E. Brujan, G. Keen, A. Vogel, and J. Blake. “The final stage of the collapse of a cavitation bubble close to a rigid boundary”. In: *Physics of Fluids* 14.1 (2002), pp. 85–92.

[59] A. Zhang, P. Cui, J. Cui, and Q. Wang. “Experimental study on bubble dynamics subject to buoyancy”. In: *Journal of Fluid Mechanics* 776 (2015), pp. 137–160.

[60] X. Ma, B. Huang, X. Zhao, Y. Wang, Q. Chang, S. Qiu, X. Fu, and G. Wang. "Comparisons of spark-charge bubble dynamics near the elastic and rigid boundaries". In: *Ultrasonics Sonochemistry* 43 (2018), pp. 80–90.

[61] H. Sagar and O. El Moctar. "Dynamics of a cavitation bubble between oblique plates". In: *Physics of Fluids* 35.1 (2023), p. 013324.

[62] J. Blake, B. Taib, and G. Doherty. "Transient cavities near boundaries. Part 1. Rigid boundary". In: *Journal of Fluid Mechanics* 170 (1986), pp. 479–497.

[63] M. Koch, C. Lechner, F. Reuter, K. Köhler, R. Mettin, and W. Lauterborn. "Numerical modeling of laser generated cavitation bubbles with the finite volume and volume of fluid method, using OpenFOAM". In: *Computers & Fluids* 126 (2016), pp. 71–90.

[64] J. Blake and D. Gibson. "Growth and collapse of a vapour cavity near a free surface". In: *Journal of Fluid Mechanics* 111 (1981), pp. 123–140.

[65] E. Johnsen and T. Colonius. "Numerical simulations of non-spherical bubble collapse". In: *Journal of Fluid Mechanics* 629 (2009), pp. 231–262.

[66] S. Popinet and S. Zaleski. "Bubble collapse near a solid boundary: a numerical study of the influence of viscosity". In: *Journal of Fluid Mechanics* 464 (2002), pp. 137–163.

[67] C. Lechner, W. Lauterborn, M. Koch, and R. Mettin. "Jet formation from bubbles near a solid boundary in a compressible liquid: Numerical study of distance dependence". In: *Physical Review Fluids* 5.9 (2020), p. 093604.

[68] W. White, S. Beig, and E. Johnsen. "Pressure fields produced by single-bubble collapse near a corner". In: *Physical Review Fluids* 8.2 (2023), p. 023601.

[69] F. Reuter, S. Lesnik, K. Ayaz-Bustami, G. Brenner, and R. Mettin. "Bubble size measurements in different acoustic cavitation structures: Filaments, clusters, and the acoustically cavitated jet". In: *Ultrasonics Sonochemistry* 55 (2019), pp. 383–394.

[70] E. Brujan and A. Vogel. "Stress wave emission and cavitation bubble dynamics by nanosecond optical breakdown in a tissue phantom". In: *Journal of Fluid Mechanics* 558 (2006), pp. 281–308.

[71] O. Lindau and W. Lauterborn. "Cinematographic observation of the collapse and rebound of a laser-produced cavitation bubble near a wall". In: *Journal of Fluid Mechanics* 479 (2003), pp. 327–348.

[72] E. Brujan and Y. Matsumoto. "Collapse of micrometer-sized cavitation bubbles near a rigid boundary". In: *Microfluidics and Nanofluidics* 13 (2012), pp. 957–966.

[73] O. Supponen, D. Obreschkow, M. Tinguely, P. Kobel, N. Dorsaz, and M. Farhat. "Scaling laws for jets of single cavitation bubbles". In: *Journal of Fluid Mechanics* 802 (2016), pp. 263–293.

[74] O. Supponen, D. Obreschkow, P. Kobel, M. Tinguely, N. Dorsaz, and M. Farhat. "Shock waves from nonspherical cavitation bubbles". In: *Physical Review Fluids* 2.9 (2017), p. 093601.

[75] E. Brujan, T. Noda, A. Ishigami, T. Ogasawara, and H. Takahira. "Dynamics of laser-induced cavitation bubbles near two perpendicular rigid walls". In: *Journal of Fluid Mechanics* 841 (2018), pp. 28–49.

[76] P. Cui, A. Zhang, S. Wang, and Y. Liu. "Experimental study on interaction, shock wave emission and ice breaking of two collapsing bubbles". In: *Journal of Fluid Mechanics* 897 (2020), A25.

[77] O. Voinov. "A calculation of the parameters of the high-speed jet formed in the collapse of a bubble". In: *Journal of Applied Mechanics and Technical Physics* 20.3 (1979), pp. 333–337.

[78] Q. Wang, K. Yeo, B. Khoo, and K. Lam. "Strong interaction between a buoyancy bubble and a free surface". In: *Theoretical and Computational Fluid Dynamics* 8 (1996), pp. 73–88.

[79] Q. Wang. "The evolution of a gas bubble near an inclined wall". In: *Theoretical and Computational Fluid Dynamics* 12 (1998), pp. 29–51.

[80] Q. Wang, K. Yeo, B. Khoo, and K. Lam. "Vortex ring modelling of toroidal bubbles". In: *Theoretical and Computational Fluid Dynamics* 19 (2005), pp. 303–317.

[81] Q. Wang. "Multi-oscillations of a bubble in a compressible liquid near a rigid boundary". In: *Journal of Fluid Mechanics* 745 (2014), pp. 509–536.

[82] V. Minsier, J. De Wilde, and J. Proost. "Simulation of the effect of viscosity on jet penetration into a single cavitating bubble". In: *Journal of Applied Physics* 106.8 (2009), p. 084906.

[83] A. Tiwari, J. Freund, and C. Pantano. "A diffuse interface model with immiscibility preservation". In: *Journal of Computational Physics* 252 (2013), pp. 290–309.

[84] L. Ge, A. Zhang, and S. Wang. "Investigation of underwater explosion near composite structures using a combined RKDG-FEM approach". In: *Journal of Computational Physics* 404 (2020), p. 109113.

[85] C. Lechner, M. Koch, W. Lauterborn, and R. Mettin. "Pressure and tension waves from bubble collapse near a solid boundary: A numerical approach". In: *The Journal of the Acoustical Society of America* 142.6 (2017), pp. 3649–3659.

[86] Y. Liu, A. Zhang, Z. Tian, and S. Wang. "Investigation of free-field underwater explosion with Eulerian finite element method". In: *Ocean Engineering* 166 (2018), pp. 182–190.

[87] N. Liu, A. Zhang, Y. Liu, and T. Li. "Numerical analysis of the interaction of two underwater explosion bubbles using the compressible Eulerian finite-element method". In: *Physics of Fluids* 32.4 (2020), p. 046107.

[88] Q. Zeng, S. Gonzalez-Avila, R. Dijkink, P. Koukouvinis, M. Gavaises, and C. Ohl. "Wall shear stress from jetting cavitation bubbles". In: *Journal of Fluid Mechanics* 846 (2018), pp. 341–355.

[89] Q. Zeng, S. Gonzalez-Avila, and C. Ohl. "Splitting and jetting of cavitation bubbles in thin gaps". In: *Journal of Fluid Mechanics* 896 (2020), A28.

[90] Q. Zeng, H. An, and C. Ohl. "Wall shear stress from jetting cavitation bubbles: Influence of the stand-off distance and liquid viscosity". In: *Journal of Fluid Mechanics* 932 (2022), A14.

[91] H. Xu, N. Eddingsaas, and K. Suslick. "Spatial separation of cavitating bubble populations: the nanodroplet injection model". In: *Journal of the American Chemical Society* 131.17 (2009), pp. 6060–6061.

[92] T. Leighton. *The acoustic bubble*. Academic Press, 2012.

[93] Y. Matsumoto. "Bubble and bubble cloud dynamics". In: *AIP Conference Proceedings*. Vol. 524. 1. American Institute of Physics. 2000, pp. 65–74.

[94] A. Konno, H. Kato, H. Yamaguchi, and M. Maeda. "On the collapsing behavior of cavitation bubble clusters". In: *JSME International Journal Series B Fluids and Thermal Engineering* 45.3 (2002), pp. 631–637.

[95] D. Krefting, R. Mettin, and W. Lauterborn. "High-speed observation of acoustic cavitation erosion in multibubble systems". In: *Ultrasonics Sonochemistry* 11.3-4 (2004), pp. 119–123.

[96] Y. Matsumoto and S. Yoshizawa. "Behaviour of a bubble cluster in an ultrasound field". In: *International Journal for Numerical Methods in Fluids* 47.6-7 (2005), pp. 591–601.

[97] E. Brujan, T. Ikeda, K. Yoshinaka, and Y. Matsumoto. "The final stage of the collapse of a cloud of bubbles close to a rigid boundary". In: *Ultrasonics Sonochemistry* 18.1 (2011), pp. 59–64.

[98] A. Tiwari, C. Pantano, and J. Freund. "Growth-and-collapse dynamics of small bubble clusters near a wall". In: *Journal of Fluid Mechanics* 775 (2015), pp. 1–23.

[99] Y. Wang and C. Brennen. "Numerical computation of shock waves in a spherical cloud of cavitation bubbles". In: *Journal of FluidS Engineering* 121.4 (1999), pp. 872–880.

[100] J. Ma, C. Hsiao, and G. Chahine. "Euler–Lagrange simulations of bubble cloud dynamics near a wall". In: *Journal of Fluids Engineering* 137.4 (2015), p. 041301.

[101] J. Ma, C. Hsiao, and G. Chahine. "Numerical study of acoustically driven bubble cloud dynamics near a rigid wall". In: *Ultrasonics Sonochemistry* 40 (2018), pp. 944–954.

[102] G. L. Chahine and R. Duraiswami. "Dynamical interactions in a multi-bubble cloud". In: *Journal of FluidS Engineering* 114.4 (1992), pp. 680–686.

[103] N. Adams and S. Schmidt. "Shocks in cavitating flows". In: *Bubble dynamics and shock waves*. Springer, 2013, pp. 235–256.

[104] D. Ogloblina, S. Schmidt, and N. Adams. "Numerical simulation of collapsing vapor bubble clusters close to a rigid wall". In: *International Symposium on Cavitation [CAV, 10th, 2018]*. 2018, 6–S.

[105] D. Rossinelli, B. Hejazialhosseini, P. Hadjidoukas, C. Bekas, A. Curioni, A. Bertsch, S. Futral, S. Schmidt, N. Adams, and P. Koumoutsakos. "11 PFLOP/s simulations

of cloud cavitation collapse". In: *Proceedings of the International Conference on High Performance Computing, Networking, Storage and Analysis*. 2013, pp. 1–13.

[106] F. Wermelinger, U. Rasthofer, P. Hadjidoukas, and P. Koumoutsakos. "Petascale simulations of compressible flows with interfaces". In: *Journal of Computational Science* 26 (2018), pp. 217–225.

[107] U. Rasthofer, F. Wermelinger, P. Hadijdoukas, and P. Koumoutsakos. "Large scale simulation of cloud cavitation collapse". In: *Procedia Computer Science* 108 (2017), pp. 1763–1772.

[108] U. Rasthofer, F. Wermelinger, P. Karnakov, J. Šukys, and P. Koumoutsakos. "Computational study of the collapse of a cloud with 12 500 gas bubbles in a liquid". In: *Physical Review Fluids* 4.6 (2019), p. 063602.

[109] C. Egerer, S. Hickel, S. Schmidt, and N. Adams. "Large-eddy simulation of turbulent cavitating flow in a micro channel". In: *Physics of Fluids* 26.8 (2014), p. 085102.

[110] G. Schnerr, I. Sezal, and S. Schmidt. "Numerical investigation of three-dimensional cloud cavitation with special emphasis on collapse induced shock dynamics". In: *Physics of Fluids* 20.4 (2008), p. 040703.

[111] B. Budich, S. Schmidt, and N. Adams. "Numerical simulation and analysis of condensation shocks in cavitating flow". In: *Journal of Fluid Mechanics* 838 (2018), pp. 759–813.

[112] T. Theofanous, L. Biasi, H. Isbin, and H. Fauske. "A theoretical study on bubble growth in constant and time-dependent pressure fields". In: *Chemical Engineering Science* 24.5 (1969), pp. 885–897.

[113] Y. Matsumoto, T. Kanbara, and K. Sugiyama. "Numerical study of cavitating flow structure on a hydrofoil". In: *KSME/JSME THERMAL and FLUID Engineering Conference*. 1998, pp. 249–252.

[114] P. Zwart, A. Gerber, T. Belamri, et al. "A two-phase flow model for predicting cavitation dynamics". In: *Fifth International Conference on Multiphase Flow*. Vol. 152. 2004.

[115] D. Fuster, G. Agbaglah, C. Josserand, S. Popinet, and S. Zaleski. "Numerical simulation of droplets, bubbles and waves: state of the art". In: *Fluid Dynamics Research* 41.6 (2009), p. 065001.

[116] G. Schnerr and J. Sauer. "Physical and numerical modeling of unsteady cavitation dynamics". In: *Fourth International Conference on Multiphase Flow*. Vol. 1. ICMF New Orleans New Orleans, LO, USA. 2001.

[117] G. Cazzoli, S. Falfari, G. Bianchi, C. Forte, and C. Catellani. "Assessment of the cavitation models implemented in OpenFOAM® Under DI-like conditions". In: *Energy Procedia* 101 (2016), pp. 638–645.

[118] L. Hanimann, L. Mangani, E. Casartelli, and M. Widmer. "Cavitation modeling for steady-state CFD simulations". In: *IOP Conference Series: Earth and Environmental Science*. Vol. 49. 9. IOP Publishing. 2016, p. 092005.

[119] E. Stavropoulos-Vasilakis, N. Kyriazis, H. Jadidbonab, P. Koukouvinis, and M. Gavaises. "Review of numerical methodologies for modeling cavitation". In: *Cavitation and Bubble Dynamics* (2021), pp. 1–35.

[120] A. Walmsley, S. Lea, G. Landini, and A. Moses. "Advances in power driven pocket/root instrumentation". In: *Journal of Clinical Periodontology* 35 (2008), pp. 22–28.

[121] D. Herrera, T. Berglundh, F. Schwarz, I. Chapple, S. Jepsen, A. Sculean, M. Kebschull, P. Papapanou, M. Tonetti, M. Sanz, et al. "Prevention and treatment of peri-implant diseases—The EFP S3 level clinical practice guideline". In: *Journal of Clinical Periodontology* 26 (2023), pp. 4–76.

[122] B. Felver, D. King, S. Lea, G. Price, and A. Walmsley. "Cavitation occurrence around ultrasonic dental scalers". In: *Ultrasonics Sonochemistry* 16.5 (2009), pp. 692–697.

[123] G. Price, T. Tiong, and D. King. "Sonochemical characterisation of ultrasonic dental descalers". In: *Ultrasonics Sonochemistry* 21.6 (2014), pp. 2052–2060.

[124] A. Walmsley, S. Lea, B. Felver, D. King, and G. Price. "Mapping cavitation activity around dental ultrasonic tips". In: *Clinical Oral Investigations* 17 (2013), pp. 1227–1234.

[125] S. J. Gartenmann, T. Thurnheer, T. Attin, and P. R. Schmidlin. "Influence of ultrasonic tip distance and orientation on biofilm removal". In: *Clinical Oral Investigations* 21 (2017), pp. 1029–1036.

[126] N. Vyas, M. Grewal, S. Kuehne, R. Sammons, and A. Walmsley. "High speed imaging of biofilm removal from a dental implant model using ultrasonic cavitation". In: *Dental Materials* 36.6 (2020), pp. 733–743.

[127] B. Verhaagen and D. Rivas. "Measuring cavitation and its cleaning effect". In: *Ultrasonics Sonochemistry* 29 (2016), pp. 619–628.

[128] W. Song, M. Hong, B. Lukyanchuk, and T. Chong. "Laser-induced cavitation bubbles for cleaning of solid surfaces". In: *Journal of Applied Physics* 95.6 (2004), pp. 2952–2956.

[129] M. O. Lamminen, H. W. Walker, and L. K. Weavers. "Mechanisms and factors influencing the ultrasonic cleaning of particle-fouled ceramic membranes". In: *Journal of Membrane Science* 237.1-2 (2004), pp. 213–223.

[130] B. Klenow and A. Brown. "Prevention of pressure oscillations in modeling a cavitating acoustic fluid". In: *Shock and Vibration* 17.2 (2010), pp. 137–159.

[131] H. Weller, G. Tabor, H. Jasak, and C. Fureby. "A tensorial approach to computational continuum mechanics using object-oriented techniques". In: *Computers in Physics* 12.6 (1998), pp. 620–631.

[132] Q. Wang and J. Blake. "Non-spherical bubble dynamics in a compressible liquid. Part 1. Travelling acoustic wave". In: *Journal of Fluid Mechanics* 659 (2010), pp. 191–224.

[133] Q. Wang and J. Blake. "Non-spherical bubble dynamics in a compressible liquid. Part 2. Acoustic standing wave". In: *Journal of Fluid Mechanics* 679 (2011), pp. 559–581.

[134] R. Ogden. "Large deformation isotropic elasticity–on the correlation of theory and experiment for incompressible rubberlike solids". In: *Proceedings of the Royal Society of London. A. Mathematical and Physical Sciences* 326.1567 (1972), pp. 565–584.

[135] R. Ogden. *Non-linear elastic deformations*. Courier Corporation, 1997.

[136] H. Jasak. "Error analysis and estimation for the finite volume method with applications to fluid flows." PhD thesis. Imperial College London (University of London), 1996.

[137] H. Rusche. "Computational fluid dynamics of dispersed two-phase flows at high phase fractions". PhD thesis. Imperial College London (University of London), 2003.

[138] C. Hirt and B. Nichols. "Volume of fluid (VOF) method for the dynamics of free boundaries". In: *Journal of Computational Physics* 39.1 (1981), pp. 201–225.

[139] K. Wardle, H. Weller, et al. "Hybrid multiphase CFD solver for coupled dispersed/segregated flows in liquid-liquid extraction". In: *International Journal of Chemical Engineering* 2013 (2013).

[140] J. Brackbill, D. Kothe, and C. Zemach. "A continuum method for modeling surface tension". In: *Journal of Computational Physics* 100.2 (1992), pp. 335–354.

[141] Y. Li. "Equation of state of water and sea water". In: *Journal of Geophysical Research* 72.10 (1967), pp. 2665–2678.

[142] T. Leighton, S. Meers, and P. White. "Propagation through nonlinear time-dependent bubble clouds and the estimation of bubble populations from measured acoustic characteristics". In: *Proceedings of the Royal Society of London. Series A: Mathematical, Physical and Engineering Sciences* 460.2049 (2004), pp. 2521–2550.

[143] D. Gerlach, G. Tomar, G. Biswas, and F. Durst. "Comparison of volume-of-fluid methods for surface tension-dominant two-phase flows". In: *International Journal of Heat and Mass Transfer* 49.3-4 (2006), pp. 740–754.

[144] Z. Zhang and H. Zhang. "Surface tension effects on the behavior of two cavities near a rigid wall". In: *Physical Review E* 71.6 (2005), p. 066302.

[145] J. He, X. Zhou, N. Zhang, M. Nie, W. Mao, and Z. Lu. "Study of surface tension effects on near-wall cavitation bubble collapse with a pseudopotential lattice Boltzmann model". In: *AIP Advances* 12.3 (2022).

[146] S. Miller, H. Jasak, D. Boger, E. Paterson, and A. Nedungadi. "A pressure-based, compressible, two-phase flow finite volume method for underwater explosions". In: *Computers & Fluids* 87 (2013), pp. 132–143.

[147] M. Koch, J. Rosselló, C. Lechner, W. Lauterborn, and R. Mettin. "Dynamics of a laser-induced bubble above the flat top of a solid cylinder—Mushroom-shaped bubbles and the fast jet". In: *Fluids* 7.1 (2021), p. 2.

[148] Y. Yu, J. Cui, W. Smith, Q. Wang, and T. Leighton. "The mechanisms of jetting, vortex sheet, and vortex ring development in asymmetric bubble dynamics". In: *Physics of Fluids* 35.12 (2023), p. 123320.

[149] A. U. Manual. "Abaqus theory guide". In: *Version* 6.14 (2014), p. 281.

[150] T. Łodygowski and W. Sumelka. "Limitations in application of finite element method in acoustic numerical simulation". In: *Journal of Theoretical and Applied Mechanics* 44.4 (2006), pp. 849–865.

[151] M. Abdullahi and S. Oyadiji. "Acoustic wave propagation in air-filled pipes using finite element analysis". In: *Applied Sciences* 8.8 (2018), p. 1318.

[152] A. B. Wardlaw Jr and J. Luton. "Fluid-structure interaction mechanisms for close-in explosions". In: *Shock and Vibration* 7.5 (2000), pp. 265–275.

[153] J. Park. "A Runge Kutta discontinuous Galerkin-direct ghost fluid (RKDG-DGF) method to near-field early-time underwater explosion (UNDEX) simulations". PhD thesis. Virginia Tech, 2008.

[154] W. Wu, A. Zhang, Y. Liu, and S. Wang. "Local discontinuous Galerkin method for far-field underwater explosion shock wave and cavitation". In: *Applied Ocean Research* 87 (2019), pp. 102–110.

[155] T. Liu, B. Khoo, and W. Xie. "Isentropic one-fluid modelling of unsteady cavitating flow". In: *Journal of Computational Physics* 201.1 (2004), pp. 80–108.

[156] W. Xie, Y. Young, T. Liu, and B. Khoo. "Dynamic response of deformable structures subjected to shock load and cavitation reload". In: *Computational Mechanics* 40 (2007), pp. 667–681.

[157] J. Cui, T. Zhou, X. Huang, and Z. Li. "Experimental study of bubble dynamics in the neighbourhood of a vertical incomplete boundary". In: *Ultrasonics Sonochemistry* 75 (2021), p. 105587.

[158] R. Klein and L. Ting. "Far field velocity potential induced by a rapidly decaying vorticity distribution". In: *Zeitschrift für angewandte Mathematik und Physik ZAMP* 41.3 (1990), pp. 395–418.

[159] C. Felippa. "A family of early-time approximations for fluid-structure interaction". In: *Journal of Applied Mechanics* 47.4 (1980), pp. 703–708.

[160] R. Courant, K. Friedrichs, and H. Lewy. "On the partial difference equations of mathematical physics". In: *IBM Journal of Research and Development* 11.2 (1967), pp. 215–234.

[161] D. Akhmetov. "Loss of energy during the motion of a vortex ring." In: *Journal of Applied Mechanics & Technical Physics* 49.1 (2008), p. 18.

[162] T. Pedley. "The toroidal bubble". In: *Journal of Fluid Mechanics* 32.1 (1968), pp. 97–112.

[163] T. Lundgren and N. Mansour. "Vortex ring bubbles". In: *Journal of Fluid Mechanics* 224 (1991), pp. 177–196.

[164] S. Zhang, J. Duncan, and G. Chahine. "The final stage of the collapse of a cavitation bubble near a rigid wall". In: *Journal of Fluid Mechanics* 257 (1993), pp. 147–181.

[165] A. Zhang and Y. Liu. "Improved three-dimensional bubble dynamics model based on boundary element method". In: *Journal of Computational Physics* 294 (2015), pp. 208–223.

[166] K. Chun, K. Kum, W. Lee, S. Baek, H. Choi, and W. Shon. "Evaluation of the safety and efficiency of novel metallic implant scaler tips manufactured by the powder injection molding technique". In: *BMC Oral Health* 17.1 (2017), pp. 1–8.

[167] M. M. Fyrillas and A. J. Szeri. "Dissolution or growth of soluble spherical oscillating bubbles". In: *Journal of Fluid Mechanics* 277 (1994), pp. 381–407.

[168] W. Smith and Q. Wang. "A theoretical model for the growth of spherical bubbles by rectified diffusion". In: *Journal of Fluid Mechanics* 939 (2022), A28.

[169] W. Dukić, I. Bago, A. Aurer, and M. Roguljić. "Clinical effectiveness of diode laser therapy as an adjunct to non-surgical periodontal treatment: a randomized clinical study". In: *Journal of Periodontology* 84.8 (2013), pp. 1111–1117.

[170] L. E. Kinsler, A. R. Frey, A. B. Coppens, and J. V. Sanders. *Fundamentals of acoustics*. John wiley & sons, 2000.

[171] M. Jezeršek, K. Molan, S. Terlep, Š. Levičnik-Höfferle, B. Gašpirc, M. Lukač, and D. Stopar. "The evolution of cavitation in narrow soft-solid wedge geometry mimicking periodontal and peri-implant pockets". In: *Ultrasonics Sonochemistry* 94 (2023), p. 106329.

[172] T. Kim, J. Kim, and O. Jeong. "Measurement of nonlinear mechanical properties of PDMS elastomer". In: *Microelectronic Engineering* 88.8 (2011), pp. 1982–1985.

[173] F. Beer, E. Johnston, E. Eisenberg, D. Mazurek, W. Clausen, and P. Cornwell. *Vector mechanics for engineers*. McGraw-Hill New York, 1977.

[174] J. Gere and B. Goodno. *Mechanics of materials*. Cengage Learning, 2012.

[175] E. Brujan, A. Zhang, Y. Liu, T. Ogasawara, and H. Takahira. "Jetting and migration of a laser-induced cavitation bubble in a rectangular channel". In: *Journal of Fluid Mechanics* 948 (2022), A6.

[176] S. Gonzalez-Avila, A. Van Blokland, Q. Zeng, and C. Ohl. "Jetting and shear stress enhancement from cavitation bubbles collapsing in a narrow gap". In: *Journal of Fluid Mechanics* 884 (2020), A23.

[177] T. Li, S. Wang, S. Li, and A. Zhang. "Numerical investigation of an underwater explosion bubble based on FVM and VOF". In: *Applied Ocean Research* 74 (2018), pp. 49–58.

[178] T. Li, A. Zhang, S. Wang, S. Li, and W. Liu. "Bubble interactions and bursting behaviors near a free surface". In: *Physics of Fluids* 31.4 (2019), p. 042104.

[179] J. Rosselló, H. Reese, and C. Ohl. "Dynamics of pulsed laser-induced cavities on a liquid–gas interface: From a conical splash to a 'bullet'jet". In: *Journal of Fluid Mechanics* 939 (2022), A35.

[180] H. Reese, R. Schädel, F. Reuter, and C. Ohl. “Microscopic pumping of viscous liquids with single cavitation bubbles”. In: *Journal of Fluid Mechanics* 944 (2022), A17.

[181] F. Young. *Cavitation*. World Scientific, 1999.